PENETRATION OF COMPOSITE LAMINATES

BY CONICAL INDENTERS AND PROJECTILES

by

Timothy A. Sanders

B.Sc. Electro-Mechanical Engineering, The University of Cape Town, 1994

A THESIS SUBMITTED IN PARTIAL FULFILMENT OF

THE REQUIREMENTS FOR THE DEGREE OF

MASTER OF APPLIED SCIENCE

in

THE FACULTY OF GRADUATE STUDIES

(Department of Civil Engineering)

We accept this thesis as conforming
to the required standard

THE UNIVERSITY OF BRITISH COLUMBIA

July, 1997

In presenting this thesis in partial fulfilment of the requirements for an advanced degree at the University of British Columbia, I agree that the Library shall make it freely available for reference and study. I further agree that permission for extensive copying of this thesis for scholarly purposes may be granted by the head of my department or by his or her representatives. It is understood that copying or publication of this thesis for financial gain shall not be allowed without my written permission.

Department of CIVIL ENGINEERING

The University of British Columbia
Vancouver, Canada

Date JULY 28, 1997

DE-6 (2/88)

Abstract

Impact resistance of composite materials is a primary concern where human lives are at risk. To design against impact the mechanisms by which these composites defeat projectiles becomes important to understand. The main focus of this thesis has been understanding the initiation and progression of damage in both carbon fibre reinforced polymer (CFRP) and glass fibre reinforced polymer (GFRP) composites. Static penetration tests were performed on CFRP laminates while both instrumented ballistic and static penetration tests were performed on GFRP laminates. The projectiles used for this study were cylindro-conical and the damage mechanisms were identified through detailed micro-graphs.

Detailed ballistic force-displacement curves were obtained for GFRP laminates using a measurement system developed during the course of this thesis. Using these ballistic force-displacement curves it was then possible to compare the static and ballistic response of the GFRP laminates. Good agreement was found and as far as the author is aware, it is also the first time that such a detailed comparison has been made. The combination of damage progression and force-displacement curves provides the necessary input data for the analytical and numerical models currently under development at UBC.

Table of Contents

List of Tables

List of Figures

Acknowledgments

I would first like to thank my supervisor, Reza Vaziri, for his guidance and support during this thesis.

I would also like to thank Anoush Poursartip for the many valuable lessons he taught me about experimental work. His constant attention to detail and probing questions have left a lasting impression on how to approach and solve problems.

I would also like to thank the people who made this thesis possible. The time and effort Roger Bennett, Ross McLeod and Carl Ng put into 'building' my thesis is enormously appreciated, and this thesis would not have been possible without their help.

A big thank-you to Darlene Starratt who shared in the struggles and frustrations involved in developing the LLVS. Many calibrations later and the laser system finally works.

Also many thanks to all the members, past and present, of the Composites Group whose encouragement was felt and whose friendship will be sorely missed.

I would like to gratefully acknowledge the Natural Sciences and Engineering Research Council of Canada for their financial support and the Canadian Department of National Defence and Defence Research Establishment Valcartier (DREV) for providing technical support.

Finally, a loving thank-you to Giga Swan who provided me with the support I needed to finish this thesis when I did.

Chapter One

Introduction

1.1 Background

Composite materials are being used increasingly for applications such as defence and aerospace. Their high stiffness-to-weight and strength-to-weight ratios make them attractive for use in military and commercial aeroplanes, military land vehicles and protective body armour. Composites are being used in places where human lives are at risk. As a result it is becoming increasingly important that the mechanisms by which composites defeat projectiles are fully understood. Fully understanding these mechanisms in turn allows for effective design against impact.

Impact can be caused by something as simple as a tool being dropped, to shrapnel from a land mine, to the worst case of a direct hit by a ballistic projectile. The major problem with composite materials is that for low energy impact the damage can sometimes be undetectable. Even for high energy impact there can be considerable internal damage which is not visible.

Composites, unlike metals, have quite complicated damage mechanisms. The main damage mechanisms in composites are matrix failure, fibre failure and delamination. To design against impact it is important to understand the progression of damage in composites. In this way the

different damage mechanisms can be identified and more importantly the amount of energy needed to initiate each mechanism can be obtained.

Most authors use low velocity and static tests to identify the initiation and progression of damage and then apply this to a model to predict the ballistic response.

Cantwell and Morton [1989] performed a study that compared the low and high velocity impact of CFRP. They found that similarities do exist when comparing the damage from the two velocity regimes. Initial failure was found to occur at the same place and the shear zones observed at the perforation energies were found to be very similar. They did find, however, that the threshold energies for damage initiation and target perforation differed quite considerably. The reason for this is shown schematically in Figure 1.1. For low velocity impact the projectile induces a global response of the specimen. Thus the specimen appears very flexible and the impact energy is dissipated over a large area. For high velocity impact, however, the projectile causes a more localised response of the specimen and the energy is dissipated over a very small zone.

Pierson [1994] used the concept of local and global effects in modelling the response of CFRP specimens to impact by hemispherical, blunt and conical shaped projectiles. The local and global effects were treated separately and the complete penetration process was modelled as a superposition of the local and global response.

Lee and Sun [1993a] developed a model to predict the penetration of thin CFRP laminates by blunt projectiles. A series of static tests were carried out in order to characterise the load-displacement curve or response during penetration. In the study, ballistic tests were also

performed and the preliminary results showed that the dynamic failure modes were similar to the static case. Sun and Potti [1993] compared the static and ballistic tests for CFRP laminates on a range of thicknesses and once again found that the overall damage pattern in the static test was similar to the ballistic test.

Therefore depending on the material it is often possible to us static tests to predict the ballistic response. This is a very useful tool to have when it comes to looking at the progression of damage. A static test has the advantage over a ballistic test in that the event happens very slowly. The transition between damage mechanisms can be clearly defined allowing a detailed analysis of the penetration. Thus the progression of damage is useful in terms of characterising how much of each damage mechanism contributes to the energy absorption during the impact.

Most authors identified the damage mechanisms in composites as matrix cracking, delamination and fibre fracture. The order that these occur depends on the material but in general matrix cracking occurs first, followed by delamination and fibre fracture. Fibre fracture most commonly occurs when the stresses in the back of a specimen build up due to bending and the fibres fail in tension.

Using optical micro-graphs Cantwell and Morton [1990] identified the three main damage modes as matrix cracking, delamination and fiber fracture. They also showed that the shape of the damage zone is conical for impact energies above the damage initiation threshold. The cone has an increasing area towards the back of the specimen. Davies and Zhang [1995] also showed that delamination and matrix fracture (or cracking) occurred first, followed by back-face splitting, due to tension, at higher impact energies.

A major shortcoming of most of the studies on impact of composites, however, is the continuous measurement of the force (or any other parameter) during high volocity or ballistics impact events. The knowledge of the complete history the impact event is one of the key requirements for model development. As shown above, current models make use of static force-displacement curves for their input. Thus obtaining the ballistic force-displacement curves will provide additional information to prove or disprove the validity of using static tests to understand ballistic response..

1.2 Measurement Systems

A majority of the measurement systems available today are limited to taking instantaneous, or discrete, velocity measurements during an impact event. These systems include X-ray, high speed photography, streak photography and optical sensors. Optical sensors appear to be the most commonly used type of system for measuring impact velocity. The velocity is merely the time taken to travel between two sensors, usually light emitting diodes (LED's). Variations on the use of LED's include using a 1 mW He-Ne laser to generate two parallel beams of light (Khetan and Chang [1983]) while Cantwell and Morton [1985] used two thin wires instead of light beams.

Another method developed by Zee *et al.* [1989] is a microvelocity sensor. This system is similar to the optical sensors but uses coils. The projectile has a magnet attached and as it passes through a coil it induces a current in the coil. A total of 11 coils, spaced 0.1″ apart, are used. During impact and penetration the magnet in the projectile induces the current in the coils in succession. The output signal is then processed with the use of a specially developed digital

circuitry and the velocity-time history for the impact event is obtained. The number of data points is limited to the number of coils in the system.

The major drawback with discrete measurement systems is that they only provide instantaneous velocity measurements at certain points rather than a continuous measurement. Some of the systems, e.g. high speed photography and X-ray, are also expensive to own and operate.

A more desirable velocity measurement system is one where the velocity during the impact event is measured continuously. A principle that is used by Hodgkinson *et al.* [1982], Gupta and Chiang [1989] and Wu *et al.* [1994] is that of laser interferometry. The principle of laser interferometry is to intersect two coherent laser beams forming an ellipsoidal measuring volume. The beams intersect and form fringes. When the projectile passes through these fringes light of different intensities is scattered. The change in intensity can then be detected using a photodetector. The data is then converted into a velocity-time history for the impact event.

Espinosa *et al.* [1996] used laser interferometry to simultaneously measure the projectile velocity and back face motion of the target. The projectile velocity was measured using a normal velocity interferometer while the target motion was measured using a multi-point normal displacement interferometer. The reflectivity of the back surface of the targets had to be improved by gluing a 0.001 inch mylar sheet and then depositing a thin film of aluminium vapour.

While laser interferometers do provide continuous force-displacement histories for the impact event they are quite costly to purchase and the data reduction can often be quite lengthy. As observed with Espinosa *et al.* there may also be times where the targets have to be enhanced to enable measurement.

A method developed by Delfosse *et al.* [1993] is the instrumented (load cell or accelerometer) low-mass projectile. This system is capable of measuring the force-time history for an impact event. The load cell on the projectile is attached to an oscilloscope with wire leads. This method also requires the removal of the vibrations corresponding to the natural frequency of the projectile. The major drawback with this system is the velocity is limited to 50 m/s. Above this value the wire leads begin to break more frequently resulting in a lost signal.

Based on the above measurement systems there is a definite need for a measurement system that is cost-effective, simple to operate and will provide continuous velocity or displacement measurement during an impact event. One such system was developed by Ramesh and Kelkar [1995] called a Laser Line Velocity Sensor (LLVS). This LLVS is capable of continuously measuring the displacement during an impact event and is used at the Johns Hopkins University for measuring the impact velocity of flyer plates. The system has been further developed at UBC and is discussed in section 2.5.2 and in detail in Appendix A.

1.3 Purpose and Scope

The main focus of this thesis is the experimental investigation of the penetration of carbon fibre reinforced plastic (CFRP) and glass fibre reinforced plastic (GFRP) laminates with conical indenters. The present study attempts to identify the damage modes present in both these material systems and accurately describe the penetration process. This information can in turn be used for modelling the ballistic response of both CFRP and GFRP laminates.

The first goal of this thesis was to develop a measurement system capable of continuously measuring the force during a ballistic test. There is a definite need for a measurement system

that is low cost, requires little or no maintenance and is easy to operate and set-up. With a system which is capable of doing this, the force-displacement curves for a variety of materials can then be obtained. This in turn enables more accurate modelling of the ballistic penetration of composites.

The second goal of this thesis was to investigate the penetration of both CFRP and GFRP laminates by conical projectiles and indenters. The penetration of CFRP is to enable the calibration of a model currently under development at UBC. The main focus is on damage modes present and in particular their progression during penetration. For GFRP laminates the main focus is on the force-displacement curves and the effect of changing test parameters. Once again, identifying the damage modes and damage progression in GFRP is useful for the calibration of analytical and numerical models being developed at UBC.

The experimental set-up is explained in detail in Chapter 2. The testing machines which were used are described as well as a brief description of the principle of operation of the LLVS which has been implemented.

Chapter 3 presents the experimental results of the static penetration of CFRP laminates (IM7 carbon fibre in an epoxy resin). The focus of this chapter is on the initiation and progression of damage. Different areas on the force-displacement curves are highlighted and the damage mechanisms at any one point are identified through optical micro-graphs.

Chapter 4 presents the experimental results of the static and ballistic tests performed on GFRP laminate (S-2 glass phenolic resin). This chapter makes use of the LLVS for obtaining force-displacement curves for the ballistic tests. Trends observed by changing the test parameters are

discussed and comparisons with static tests are made. Once again the damage progression is presented and damage modes identified.

Finally in Chapter 5 conclusions are drawn and areas of future research identified.
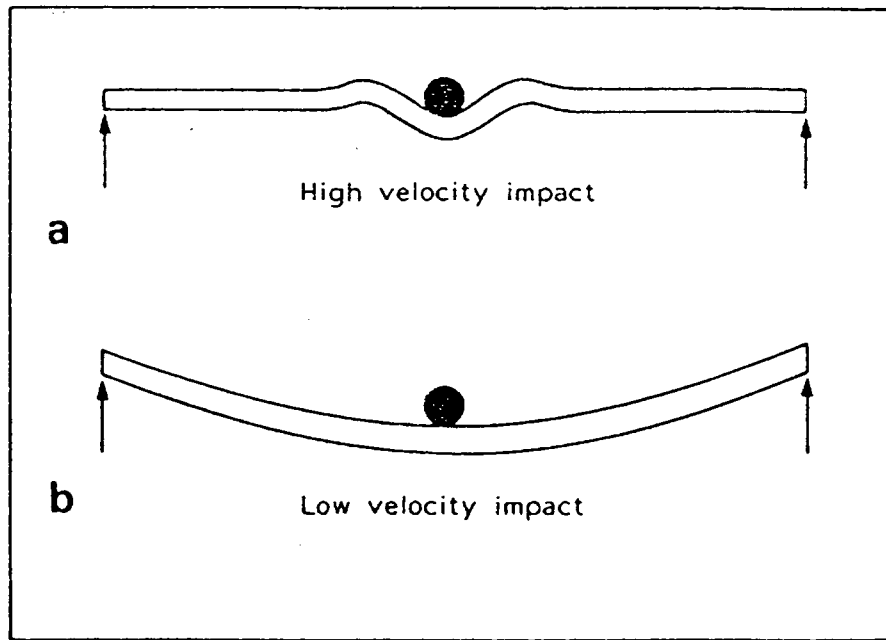
Figure 1.1. Schematic showing the response due to high and low velocity impact (from Cantwell and Morton [1989]).

Chapter Two

Experimental Procedures

This chapter covers the experimental set-up used for the static and ballistic tests on CFRP and GFRP laminates. The specimens, projectiles and indenters, boundary conditions and measurement techniques will be discussed.

2.1 Background

Abrate [1991] and [1994] provides a good summary of the techniques available for generating impact. The most commonly used instruments are the drop weight tower and gas gun. The drop weight provides a high mass low velocity impact (see Figure 2.1). Drop-weight tests, as the name implies, drop a weight onto a specimen. Depending on the amount of energy required for the test, the mass, of the weight or the height from which the weight is dropped can be changed. The lighter mass drop-weight testers tend to be free falling, whereas the heavier mass drop-weight testers are guided by a rail.

The gas gun provides a low mass, high velocity impact (see Figure 2.1). The basic principle of the gas gun is to use compressed air to launch a projectile down a tube. The velocity can be accurately controlled by varying the pressure. Variations on this theme include the use of gun powder to launch the projectile. A powder gun, however, has the disadvantage that unburned

powder and smoke sometimes interfere with any optical measurement systems used during the impact test. The type of gun powder can sometimes adversely influence the repeatability of the velocity, whereas a gas gun typically has good reproducibility for velocity.

The majority of static tests are performed on screw-driven or servo-hydraulic testing machines. The cross head rate on a screw driven testing machine is adjustable from as low as 0.00508 mm/min to 50.8 mm/min. More recently servo-hydraulic testing machines have become popular for performing static tests. Servo-hydraulic testing machines have the advantage that load controlled (as opposed to displacement controlled) tests can be performed. This is advantageous since more control is possible, higher displacement rates can be achieved and more data acquisition is possible.

2.2 Specimens

This study made use of both IM7 carbon fibre reinforced polymer (CFRP) and S-2 glass fibre reinforced polymer (GFRP).

2.2.1 Carbon Fibre Reinforced Polymer (CFRP)

The CFRP panels were manufactured by The Boeing Company in Seattle, WA. The panels were manufactured from IM7 carbon fibres with an 8551-7 epoxy matrix. The layup of the specimens is $[-45/90/45/0/0]_{4s}$ (quasi-isotropic) giving a total of 40 plies. The panels all had a nominal thickness of 6.15 mm and were used to cut specimens with a 50.8 mm x 50.8 mm (2″ x 2″) square geometry.

2.2.2 Glass Fibre Reinforced Polymer (GFRP)

The GFRP panels were manufactured by Sioux Manufacturing Corporation according to military specification MIL-L-64154. The panels were manufactured from S-2 glass plain weave rovings with a phenolic resin matrix. Three panels were supplied measuring 1219.2 mm (6') x 1828.8 mm (8') and with nominal thicknesses of 6.35 mm (0.25"), 12.70 mm (0.50") and 19.05 mm (0.75"), respectively. These panels were used to cut specimens with a 101.6 mm (4") x 152.4 mm (6") rectangular geometry.

2.3 Projectiles and Indenters

This study used four different types of projectiles and two types of indenters. The projectiles were used for ballistic tests while the indenters were used for static tests. Both the indenters and projectiles had conical nose shapes. Complete set of projectiles and indenters used is shown in Figure 2.2. The 37° indenter had a bluntness of 1.5 mm. Both the indenters and projectiles had two cone angles (37° and 120°) while the projectiles also had a *short* and a *long* version. The long projectiles were manufactured to use with the Line Laser Velocity Sensor (see section 2.5.2.1), so that the back of the projectile could be tracked. All the projectiles and indenters were manufactured from 4340 steel and were sufficiently hardened to $30R_c$ to prevent deformation of the tip during impact.

2.4 Boundary Conditions

Three different boundary conditions (backing plates) were used for this study. A rigid steel plate was used during the static indentation tests on GFRP specimens. A 25.4 mm (1") circular

opening was used for the CFRP specimens in static deflection tests. A 76.2 mm (3″) x 127.0 mm (5″) rectangular opening was used for the GFRP specimens in both static deflection and ballistic tests. In the ballistic tests the backing plate had clamps to hold the specimen in place. A schematic area of both backing plates is shown in Figure 2.3.

2.5 Testing Machines

This study made use of an Instron screw-driven testing machine for static testing and a powder gun for high velocity, or ballistic, testing.

2.5.1 Instron Testing Machine

The Instron (model TTDL) screw-driven testing machine uses a load cell and linear voltage displacement transducer (LVDT) to obtain a force-displacement history for static deflection and static indentation tests. The load cell has a rated capacity of 89 000 kN (20 000 lbs) while the LVDT (model SANGAMO DCR 15) has a displacement range of 30 mm. Data acquisition was done with an application developed in-house using the National Instruments LabView software package.

All the static tests performed on CFRP and GFRP were done at a cross head rate of 0.1″/min. The tests were recorded using a video camera and a digital display was used which displays the load and displacement in voltage. The display was recorded on the video screen during the tests. By knowing both the load and displacement simultaneously it is possible to determine where on the force-displacement curve a particular event happens. The Instron testing machine set-up is shown in Figure 2.4 with the LVDT, indenter, specimen, backing plate and display shown.

A piece of conductive foam was also used during the static deflection tests to determine when perforation occurs. This foam was inserted on the back face of the specimens forming an open circuit with the indenter. When the indenter touched the foam the circuit was closed, and the exact point of perforation could be determined. This is useful to know when comparing perforation energies from static and ballistic tests.

2.5.2 Powder Gun

The components of the powder gun are the universal receiver, barrel, blast deflector, measurement system, break screens and catchment chamber as shown in Figure 2.5.

The .308 Winchester rifle barrel attaches to the universal receiver of the powder gun. The projectiles are loaded into Winchester .308 brass casings before being loaded into the barrel. The energy, and hence velocity, of the projectile is a function of the charge, or amount of gun powder, in the casing. The amount of gun powder is measured in grains and Figure 2.6 shows the linear relationship between energy and grains. The powder used in this study was Bullseye® which is a high energy powder manufactured by Hercules Incorporated. Once the projectile was loaded into the barrel the firing pin was inserted and was activated remotely using a solenoid switch.

To reduce the amount of smoke and unburned powder that might interfere with the measurement system a blast deflector was installed at the muzzle of the barrel.

The velocity during impact is continuously measured using a Line Laser Velocity Sensor (LLVS) based on the system originally developed by Ramesh and Kelkar [1995] at the John's Hopkins University. Ramesh used the LLVS to continuously measure the impact velocity of flyer plates. Using the same principle as Ramesh, the LLVS was implemented at UBC. The only difference is

that the system at UBC is used to measure velocities during the impact. The principle of operation of the LLVS, calibration of the LLVS, data reduction and some data from ballistic tests are discussed below in sections 2.5.2.1 through 2.5.2.4. A more detailed discussion of the LLVS can also be found in Appendix A.

The residual velocity of a projectile is always important to know to determine how much energy a target absorbs during an impact event. To measure residual velocity a break screen set-up was used that measured the time taken to break two parallel conductive screens set a distance of 150 mm apart. As the projectile broke the first screen the voltage dropped and triggered the oscilloscope. As the projectile broke the second screen there was a second voltage drop. The time taken to travel 150 mm was then measured between these two drops. The catchment chamber was used to stop projectiles with residual velocities.

2.5.2.1 Principle of Operation of the LLVS

Figure 2.7 shows a schematic of the LLVS. This set-up was for a projectile of length 46.0 mm. The original projectiles had lengths of 20 mm which meant the back of the projectile could not be tracked during an impact. Thus 26 mm was added to the new projectiles giving them a length of 46.0 mm.

The light is emitted from the diode laser (labelled 1 in Figure 2.7) as a sheet which diverges in the horizontal and vertical planes. The first of two cylindrical lenses (labelled 2 in Figure 2.7) collimates the sheet in the horizontal plane, while the second lens (labelled 5 in Figure 2.7) collimates the sheet in the vertical plane. An aperture (labelled 3 in Figure 2.7) and a neutral density filter (labelled 4 in Figure 2.7) are placed between the first and second cylindrical lens to

block out the edges and reduce the intensity of the sheet respectively. The sheet is then focused by a collector lens (labelled 6 in Figure 2.7) on to the active area of the photo-detector (labelled 7 in Figure 2.7) which converts the intensity of the sheet into a voltage.

There is now a sheet of light of uniform width intensity. Figure 2.7 shows a projectile in five different positions labelled A, B, C, D and PoI. The corresponding voltage-time curve is shown in Figure 2.8 with the positions from Figure 2.7 labelled. The projectile starts out of the sheet at position A and the oscilloscope shows full voltage, or 100 % intensity. As the projectile moves from position A to B it blocks out the sheet and the intensity drops in proportion to the amount of light blocked. At an intensity of 0 % the voltage, however, does not drop to 0 V since the photo-detector registers background light. From B to C there is a null period where the intensity of the sheet stays constant at 0 %. Since the projectile is longer than the sheet it continues to block out the sheet until the back end of the projectile reaches the front of the sheet, i.e. from B to C in Figure 2.8. This causes the null period in the voltage-time reading (B to C in Figure 2.8). From position C to D the projectile leaves the sheet causing the intensity to rise with a corresponding rise in voltage. The fifth position is labelled PoI (Point of Impact) and is the point at which impact occurs.

2.5.2.2 Calibration

Theoretically the intensity of the laser sheet should be uniform across the width. In practice this was found not to be the case. There was a slight non-uniformity in intensity from one side of the sheet to the other. Therefore the calibration relating voltage to displacement was not linear. This is quite clear from Figure 2.9. The non-uniformity also affects the calibration to the extent that two calibrations are needed for the system. These calibrations are referred to as the *calibration*

into the sheet and the *calibration out of the sheet* and represent the projectile entering the sheet (A to B in Figure 2.7) and the projectile leaving the sheet (C to D in Figure 2.7) respectively. The two calibrations are shown in Figure 2.9 and both the non-linearity and difference is quite clear.

It is possible to have a linear or even a polynomial function relating voltage to displacement. The drawback with this approach is that the original calibration data is not used in relating voltage to displacement. This implies that error is introduced into the data reduction very early on in the process. A better approach is to use a look-up table. As the name suggests this technique takes a voltage and looks-up the corresponding displacement from the calibration curve. If a value falls between two values in the calibration (as most do) then the value is found by linearly interpolating between the two points. This method ensures that the final displacement-time curve always reflects the original calibration.

2.5.2.3 Data Reduction

The data reduction was performed using a Microsoft EXCEL Visual Basic Module. The module was written using user defined functions and standard EXCEL commands to calculate velocities and accelerations. The module is executed in two parts. The first part reads in the 5000 raw data points acquired from the oscilloscope and converts these values into voltages. A sample voltage-time curve is shown in Figure 2.8. The user then inputs the times corresponding to points A, B, C and D in Figure 2.8 and the voltages are converted to displacements using the look-up table. The initial or striking velocity is calculated between points A and B in Figure 2.8. The data set is then reduced to contain only *impact data*. The *impact data* occurs between points C and D in Figure 2.8. Depending on the distance of the sheet from the target, impact could occur anywhere

between C and D in Figure 2.8. The closer the target is to the sheet the closer to point C impact will occur. It is even possible for impact to occur at point B in Figure 2.8. The point of impact (PoI in Figure 2.7 and Figure 2.8) is the point at which the projectile displacement is initialised to zero.

The reduced data set, or impact data set, is then converted into velocities by differentiating the velocity-time curve. The differentiation is done by fitting a straight line to the displacement data. The slope of the displacement data set then gives the velocity. A second differentiation gives the acceleration and from this the force is calculated. By cross plotting force and displacement the force-displacement history of the event is obtained.

It should be noted that the data reduction creates some error. The original data reduction took every second data point. If the data set was made up of odd values (1st, 3rd ,..... point) of the raw data then the data reduction gave a slightly different output than if the data set was made up of even values (2nd, 4th ,..... point). A comparison between results obtained using odd values, even values and all the values is shown in Figure 2.10. There are two areas on this velocity-time curve where the values differ. These are between 40 and 70 μs, and 170 and 240 μs. The velocity values differ by no more than 10 m/s. Due to the nature of the line fit in the data reduction the difference is magnified causing the difference shown in Figure 2.11 between 3 and 6 mm and 18 and 19 mm. From this curve it is also clear that by using all the values in the data reduction the error is minimised. Using all the values is close to an average of using every odd and every even point as shown in Figure 2.12.

It is quite clear that using all the raw data points minimises the error. All the tests used in this study were therefore analysed using the full set of 5000 raw data points.

2.5.2.4 Representative Output

This section shows the data reduction process used on all the ballistic tests used for this thesis. A more detailed analysis of each individual test is covered in section 4.4 and this example covers the basic operation of the data reduction.

A representative ballistic test performed on a 12.70 mm (0.50″) GFRP specimen is now presented. The projectile was 46.0 mm long, weighed 13.2 g and had a 37° cone angle. The striking velocity was 171 m/s and the projectile came to a complete stop in the target giving an energy absorption of 193 J. Each of the outputs from the data reduction program will be discussed.

The displacement-time curve is shown in Figure 2.13 with 3 points labelled A, B and C. From A to B the projectile was penetrating the target and at point B it came to a complete stop. From point B to C in Figure 2.13 the plate was moving with the projectile embedded in it. At point C the plate too came to a complete stop. To analyze this data set, the displacement-time curve was divided into two sections. The first is the projectile and local plate displacement from point A to B and the second is global plate displacement from point B to C.

The velocity-time curves for the projectile and plate are shown in Figure 2.14 and Figure 2.15 respectively. Impact occurs at 24.8 µs and the projectile slowed down immediately. After 240.2 µs the projectile came to a complete stop relative to the plate giving an impact event duration of 215.4 µs.

After the projectile had stopped the target continued to move in the projectile direction for an additional 41.4 μs before changing direction. The target finally came to rest 625.2 μs after impact.

Figure 2.16 shows the results of the representative ballistic test and an additional ballistic test for comparison. The ballistic tests had striking velocities of 171 m/s and 304 m/s respectively. The residual velocities were 0 m/s and 200 m/s respectively. There is also good repeatability between the tests. These curves will be discussed further in section 4.4.

Figure 2.17 shows the acceleration in the plate once the projectile had come to a complete stop. Since there is no external force acting on the plate, this acceleration is the free vibration of the plate.

The energy-displacement curve for the impact event is shown in Figure 2.18. The peak energy is 195 J which compares very well with the incident projectile energy of 193 J.

2.6 Post Test Analysis

Once the CFRP and GFRP specimens were tested they were sectioned so that the damage could be identified. The CFRP specimens were cut along the 0° fibre direction while the GFRP specimens were cut along the width. The CFRP specimens were then polished using 180, 320 and 600 grit sandpaper and were finely polished on a 5 micron diamond wheel. The GFRP specimens were polished using 180 and 320 grit sandpaper only. The GFRP specimens were initially polished in the same way as the CFRP specimens. It was found, however, that polishing beyond the 320 grit sandpaper did not improve the quality.

The CFRP specimens were then examined under the microscope and optical micrographs were taken to show the extent of damage. The images were digitised and the position of the boundary conditions on the micrographs were marked as solid black lines. The GFRP specimens were examined using photography instead of microscopy since better contrast and lower magnification were needed. Once again, the images were digitised.
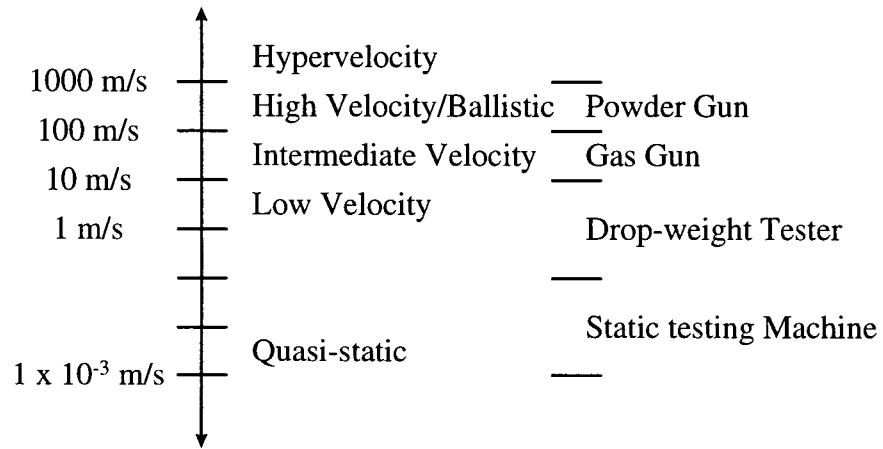
Figure 2.1. Standard velocity classifications for impacts by foreign objects.
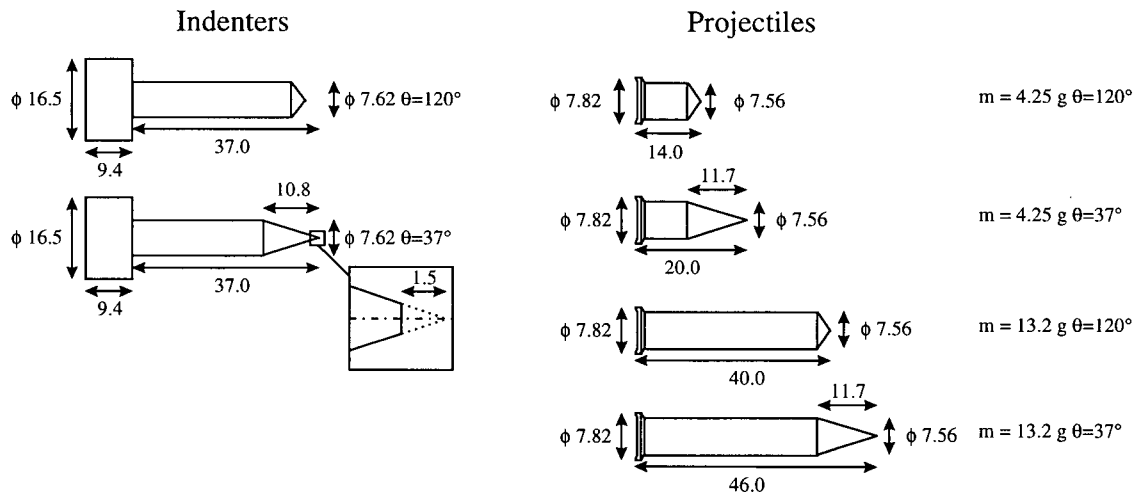
Figure 2.2. Figure showing indenters and projectiles used in the tests (units are in mm).
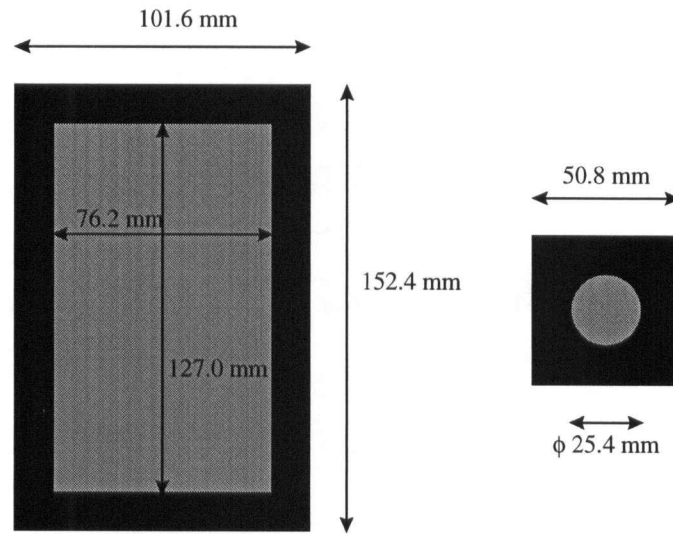
Figure 2.3. Schematic showing backing plate dimensions. (The black area represents the specimen and the grey represents the opening).
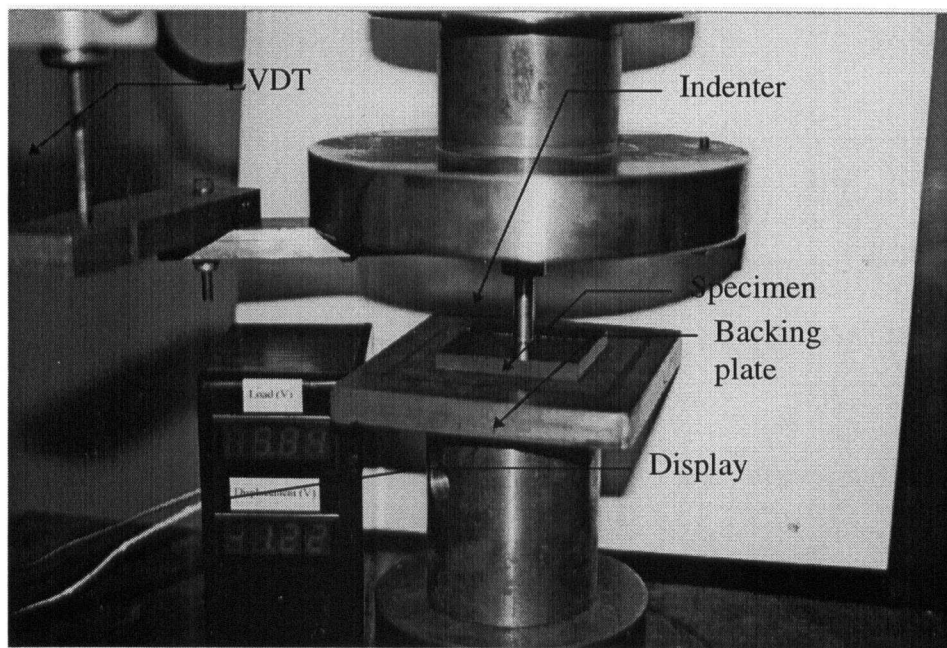
Figure 2.4. Instron screw-driven testing machine set-up showing LVDT, indenter, specimen, backing plate and display.
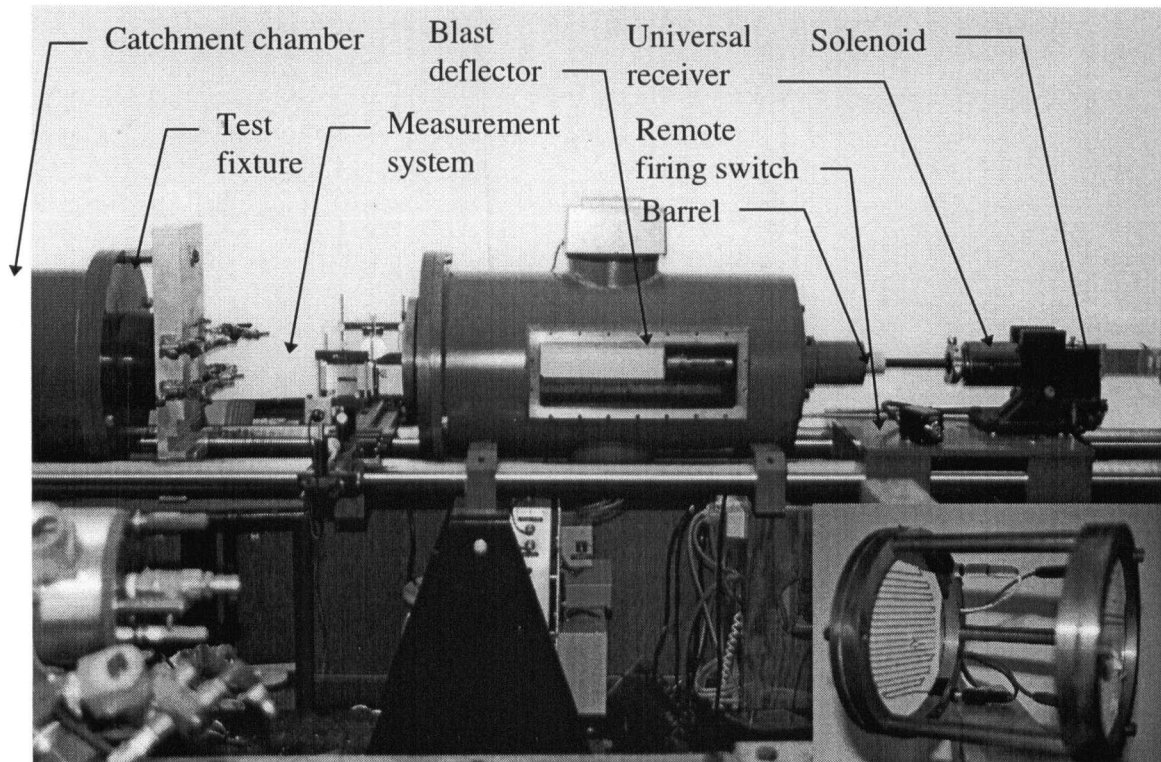
Figure 2.5. Powder gun set-up showing solenoid, universal receiver, barrel, remote firing switch, blast deflector, measurement system, test fixture and catchment chamber. The break screens are shown in the inset.
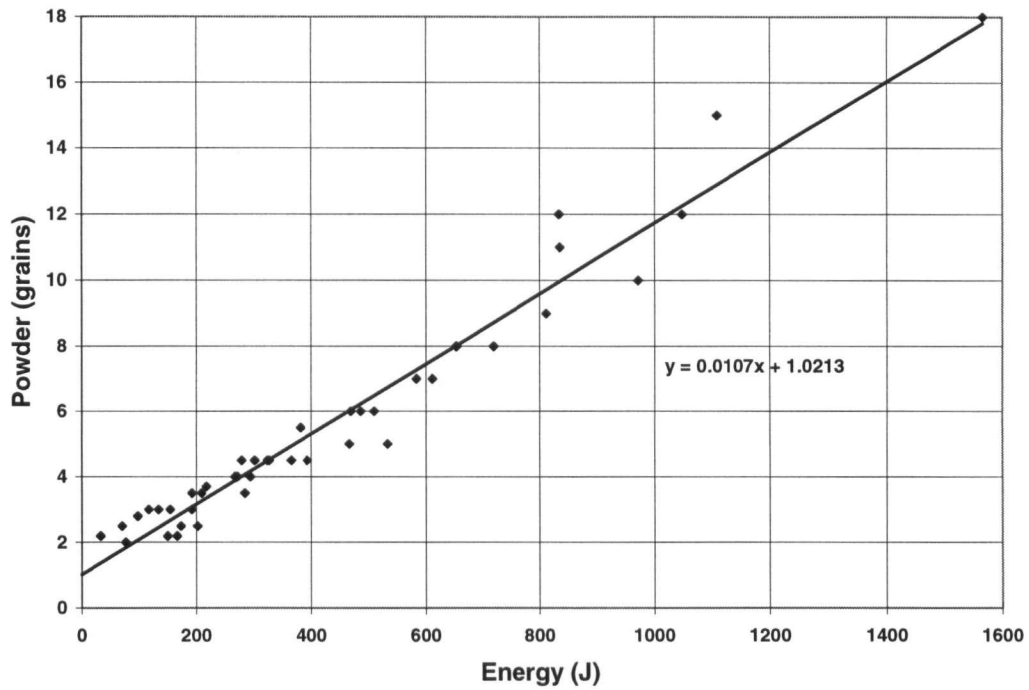
Figure 2.6. Curve used to determine the amount of powder needed for a specific energy. Although the energy is the dependent variable, in practice the impact energy is known, and the amount of powder required for that energy is unknown.
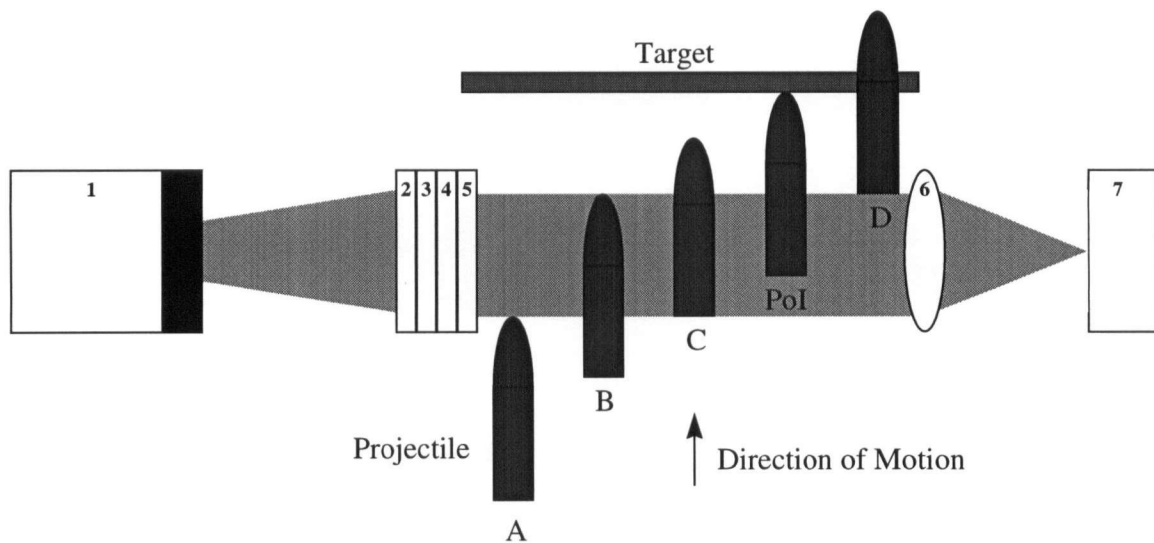
Figure 2.7. Schematic of the LLVS showing diode laser (1), cylindrical lens (2), aperture (3), neutral density filter (4), cylindrical lens (5), bi-convex lens (6) and photo-detector (7).
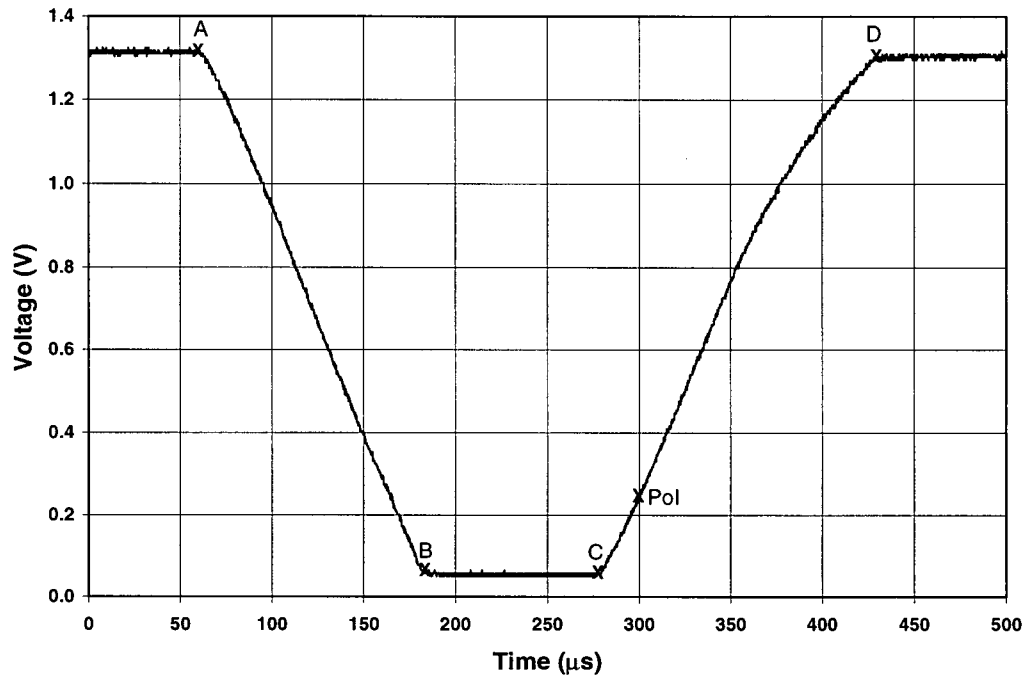
Figure 2.8. Sample output from the first part of the data reduction module.
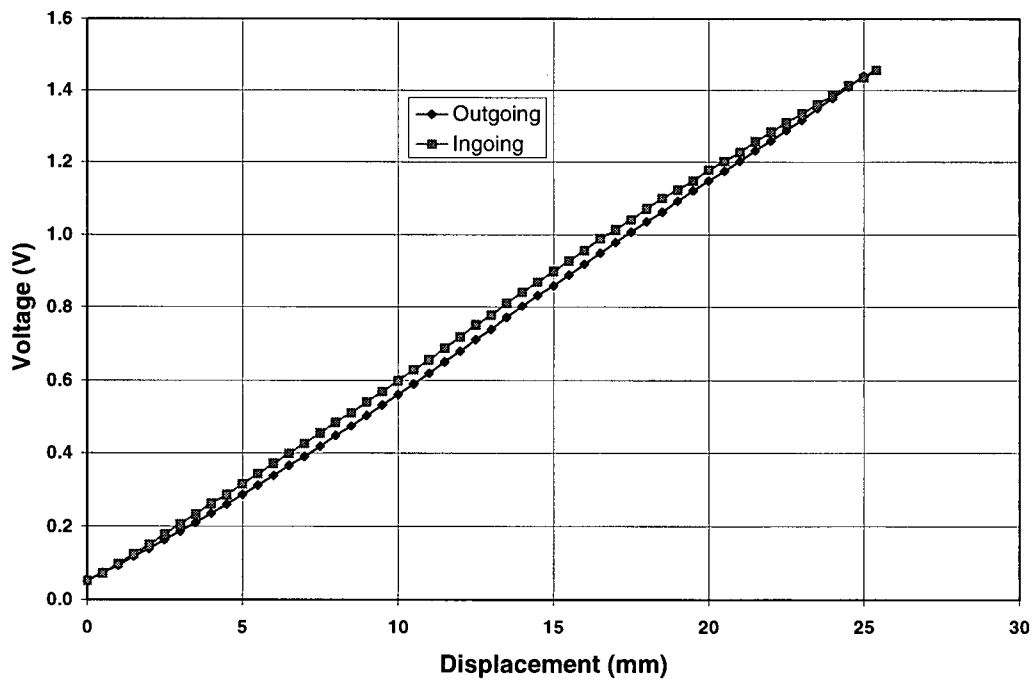
Figure 2.9. Curve showing the two calibration curves (note: these are two *different* curves and the effect is *not* due to hysteresis).
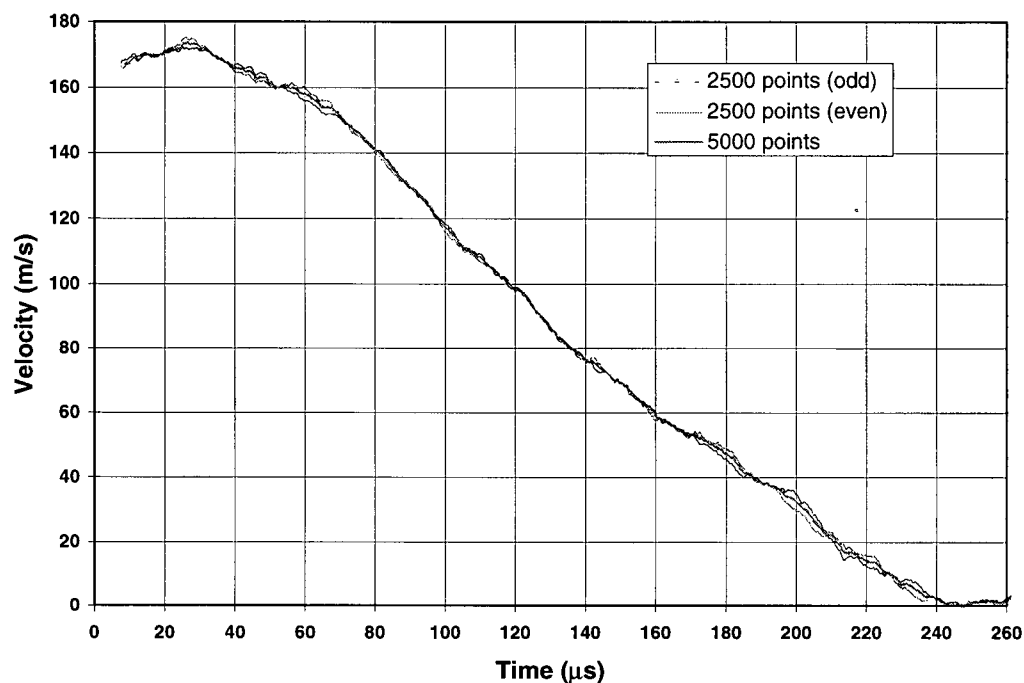
Figure 2.10. Velocity-time curve showing effect of taking every second odd, every second even and every data point.
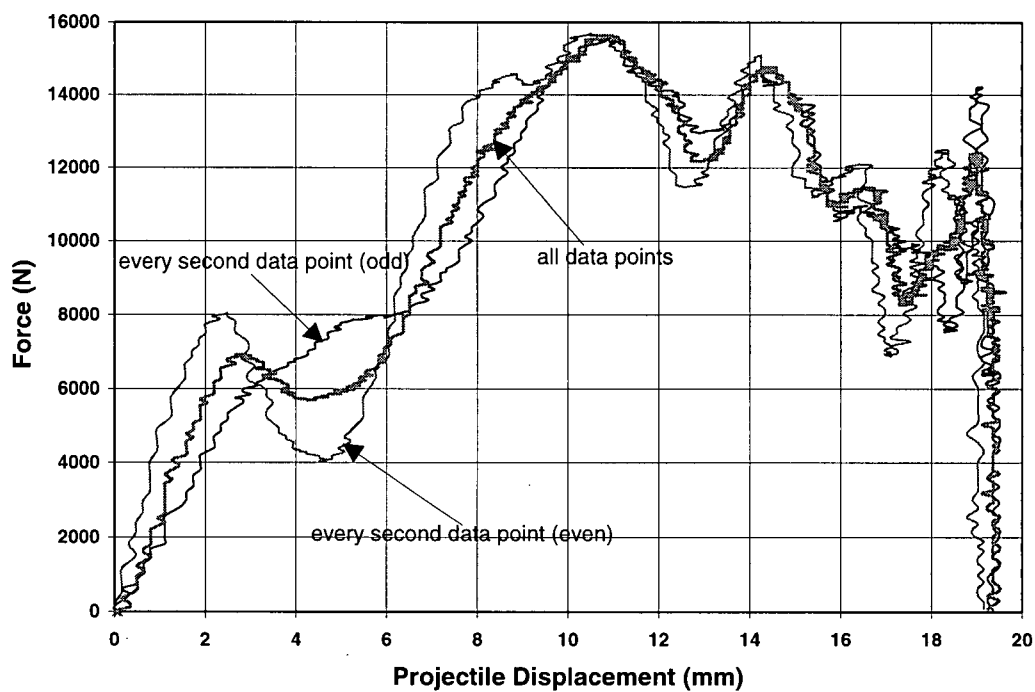
Figure 2.11. Force-displacement curve showing effect of taking every second odd, every second even and every data point.
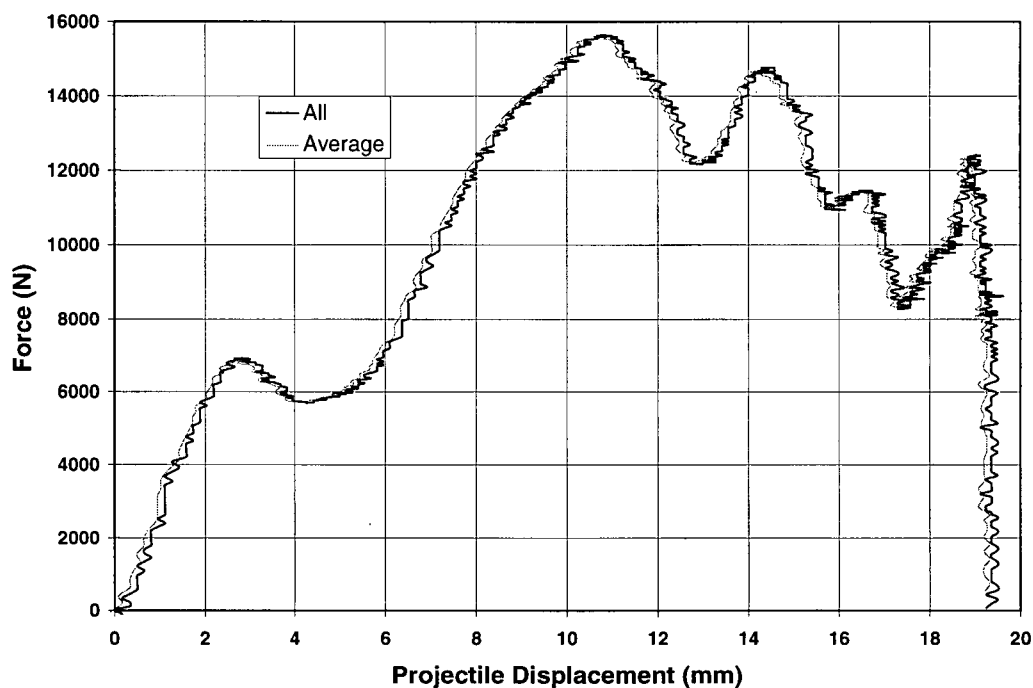
Figure 2.12. Force-displacement curve showing the comparison between using every data point, and the average between every second odd and every second even data point in the data reduction.
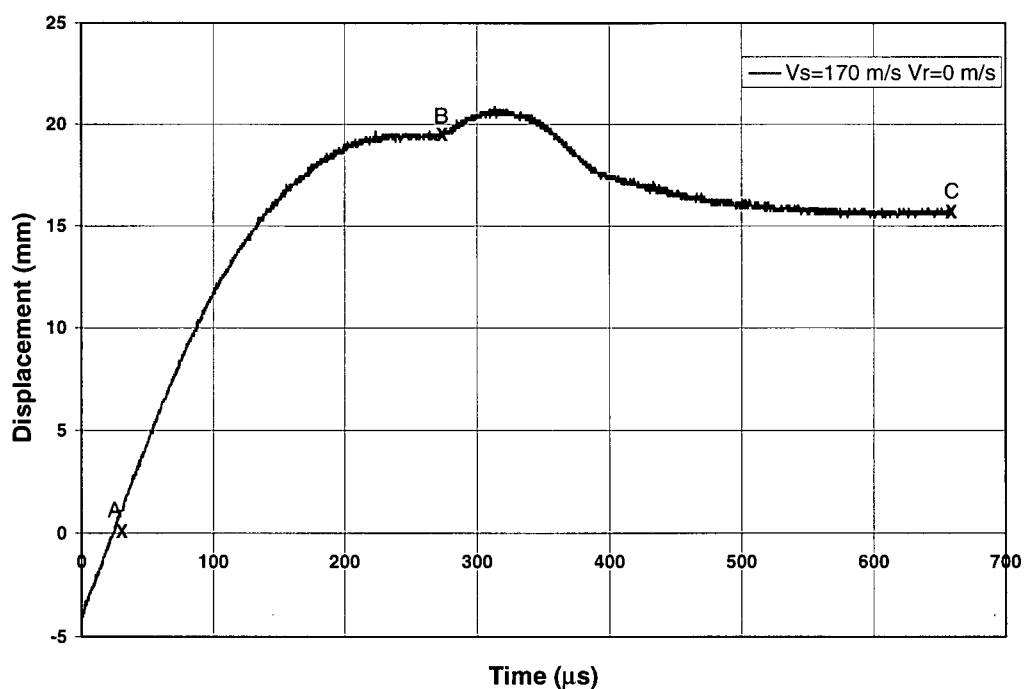
Figure 2.13. Representative displacement-time curve for a ballistic test.
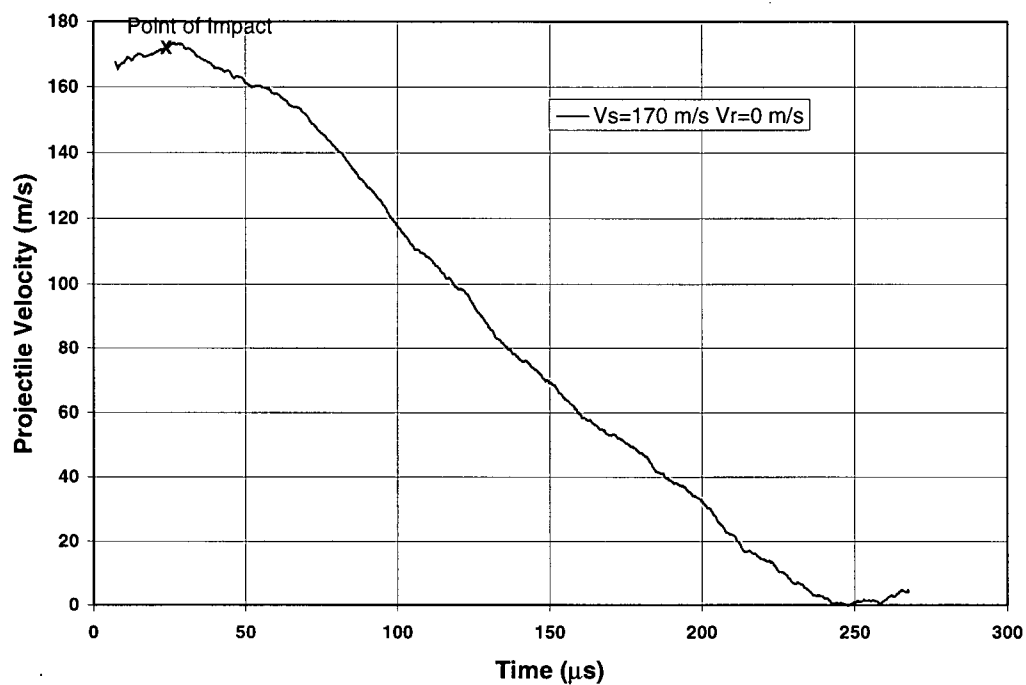
Figure 2.14. Representative velocity-time curve for the projectile.
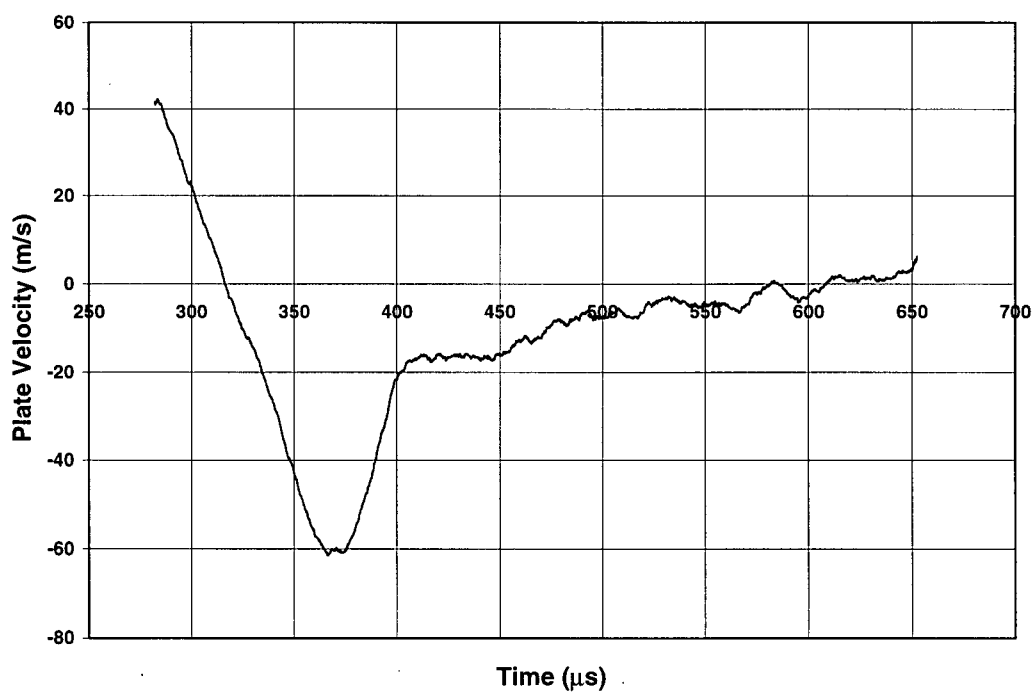
Figure 2.15. Velocity-time curve for the target.
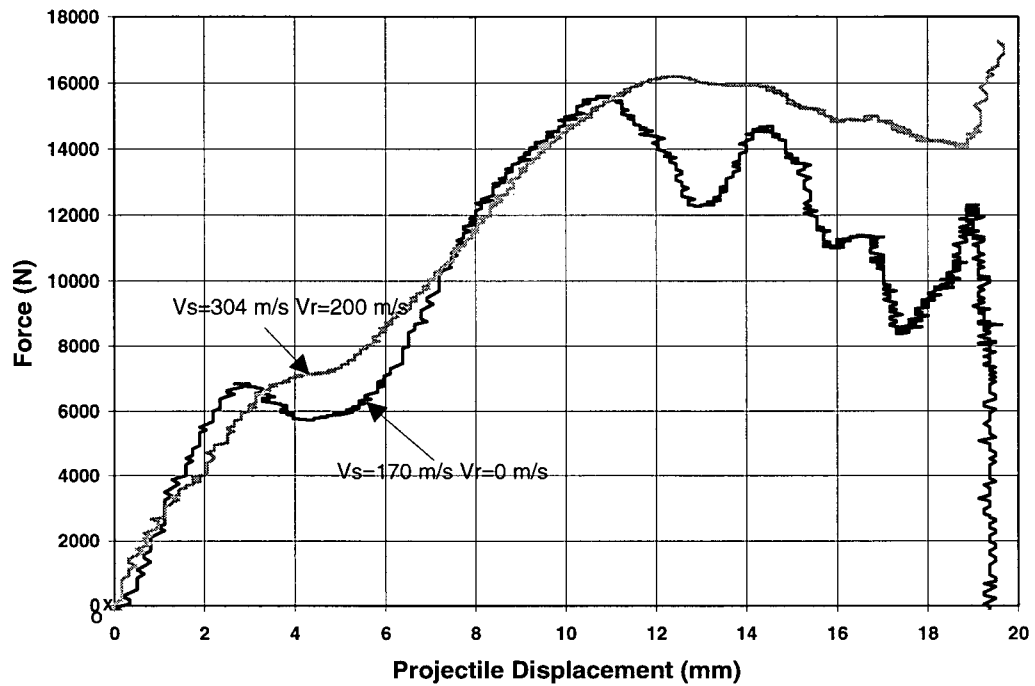
Figure 2.16. Representative force-displacement curves for a ballistic impact.
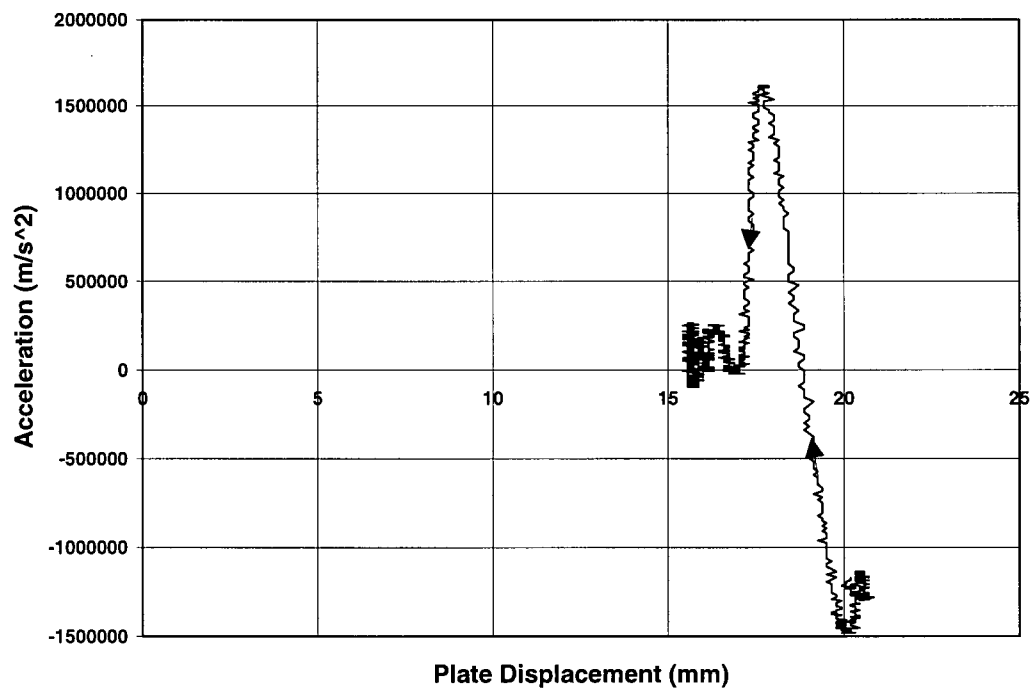
Figure 2.17. Curve showing the acceleration in the target after the projectile has come to a complete stop.
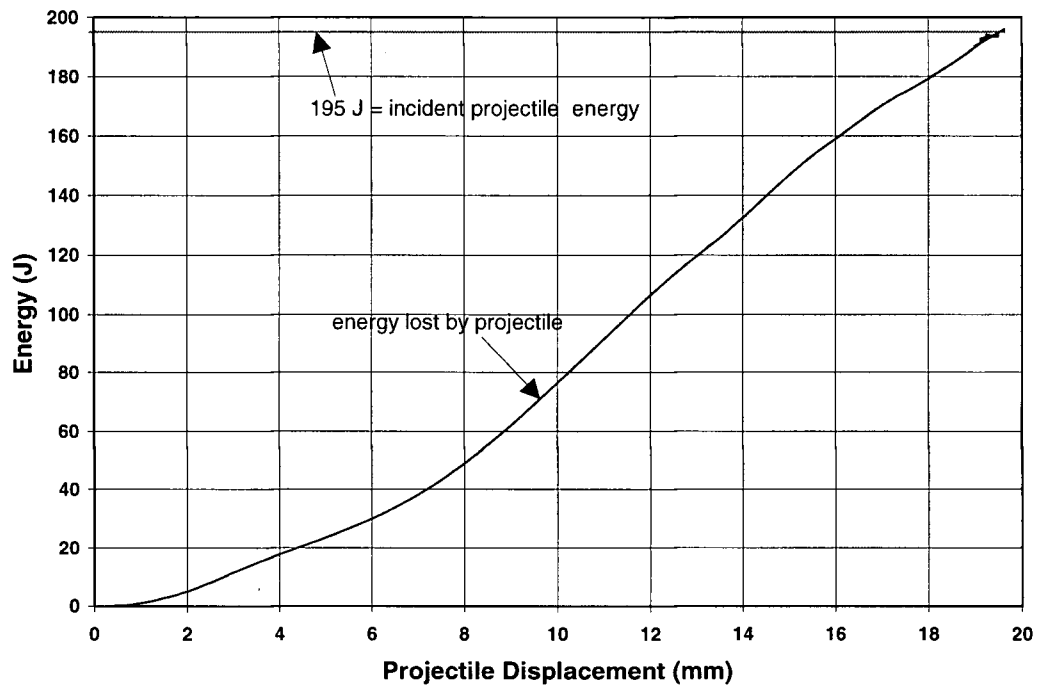
Figure 2.18. Comparison of the energy lost by the projectile to the incident projectile energy.

Chapter Three

Static Penetration of CFRP Laminates

3.1 Background

Most authors agree that for CFRP laminates, the ballistic response can be predicted based on the static penetration. Lee and Sun [1993a] performed a series of static tests on Hercules AS4/3501-6 carbon/epoxy with a quasi-isotropic layup. They used blunt nosed indenters and stopped the test at key points along the curve to examine the damage evolution in more detail. In this way the progression of damage was clearly defined. They found that matrix cracking was the initial damage mode followed by delamination and eventually plugging. They also performed preliminary ballistic tests and found the ballistic failure modes were similar to the static tests. A model was then formulated using the static force-displacement curve to characterize the penetration process.

Using this model Lee and Sun [1993b] predicted the ballistic limit of quasi-isotropic AS4/3501-6 laminates and compared these predictions with ballistic tests. The results showed good agreement and they postulated that as long as the damage modes in static and ballistic tests are similar the model should be valid. Under such conditions it is possible to predict a ballistic response of a specimen without actually having to do a ballistic test.

Cantwell and Morton [1989] and [1990] performed both low and high velocity impact experiments on Grafil XA-S fibres in Ciba-Geigy BSL914C epoxy resin with balanced lay-ups. The indenter was hemispherical. They, like Lee and Sun, also found similarities in damage progression between static and ballistic tests. Initiation of damage was in the form of matrix cracks with delamination and fibre fracture following at higher impact energies. The delaminated zone was found to be conical in shape with the area increasing towards the back surface.

Ursenbach [1995] studied the penetration of CFRP laminates by blunt indenters. Both static deflection tests and impact tests were performed on T300H/F593 CFRP. Three stages were identified during the penetration. Stage I was elastic loading followed by a load drop, stage II had a reduced stiffness and a second load drop characterising complete failure. The final stage, stage III, was the ejection of a plug. Impact tests produced a peak load twice that of the static tests. It was, however, also shown that impact tests followed the static indentation very closely indicating that the dynamic response approached the static indentation curve. The damage in the two cases was also found to be similar indicating that the information used in the static tests could be used for the higher velocity tests.

Clearly most of the research into the penetration of CFRP has been using blunt penetraters. Delfosse and Poursartip [1995] and Delfosse [1994] looked at the effect of the nose shape of the indenter on the perforation energy of IM7/8551-7 CFRP. They compared blunt, hemispherical and conical (37°) nose shapes and found that the blunt indenters had the lowest perforation energy while conical indenters had the highest perforation energy. They also found that the blunt indenters caused the highest peak force but the conical indenters had the highest indenter

displacement. From this we can conclude that blunt projectiles are the most threatening to CFRP.

Goldsmith *et al.* [1995] studied the static, dynamic and ballistic perforation of woven T300/934 CFRP by 60° indenters/projectiles. The thickest specimen was 6.6 mm with a total of 20 plies. The static tests were done using an Instron universal testing machine, the dynamic tests were performed on a gas gun and the high velocity tests used a powder gun. In addition to matrix cracking, delamination and fibre fracture petal, bending was also observed and found to be quite significant. The cone of delamination described by Cantwell and Morton [1990] was also observed by Goldsmith *et al.* but does not extend as far due to the indenter/projectile cone angle. A model was developed based on the experimental results and the results compared to the experiments. The resulting model predicts the perforation energies for the limited ballistic data quite well. For the static predictions the agreement deteriorates as the thickness is increased. One final comparison was made between carbon fibre reinforced polymer (CFRP) and kevlar fibre reinforced polymer (KFRP). The results showed that KFRP is a far superior material at stopping pointed projectiles than CFRP.

3.2 Test Matrix

A total of 8 static deflection tests were performed for this thesis. The test matrix includes an indenter cone angle of 37° and a specimen thickness of 6.15 mm. Table 3.1 shows the test matrix for the static tests performed on CFRP laminates.

Specimens qs-sd-07c and qs-sd-08c were also strain gauged on the back face, in the fibre direction (-45° direction) with Micro-Measurements EA-09-230DS-120 strain gauges.

3.3 Results from Static Deflection Tests

Figure 3.1 shows the load-displacement curves for all the tests. Clearly the test results are fairly repeatable. There are eight points labelled A through H which correspond to the 8 static tests on CFRP. A simple representative curve for the static penetration of CFRP is shown in Figure 3.2. Points A through H are once again labelled with the corresponding comments. Point O to A in Figure 3.2 represents the elastic bending of the plate, point B is the onset of bulging with matrix cracks initiating between points B and C. Point C is the onset of delamination. Point F corresponds to back face damage initiation and also the point at which a *major* load drop occurs.

3.3.1 Elastic Bending

Point O to A in Figure 3.2 represents the elastic bending of the plate. There is no permanent back face deformation after the specimen is unloaded at point A indicating that all the energy is expended in plate bending rather than a combination of plate bending and other energy absorbing mechanisms.

3.3.2 Penetration

At point A in Figure 3.2 there is a change of slope of the load-displacement curve. The micrograph corresponding to this point is shown in Figure 3.3 and clearly shows that the change of slope is due to the start of penetration. The top two plies have been penetrated and thus the structure is softened which causes the change of slope in the load-displacement curve. Further evidence can be seen by looking at the load versus the back face strain curve in Figure 3.4. Point A corresponds to a change in slope on the curve indicating that the structure has softened and penetration has started.

At point B there is a small change in the slope of the load versus the back face strain and the load-displacement curves. This change is shown quite clearly by cross-plotting the back face strain vs indenter displacement in Figure 3.5. Point O to B in Figure 3.5 represents the global bending of the specimen.

At point A in Figure 3.4 there is a change of slope in the curve that is not seen in Figure 3.5. Since Figure 3.5 shows the back face effects, the effect at point A must be happening far from the back face, i.e. on the front face. Thus point A corresponds to the start of penetration.

3.3.3 Bulging

At point B in Figure 3.5 the change in slope is due to a local effect on the back face of the specimen. The back face strain starts to increase faster and this is the onset of bulging. From B to C work is done in increasing the size of the bulge and this is the mechanism which is dominant. Figure 3.6 shows the micro-graph for this point and clearly the bulging has started. Another indication that the dominant mechanism is bulging comes from a comparison of the change in strain due to bulging to the measured change in strain.

The change in strain due to the bulge is calculated by assuming the bulge is spherical. Then from Figure 3.7

$$s = R\theta, \qquad \Delta\varepsilon_{bulging} = \frac{s-d}{d}, \qquad \cos\frac{\theta}{2} = \frac{R-h}{R} \qquad \text{and} \qquad R^2 = (R-h)^2 + \left(\frac{d}{2}\right)^2 \quad (3.1)$$

where s is the arc length, and d and h are the bulge diameter and height respectively. Substituting for s and simplifying R and θ gives

$$\Delta\varepsilon_{\text{bulging}} = \frac{R\theta - d}{d} \tag{3.2}$$

$$R = \frac{4h^2 + d^2}{8h} \quad \text{and} \quad \theta = 2\cos^{-1}\left[\frac{R-h}{R}\right] \tag{3.3}$$

Substituting R and θ in equation (3.2) gives

$$\Delta\varepsilon_{\text{bulging}} = \frac{\left(4h^2 + d^2\right)\left(\cos^{-1}\left[\frac{d^2 - 4h^2}{d^2 + 4h^2}\right]\right)}{4hd} - 1 \tag{3.4}$$

Using the values of d and h from Table 3.4, the strain due to bulging can then be calculated from equation (3.4). The measured change in strain, $\Delta\varepsilon$, is calculated from Figure 3.8. This curve is an idealised form of Figure 3.5. The comparison between the calculated and measured change in strain is shown in Figure 3.9. The agreement between the calculated and measured change in strain is not very good if the bulging is assumed to begin at point B. If, however, bulging is assumed to begin at point A, the agreement between the calculated and measured change in strain becomes reasonable. Thus it would appear that bulging begins at point A and not point B.

From point C onwards in Figure 3.9 the change in strain remains constant. The bulging increases at a constant rate but there is a new mechanism which starts and is more dominant than the bulging effects.

3.3.4 Matrix Cracks

Matrix cracks are the second type of damage found in the specimens. Figure 3.10 shows matrix cracks that pass transversely through the layers. These matrix cracks initiate somewhere in the

laminate and then grow until they reach an interface between two plies. The angle (45°) of the matrix cracks indicates that the matrix cracks are formed by shear stresses and not bending stresses which would cause vertical matrix cracks.

Matrix cracks are identified by many authors as the initial form of damage. Most authors also propose that although delamination is the major damage mode, it cannot exist without matrix cracks. Choi *et al.* [1991a], [1991b], [1991c] and Jih *et al.* [1993] identified two types of matrix cracks. These are shown in Figure 3.11 and are transverse shear and bending cracks. Transverse shear cracks occur slightly away from the impact sight and at an angle of approximately 45°. The inclination of the matrix cracks is due to the combination of the interlaminar shear stresses and the transverse normal stress. Bending cracks occur at 90° and are the result of stresses caused due to plate bending. Matrix cracks initiate somewhere in the laminate and grow. When they reach the interface of two plies they become critical and delamination starts. Delamination always occurs between plies of different fibre orientation and never between plies having the same fibre orientation.

3.3.5 Delamination

At point C there is no change in the load versus the back face strain curve but there is a change of slope in the load-displacement curve indicating that something is happening away from the back surface where the strain gauge is located. This point is also when the first audible 'tick' is heard. Figure 3.10 which was previously used to show matrix cracking, also shows the micro-graph for point C. Delaminations have started and thus point C is the onset of delamination. This is also consistent with Figure 3.9 where at point C it was shown that the damage mechanism changed.

At point C the matrix cracks have reached the interface between the plies and as described previously become critical matrix cracks, leading to delamination.

There are 4 delaminations which occur at this indenter displacement. They occur at depths of 2.69 mm, 3.92 mm, 4.61 mm and 5.30 mm in a 6.15 mm thick specimen. In other words the delaminations occur in the lower 3.46 mm of the specimen. These delaminations are labelled I through IV respectively and are shown schematically in Figure 3.12 and are tabulated in Table 3.2. Figure 3.12 also shows schematically the interface at which delaminations start and how they grow. From this schematic the first delamination starts at the 90/45° interface and then grows along the 45/0° interface while the other 3 delaminations all start at the 90/-45° interface and grow along the -45/0° interface.

The damage state corresponding to point D in Figure 3.2 is shown in the micro-graph in Figure 3.13. The delaminations that started at point C have grown. It is interesting to note the symmetry of the delaminations about the transverse centreline. From Figure 3.13 it is clear that the delaminations always occur between the same interface on both sides of the centreline.

Table 3.3 shows the delamination diameter for each delamination at points A through H. An average delamination diameter is assumed due to the symmetry of the specimen.

Two postulates can be envisaged relating to the initiation of matrix cracks and hence the onset of delamination. The first is that as the indenter penetrates, it cuts through the plies and as it does so it builds up debris ahead of the indenter tip. The indenter is now 'blunted' and is not as efficient as it was initially and shear stresses start to build up ahead of the indenter. This is much like what happens when an originally blunt indenter penetrates the specimen (Ursenbach [1995]).

This action softens the structure allowing matrix cracks to form and grow. The second theory is that as the indenter penetrates, it reduces the effective thickness of the laminate and forms a 'sub-beam'. When the sub-beam is thin enough it bends and matrix cracks are formed. The matrix cracks were shown to be due to shear stresses, and the second theory would suggest that matrix cracks are formed at 90°, which clearly is not the case. Therefore, it would appear that as the indenter penetrates it becomes 'blunted' and the matrix cracks initiate due to the resulting transverse shear stresses.

Audible 'ticks' continue just after point D and through to point E where a louder 'tick' is heard and then at point F where a loud 'bang' is heard. From point F through to point H 'ticks' are heard constantly.

Point E in Figure 3.2 is shown in the micro-graph in Figure 3.14. Quite clearly all the delaminations have grown and no new major delaminations are present. This specimen was also strain gauged on the back face in the fibre direction. The maximum strain reached was 1.9% at point E.

3.3.6 Back Face Damage

From point E (Figure 3.14) to point F (Figure 3.15) the damage mechanism changes quite quickly. The specimen suffers quite severe back face damage. The damage at point F includes fibre breakage and delamination and can be seen as splitting of the back face of the specimen. At point E the back face deformation or bulging is 0.6 mm (i.e. h=0.6 mm) and at point F this increases to 1.9 mm. By comparing Figure 3.14 and Figure 3.15 it is clear that the damage mechanism in the specimen changes very quickly over a very small change in indenter

displacement. Back face splitting was also observed by Davies and Zhang [1995] as the final damage mechanism present in CFRP laminates.

The difference in indenter displacement between these two micro-graphs is only 0.5 mm (marked on Figure 3.14). The additional indenter displacement of 0.5 mm has a severe effect on the specimen. Figure 3.14 shows the specimen intact with the delaminations not yet at the boundary and no back face damage. After a further penetration of 0.5 mm (Figure 3.15) the back face has split open, the delaminations have reached the boundary and the load carrying capacity of the specimen has dropped significantly. The specimen has essentially failed.

The deformation zone, which is defined as the diameter of the bulged zone, d, also increases considerably during the load drop. The bulge height and diameter are represented in Figure 3.16 and it is clear how both have the biggest increase during the load drop (point E to F in Figure 3.16). What is not clear, however, is what influence the smaller load drop has on the damage.

The specimen in Figure 3.15 was also strain gauged and the strain gauge failed at a value of 2.5 %. The strain gauge failed at the small load drop and not the main load drop. This would suggest that the back face also failed at this point. The strain gauge is rated at 5 % which means it didn't fail due to overloading but due to the back face splitting. Since the strain gauge is bonded to the back face, when the back face splits the strain gauge also splits. Thus the back face probably splits at the small load drop which is just past point E in Figure 3.2.

3.3.7 Steady State

From point F onwards the delaminations do not grow. They reach a 'steady state' and level off. This is seen in Figure 3.17. It should be noted that the maximum value of the delamination

diameter is 25.6 mm which is also the diameter of the opening. In other words this 'steady state' is a boundary effect.

In Figure 3.15 there are also new delaminations which form near the crater left by the indenter. As the indenter penetrates further these delaminations grow. This can be seen by looking at Figure 3.15, Figure 3.18 and Figure 3.19. Before the load drop the material was pushed aside and the indenter penetrated by shearing and crushing the plies. This mechanism changes once the load drops from a crushing/shearing action to a ply rotation action. This is made possible since there is now a 'softened zone' ahead of the indenter. Once again this can be seen in Figure 3.15 and quite clearly in Figure 3.18 and Figure 3.19.

3.3.8 Springback

There is evidence of springback of the plies once the specimen is unloaded. The specimen corresponding to point H (Figure 3.19) for example was tested up to a 12 mm indenter displacement. The specimen is 6.15 mm thick, and deflection due to global bending was 1.4 mm. As a result 4.5 mm of the tip of the indenter was sticking out which is the equivalent of a 4 mm diameter cylindrical indenter. And clearly there is not a 4 mm hole left behind once the indenter is removed (Figure 3.19). The plies that were pushed aside by the indenter springback and close the hole left by the indenter.

3.4 Summary

A series of static penetration tests have been performed and the main damage mechanisms identified. There are 3 damage mechanisms present during the penetration. The first damage mechanism is matrix cracking and it is from these cracks that the delaminations emanate. The

whole process begins with penetration and bulging. The bulging continues during the penetration but when the matrix cracks reach a critical size, delamination becomes the dominant damage mechanism. The back face then fails, at which point the overall damage is quite severe. Understanding the type and sequence of damage in the manner demonstrated here is vital for development of physically meaningful analytical/numerical penetration models.

Table 3.1. Test matrix for the experiments.

Specimen #	Point	1st loading mm	2nd loading mm	3rd loading mm	4th loading mm	5th loading mm	6th loading mm
qs-sd-06c	H	2.22	4.07	6.03	8.02	10.02	12.04
qs-sd-07c	E	5.35					
qs-sd-08c	F	5.85					
qs-sd-09c	D	3.80					
qs-sd-10c	G	9.83					
qs-si-11c	A	0.61					
qs-si-12c	B	1.63					
qs-si-13c	C	2.60					

Table 3.2. Table showing delamination number and corresponding distance from the top surface. (See also Figure 3.12).

Delamination Number	Distance from Top Surface mm
I	2.69
II	3.92
III	4.61
IV	5.30

Table 3.3. Table of delamination diameter and delamination number.

Delamination Diameter

delam no point	I mm	II mm	III mm	IV mm	Inden Displ mm	Force N
A	0.00	0.00	0.00	0.00	0.61	2798
B	0.00	0.00	0.00	0.00	1.63	5358
C	11.83	11.51	10.01	11.61	2.60	6482
D	21.07	10.14	13.37	15.22	3.80	7719
E	23.98	19.99	21.52	22.30	5.35	8718
F	25.83	22.75	25.37	25.21	5.85	9330
G	25.06	19.84	22.91	24.60	9.83	9593
H	25.22	21.22	23.68	21.99	12.04	8231

Table 3.4. Table showing measurements taken from the specimens.

Point	Penetration Depth mm	Bulge Height mm	Bulge Diameter mm	Hole Diameter mm	Indenter Displacement mm	Force N
A	0.38	0.00	0.0	1.0	0.61	2798
B	1.00	0.15	6.0	1.7	1.63	5358
C	1.70	0.45	10.2	2.4	2.60	6482
D	2.40	0.60	13.0	3.1	3.80	7719
E	3.20	0.70	15.0	3.2	5.35	8718
F	4.05	1.85	18.7	3.8	5.85	9330
G	5.90	3.20	21.6	6.0	9.83	9593
H	8.20	3.30	25.4	6.6	12.04	8231
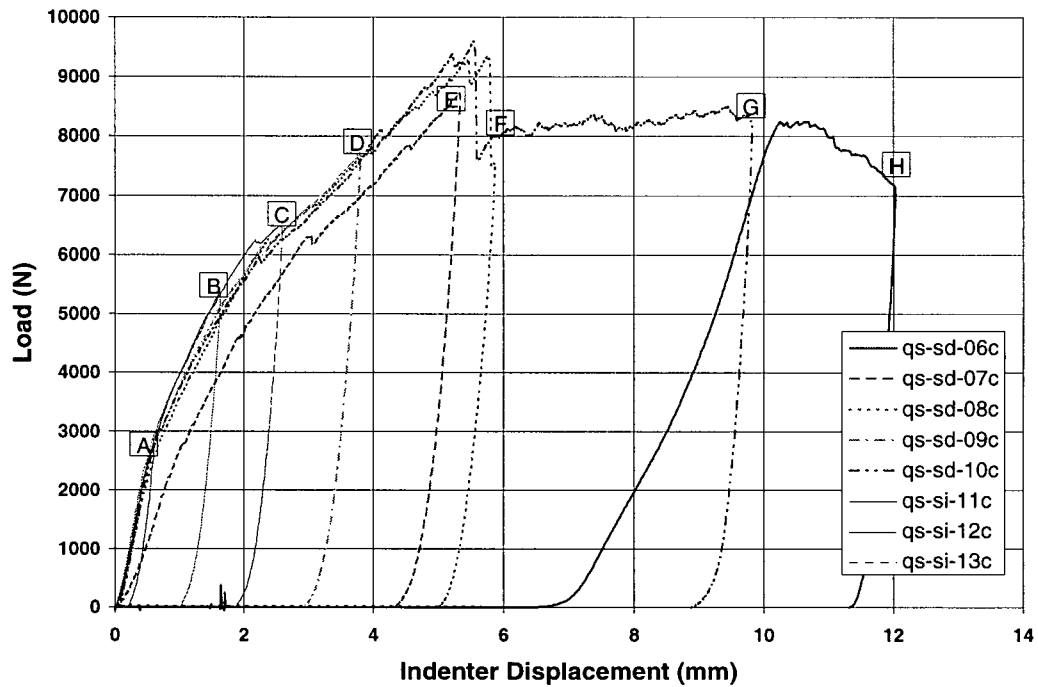
Figure 3.1. Load-displacement curves for all the static tests on CFRP laminates.
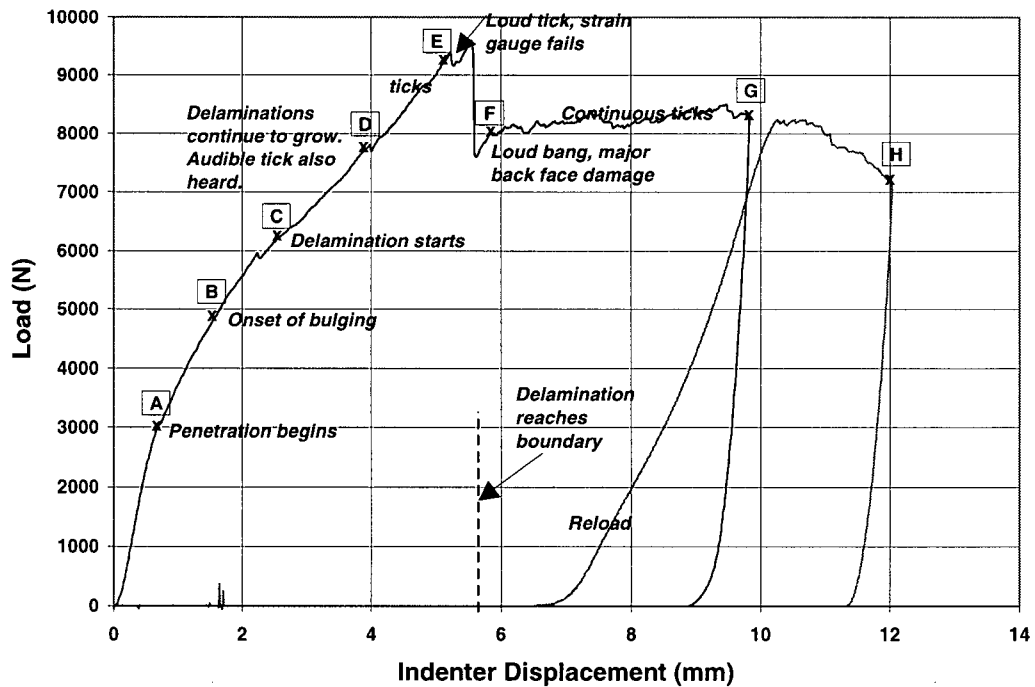
Figure 3.2. Load-displacement curve for specimens qs-sd-10c and qs-sd-06c with comments corresponding to the progression of damage.

Force	Indenter Displacement	Bulge Height	Bulge Diameter
N	mm	mm	mm
2798	0.61	0.00	0.00
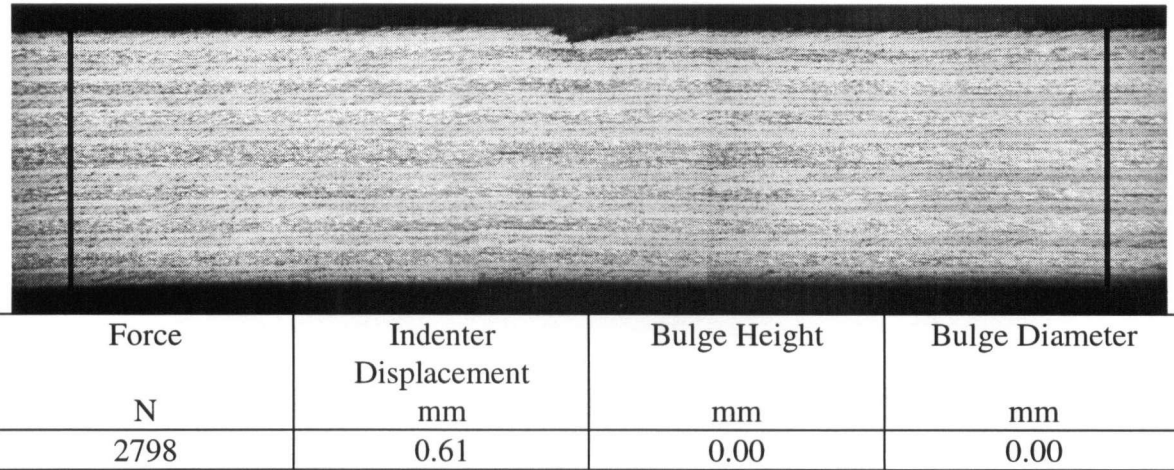
Figure 3.3. Micro-graph corresponding to point A.
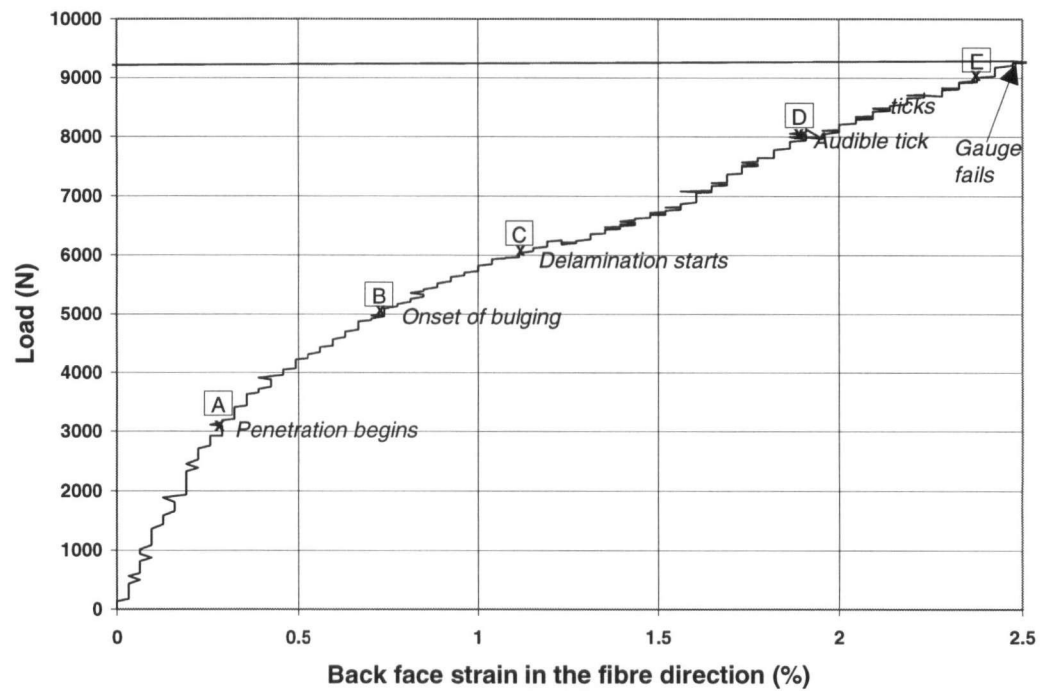
Figure 3.4. Load strain curve for specimen qs-sd-08c.
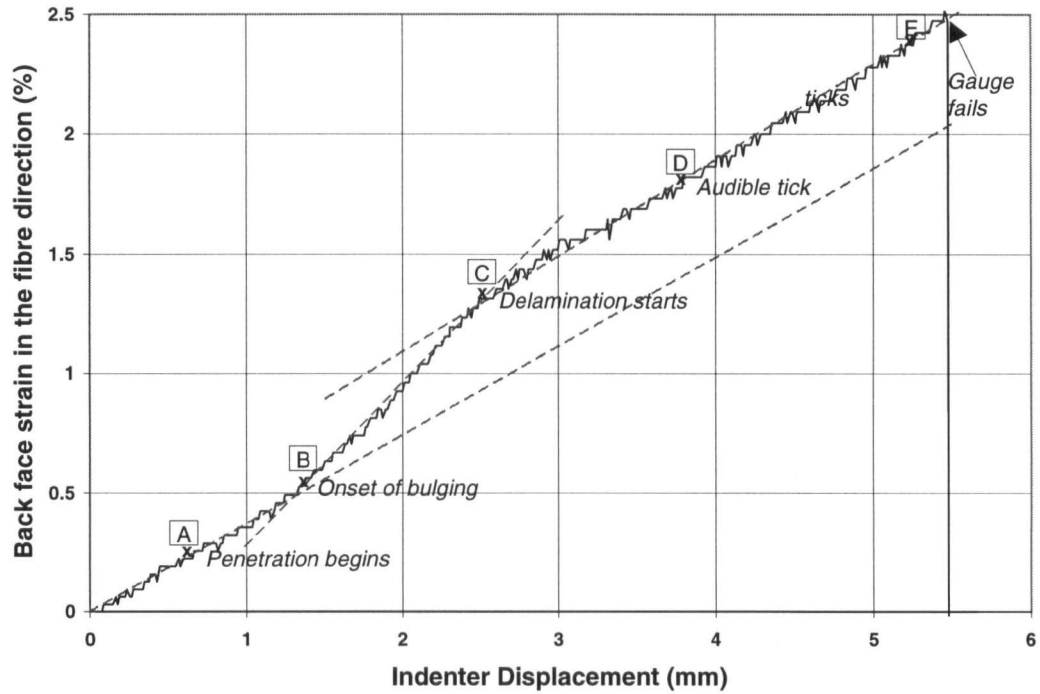
Figure 3.5. Curve for specimen qs-sd-08c showing the onset of bulging.
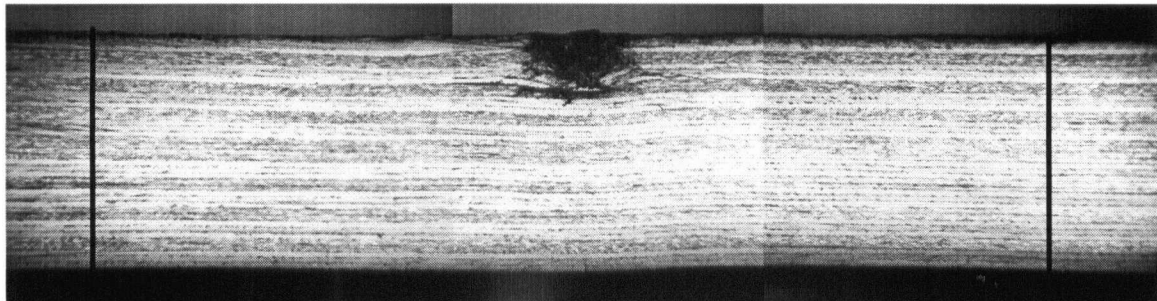
Force	Indenter Displacement	Bulge Height	Bulge Diameter
N	mm	mm	mm
5358	1.63	0.15	6.0

Figure 3.6. Micro-graph corresponding to point B.
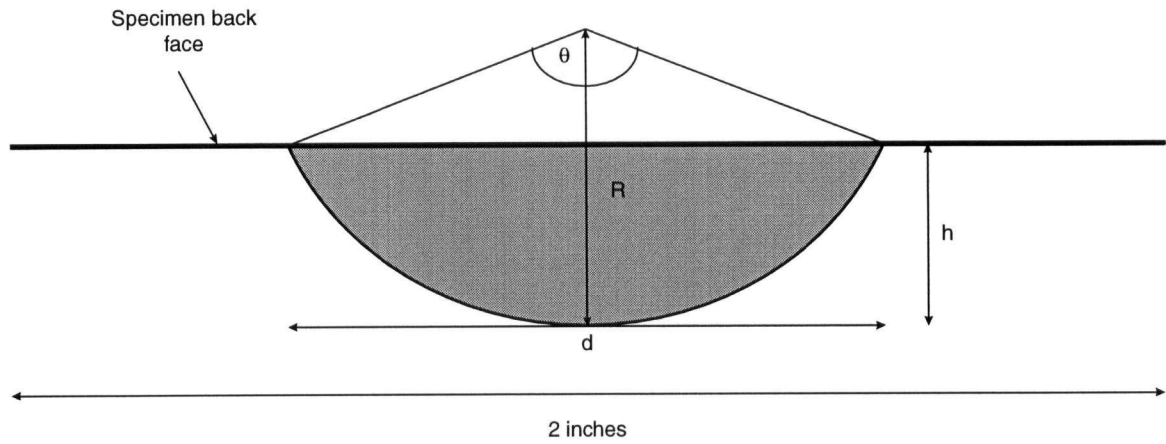
Figure 3.7. Schematic showing calculation of strain due to bulging.
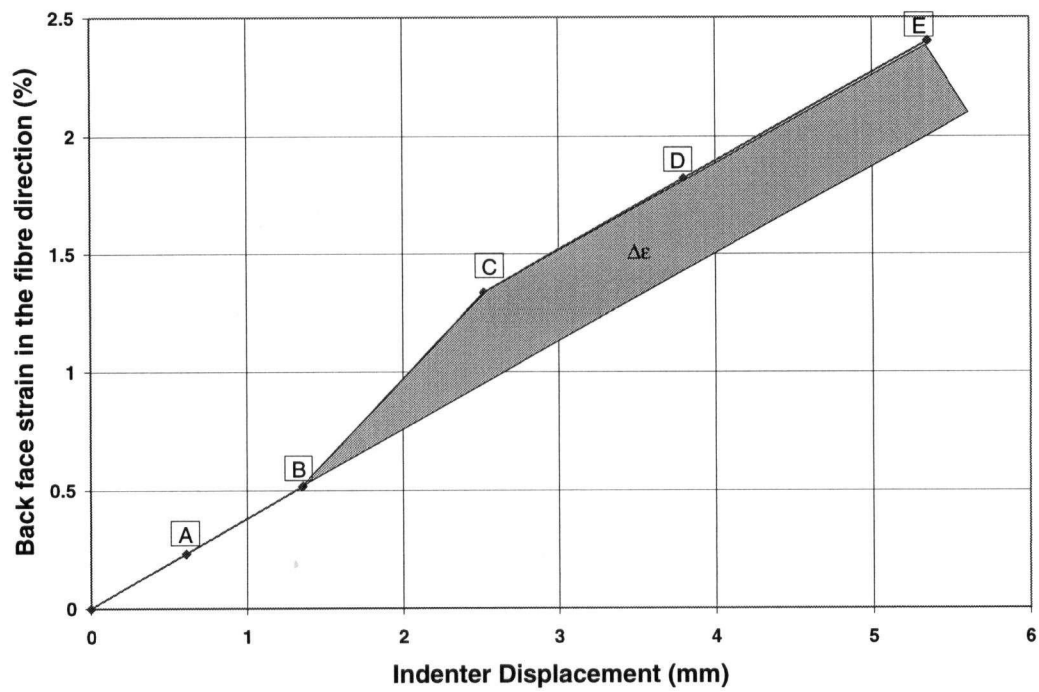
Figure 3.8. Idealised strain-displacement curve for specimen qs-sd-08c assuming bulging initiation at point B in Figure 3.2.
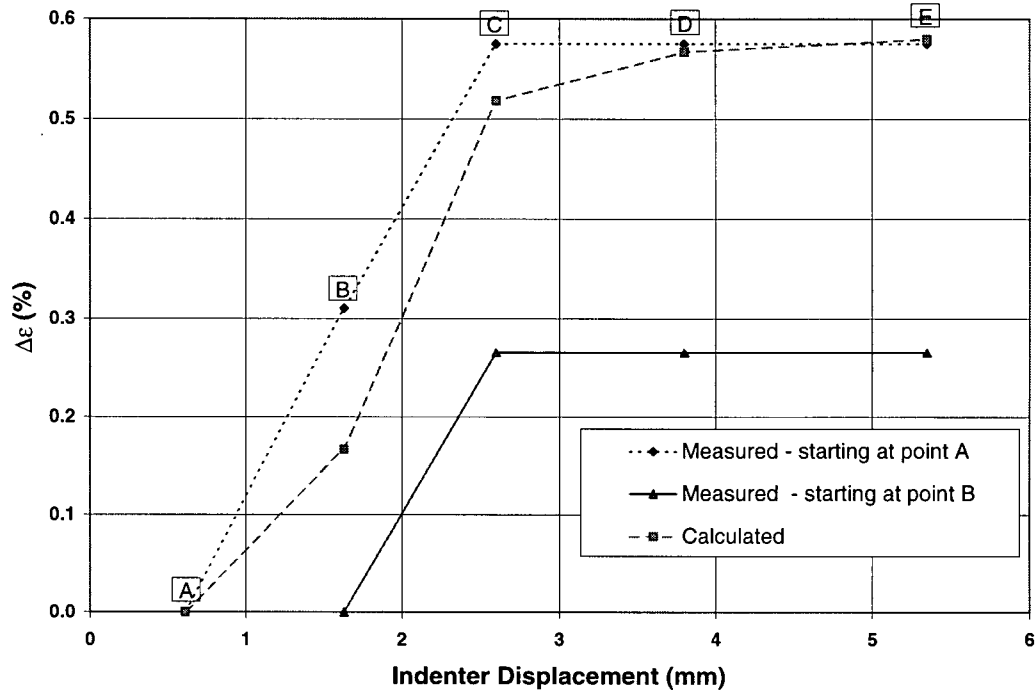
Figure 3.9. Comparison of measured change in strain ($\Delta\varepsilon$) to calculated $\Delta\varepsilon$ due to bulging. The dotted curve represents the measured strain assuming that bulging begins at point A and not point B.
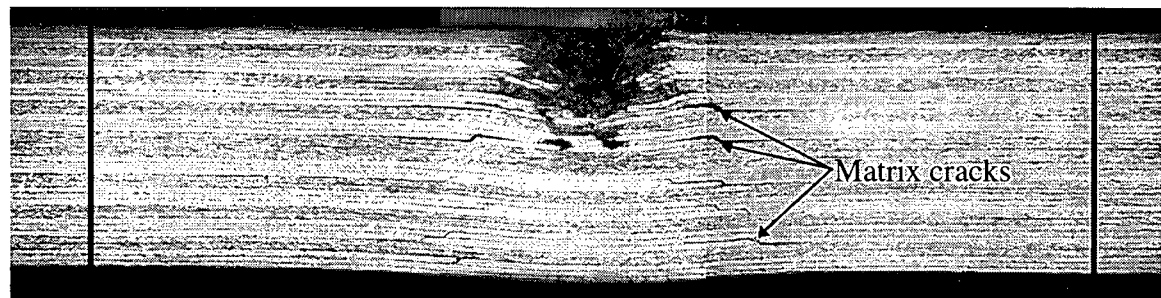
Force	Indenter Displacement	Bulge Height	Bulge Diameter
N	mm	mm	mm
6482	2.60	0.45	10.2

Figure 3.10. Micro-graph corresponding to point C. This micro-graph also shows matrix-cracking.

Impact Damage Growth Mechanism
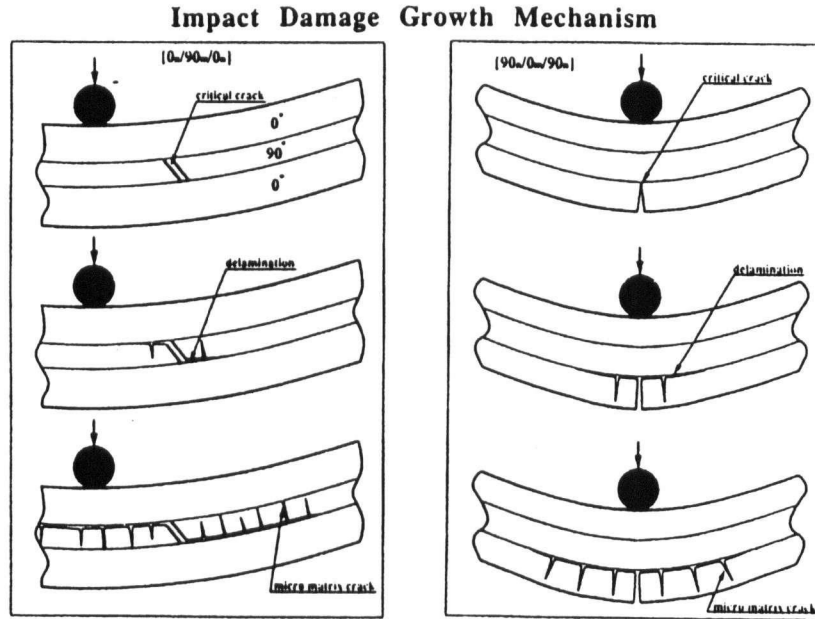
Figure 3.11. Schematic showing matrix cracks due to transverse shear (left) and matrix cracks due to bending stresses (right) (from Choi *et al.* [1991c]).
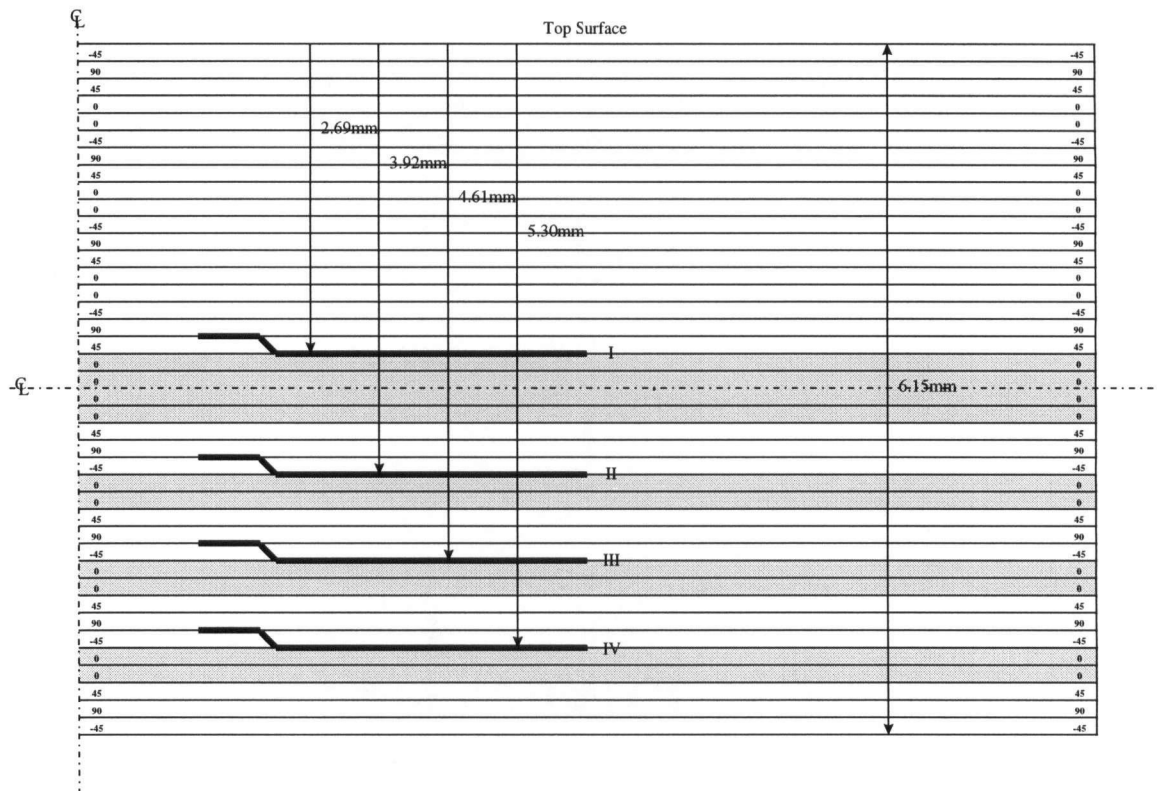
Figure 3.12. Schematic showing delamination number, delamination depth, delamination initiation and delamination growth (not to scale).
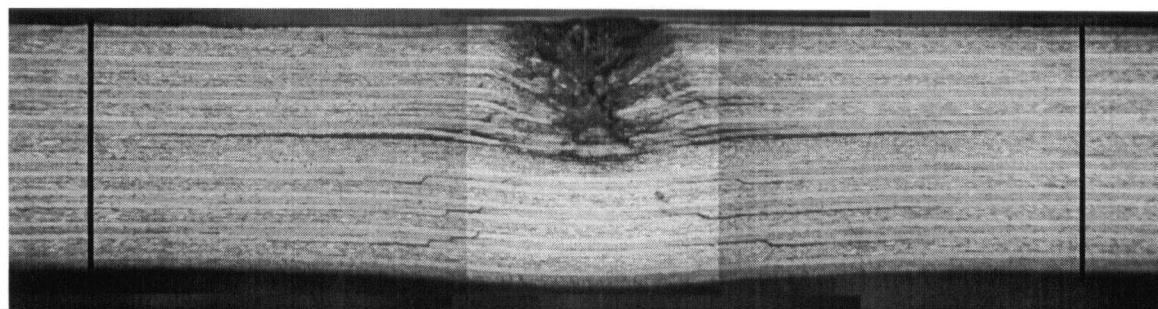
Force	Indenter Displacement	Bulge Height	Bulge Diameter
N	mm	mm	mm
7719	3.80	0.60	13.0

Figure 3.13. Micro-graph corresponding to point D.
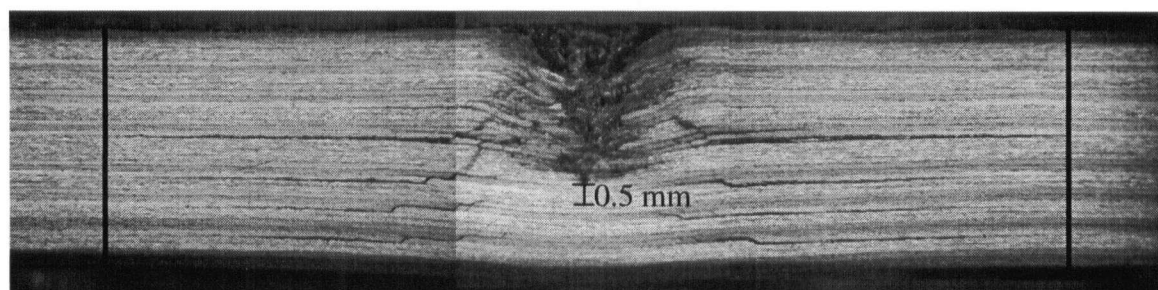
Force	Indenter Displacement	Bulge Height	Bulge Diameter
N	mm	mm	mm
8718	5.35	0.70	15.0

Figure 3.14. Micro-graph corresponding to point E.
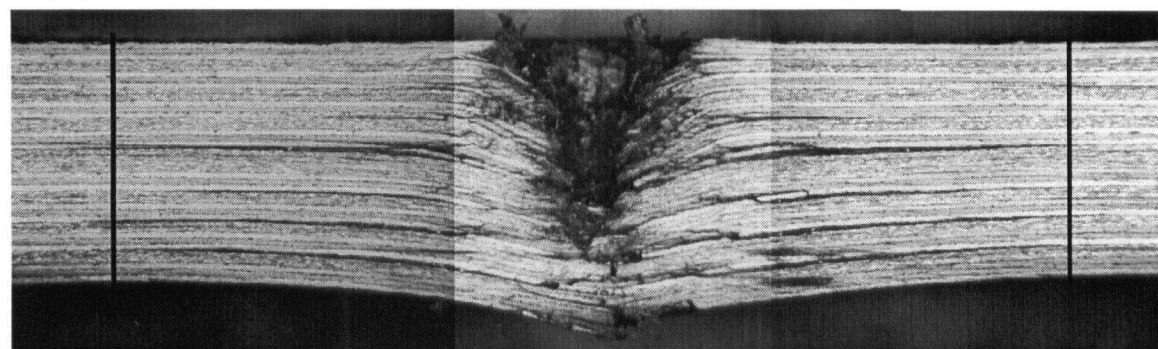
Force	Indenter Displacement	Bulge Height	Bulge Diameter
N	mm	mm	mm
9330	5.85	0.70	15.0

Figure 3.15. Micro-graph corresponding to point F.
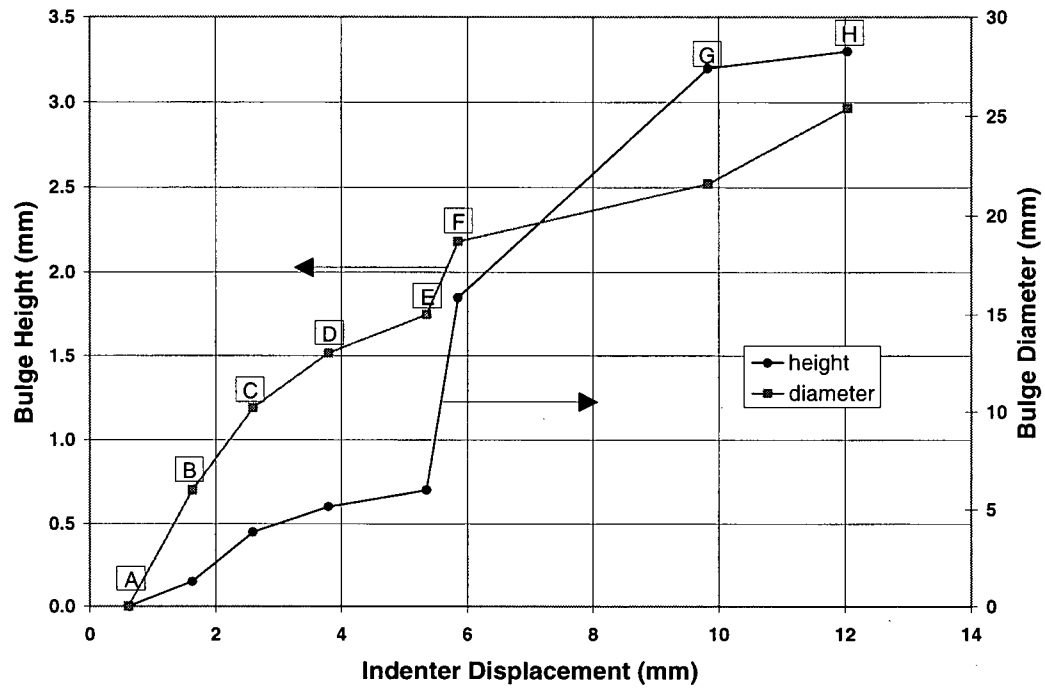
Figure 3.16. Curve of bulging and deformation zone.
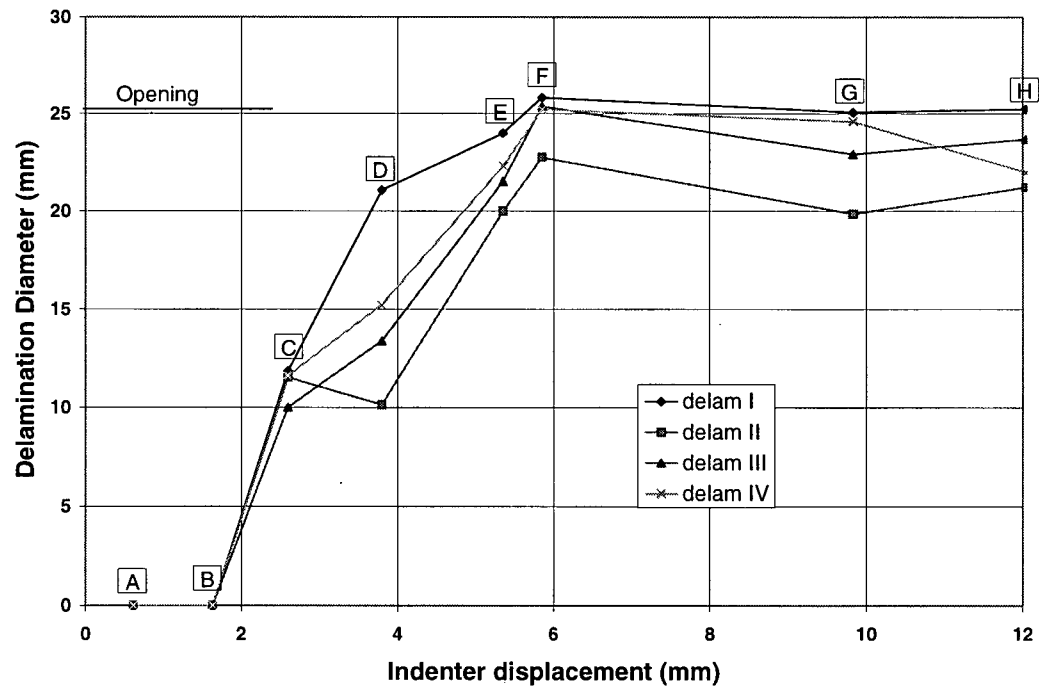
Figure 3.17. Curve showing delamination growth.
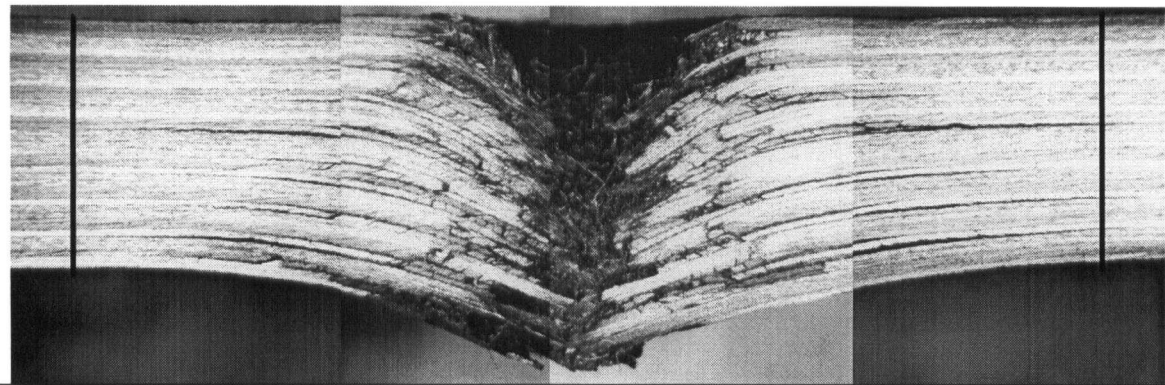
Force	Indenter Displacement	Bulge Height	Bulge Diameter
N	mm	mm	mm
9593	9.83	3.20	21.6

Figure 3.18. Micro-graph corresponding to point G.
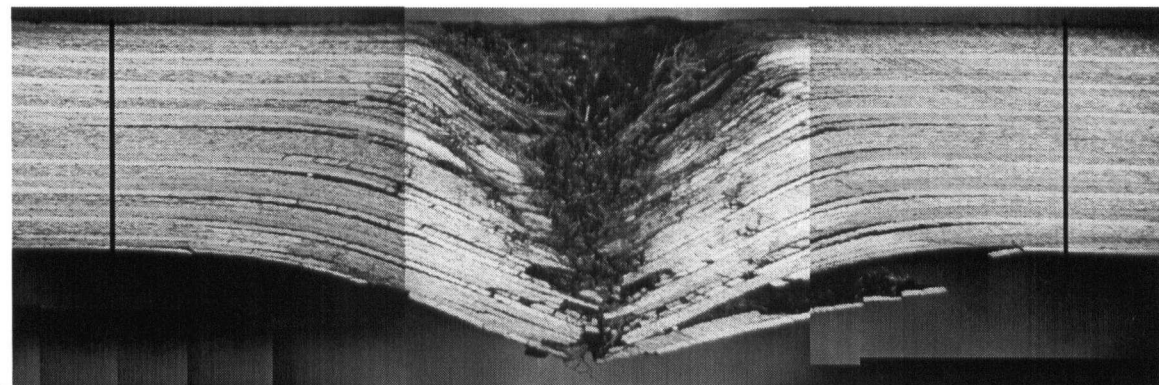
Force	Indenter Displacement	Bulge Height	Bulge Diameter
N	mm	mm	mm
8231	12.04	3.30	25.4

Figure 3.19. Micro-graph corresponding to point H.

Chapter Four

Static and Ballistic Penetration of GFRP Laminates

4.1 Background

The impact resistance of GFRP laminates has received considerable attention regarding damage mechanisms, failure modes and ballistic limits. The one area lacking in the literature, however, is the continuous measurement of the impact force during ballistic tests. Furthermore, no comparison has been made between static and ballistic tests which is perhaps due to the strain rate sensitivity of glass.

4.1.1 Strain Rate Sensitivity

Sun and Potti [1993] and Lee and Sun [1993b] made use of static tests to predict the ballistic response of CFRP laminates. Static tests were performed on carbon-epoxy (Hercules AS4-3501/6) specimens with 9 x 9 cm square geometry. Based on the static penetration tests a model was developed and applied to the ballistic tests. Good agreement was found except for residual velocities which tended to be over-predicted in the thicker laminates. They also found that the overall damage pattern was similar for the static and ballistic cases.

Other authors also made use of static tests to predict ballistic responses. All of these analyses, however, are for CFRP which, unlike GFRP, is a strain rate insensitive material. Harding and Welsh [1983], Staab and Gilat [1993] and Newill [1993] performed split Hopkinson-bar tensile tests on GFRP specimens. Harding found that increasing the strain rate increased the maximum stress before failure for GFRP specimens. Increasing the strain rate also had the effect of increasing the elastic modulus. Also, the energy absorbed in fracturing GFRP specimens increased dramatically with increased strain rate. All the authors concluded that GFRP is strain rate sensitive.

Delfosse [1994] performed dynamic compression tests on both CFRP and GFRP and found similar results to Harding. He found that for CFRP, there was only a slight increase in elastic modulus for increasing strain rates whereas GFRP had a definite increase in elastic modulus. From this he concluded that CFRP is strain rate insensitive whereas GFRP is strain rate sensitive.

Jenq *et al.* [1994] performed static penetration tests on plain woven glass reinforced epoxy laminates with hemispherical indenters. These tests were done in order to characterise the progressive damage mechanisms which were then incorporated into a model. This model was then used to predict the ballistic response of the laminate. The impact tests were carried out using a gas gun. They found that while the major damage pattern in the impact and static tests were similar, the area of the rhombus-shaped delamination was about 9 times greater for the impacted specimens. Comparing the predicted and actual ballistic limits for the specimens further gave an error of 24 % which they attributed to the strain rate sensitivity of the glass. They found that by using a dynamic elastic modulus of twice the static elastic modulus good agreement could be obtained between the predicted and actual ballistic limits.

4.1.2 Force-displacement

Bless *et al.* [1990] studied the penetration of S-2 glass reinforced phenolic by conical (apex ratio of 3), hemispherical and blunt projectiles. The specimens were 150x150x12.70 mm with 25 plies. The projectiles were fired from a 0.30 calibre 0.74 m long rifle barrel. A streak camera was used to measure the projectile displacement. The streak record gave a continuous one dimensional picture of the penetration process. To enable the projectile to be tracked during the penetration, tails were added to the projectiles. The only disadvantage with the streak record is that the duration of the light source is 80 µs. The post test analysis of the streak record was also quite involved and the one thing lacking from this study was the knowledge of the projectile force during penetration.

Espinosa *et al.* [1996] studied the penetration of S-2 glass reinforced polyester by projectiles with a cone angle of 30°. They performed both direct penetration and reverse penetration experiments on 25.4 mm (1″) thick specimens. The reverse penetration experiments were performed by firing the target specimen at the projectile. A measurement system was developed that was capable of measuring both projectile velocity and back face motion of the specimen. The system was based on laser interferometry and has a time resolution in nanoseconds. It provided the continuous measurement of the projectile velocity during the impact but required quite extensive calculations to obtain the velocity from the raw data. As with Bless, no force-displacement curves for the impact were presented.

Wu *et al.* [1994] studied the impact of thin aluminium plates by hemispherical projectiles. The projectile velocity was measured using laser-Doppler anemometry. This system is very accurate

but the drawback is the complexity of both the system and the data reduction. The data reduction includes filtering the data and linear interpolation to get the velocity data. Once the velocity was obtained, a polynomial was used to best fit the data. By differentiating the polynomial the force was obtained. The drawback with curve fitting, however, is that the original velocity data is lost and sometimes this can lead to trends being missed. Wu *et al.* did, however, present force-displacement curves for the impact event.

A more direct measurement of the projectile force during impact was presented by Delfosse *et al.* [1993]. This study makes use of an instrumented projectile to measure the force during an impact event. This method provides the force directly and the only calculation needed is a Fourier transform to the frequency domain. This is necessary in order to remove vibrations due to the natural frequency of the projectile. This system is limited to velocities of about 50 m/s. At higher velocities the wire attaching the projectile to the oscilloscope breaks more frequently, resulting in a loss of signal.

4.2 Test Matrix

A total of 6 static deflection, 2 static indentation and 44 ballistic tests were completed during the course of this study. The test matrix has three different specimen thicknesses and two different cone angles as described in sections 2.2 and 2.3. Table 4.1 shows the test matrix for both the ballistic and static tests performed on GFRP laminates.

4.3 Static Deflection Tests

The results from the static deflection tests are shown in Figure 4.1 and Figure 4.2. These figures show the load-displacement curves for a 37° indenter (Figure 4.1) and a 120° indenter (Figure 4.2) penetrating specimens with thicknesses of 6.35 mm (0.25″), 12.70 mm (0.50″) and 19.05 mm (0.75″). The backing plate hole geometry is 76.2 mm (3″) x 127 mm (5″).

The specimens used in the static deflection tests were tested up to the point at which perforation occurred. This was done so that a comparison could be made with the ballistic tests in section 4.4. The frictional force between the 37° indenter and a 12.70 mm (0.50″) specimen was found to be 4720 N. This was established by testing a 12.70 mm (0.50″) specimen until the load remained constant (see Figure 4.1). This value is useful in determining the energy absorbed due to friction. Using this value and assuming the indenter is infinitely long the frictional force between the 6.35 mm (0.25″) and 19.05 mm (0.75″) thick specimens can be assumed to vary linearly. The values for all three thicknesses are shown in Table 4.2.

4.3.1 37° indenter

Figure 4.1 shows the load-displacement curves for a 37° indenter penetrating all 3 thicknesses. There are points of interest on each of the load-displacement curves and these are labelled A through J in Figure 4.1. Point A is common to all 3 thicknesses and is the start of penetration. In section 3.3.2 it was shown that the change of slope at this point is due to penetration.

Audible 'ticks' are heard for the first time at points B, E and H in Figure 4.1. These 'ticks' are the start of front face matrix cracking. The matrix cracks usually occur at the intersection of two

rovings as shown in Figure 4.3. These matrix cracks usually occur along the width and length of the specimen and are due to the compression of the front face resulting from bending. It was also found that the 6.35 mm (0.25″) thick specimens had more matrix cracking than the 19.05 mm (0.75″) thick specimen. The matrix cracks extended further towards the boundary. The reason for this is that the 6.35 mm (0.25″) thick specimens have a lower bending stiffness than the 19.05 mm (0.75″) thick specimens. Therefore the 6.35 mm (0.25″) thick specimen can bend more than the 19.05 mm (0.75″) thick specimen resulting in more matrix cracking.

As the test progresses the matrix cracks continue to grow and the 'ticks' can be heard periodically during the test. Points C, F and I in Figure 4.1 correspond to the peak load in the 6.35 mm (0.25″), 12.70 mm (0.50″) and 19.05 mm (0.75″) thick specimens respectively. After the peak load, the specimen is softened due to damage in the specimen and the resistance to penetration is reduced. This causes the load to decrease with increasing indenter displacement until the indenter perforates at points D, G and J in Figure 4.1. The micro-graphs corresponding to points D, G and J are shown in Figure 4.4 through Figure 4.6 respectively. Clearly there is no major damage other than the front face damage shown previously in Figure 4.3. The only other type of visible damage is 'fibre breakage'. This refers to the fibres that are cut as the indenter penetrates and not the traditional fibre breakage due to bending stresses.

Front face matrix cracking and 'fibre breakage' are the only visible damage mechanisms for specimens penetrated by 37° indenters. For all three thicknesses the load increases to the peak load, the specimen softens due to damage, and the resistance to penetration decreases with a corresponding drop in the load.

4.3.2 120° indenter

The load-displacement curves for the 120° indenter are shown in Figure 4.2 with points A through L labelled. The first observation is that penetration for the 12.70 mm (0.50″) and 19.05 mm (0.75″) thick specimens occurs immediately. The common point for penetration is the origin of the curve since there is no bluntness on the 120° indenter. In other words, penetration of the 12.70 mm (0.50″) and 19.05 mm (0.75″) thick specimens begins as soon as the load is applied. The curves also have a different shape from the 37° indenters.

Points A, D and I in Figure 4.2 are once again the first time 'ticks' are heard indicating the onset of front face matrix cracks. From A to B in Figure 4.2 the load increases and then from B onwards remains constant. The indenter never actually penetrates the 6.35 mm (0.25″) specimen. Figure 4.7 shows the top and side view of a 6.35 mm (0.25″) thick specimen and clearly the penetrater has not penetrated. The test was stopped at C in Figure 4.2 and the micro-graph of this point is shown in Figure 4.8. This micro-graph once again shows quite clearly that there is no penetration. The indenter simply pushes the 6.35 mm (0.25″) thick specimen through the hole in the backing plate causing severe damage (Figure 4.7).

The 12.70 mm (0.50″) thick specimen reaches the peak load and at E in Figure 4.2 there are louder ticks than before. Shortly after these ticks, at F, a 'tearing' noise is heard. This is the start of a delamination that literally separates a sub-laminate from the specimen. The 'tearing' starts at F and continues to G. From G to H there is once again the plateau seen in the 6.35 mm (0.25″) thick specimens. The micro-graph of point H is presented in Figure 4.9 and shows the sub-

laminate and the delamination which occurs at a depth of 4.33 mm from the front face (8.37 mm from the back face).

The 19.05 mm (0.75″) thick specimen exhibits similar trends to the 12.70 mm (0.50″) thick specimen. The peak load is reached and shortly after, at J in Figure 4.2, the same 'tearing' noise starts. This 'tearing' is once again a delamination that separates a sub-laminate from the specimen. The 'tearing' continues until K. From K to L there is once again a plateau. The micro-graph of point L is shown in Figure 4.10. The delamination occurs at a depth of 6.35 mm from the front face (12.70 mm from the back face).

There are two dominant parameters which emerge from the results of the static deflection tests. The first is cone angle and the second is thickness. Changing the indenter cone angle from 37° to 120° causes the delamination to occur. But, this delamination only occurs when the thickness is large enough to allow penetration.

The bending stiffness, or thickness, of the 6.35 mm (0.25″) thick specimen was not enough to allow penetration. It should be noted that the bending stiffness is a function of the boundary condition. We can see that if the hole size were to increase, the corresponding thickness needed for penetration would also increase.

As the thickness of the specimens is increased from 6.35 mm (0.25″) to 12.70 mm (0.50″) the corresponding bending stiffness increases. The specimen is now stiff enough to allow penetration to dominate over bending. The indenter penetrates until the bending stiffness of the remaining sub-laminate is once again low enough that penetration is not possible and bending

starts. It is at this point that the 'tearing' sound at F and J in Figure 4.2 begins. The 'tearing' is thus the onset of delamination as the sub-laminate separates from the specimen.

Thus there is a critical thickness which determines whether or not penetration will occur. This critical thickness is at least the thickness of the 6.35 mm (0.25″) thick specimen, or 6.35 mm. Therefore the sub-laminate thickness of the 12.70 mm (0.50″) and 19.05 mm (0.75″) thick specimens should be of that order. The sub-laminate thickness for the 12.70 mm (0.50″) and 19.05 mm (0.75″) thick specimens are 4.5 mm and 9.4 mm respectively. If, however, the sub-laminate thickness for the 19.05 mm (0.75″) thick specimen is taken from the penetration depth, then the sub-laminate thickness would be 6.0 mm. Both of these values are close to the value of 6.35 mm indicating that the critical thickness required for penetration on a 76.2 x 127.0 mm (3″x5″) opening is approximately 6 mm.

4.4 Static Indentation Tests

The results from the static indentation tests are shown in Figure 4.11. This figure shows the load-displacement curves for a 37° and 120° indenter penetrating 19.05 mm (0.75″) thick specimens. The backing plate is a rigid steel plate that inhibits plate bending and thus the response is purely due to the local indentation.

For both indenter angles the indenter shaft started to bend and the test had to be stopped. During the tests there were no sudden load drops and no audible 'ticks' indicating front face matrix cracking. The load merely increased until the indenter yielded. If the indenter didn't bend it would be expected that the load-displacement curves would continue to increase at a constant

rate. The load-displacement curve also shows that the loading rate for the 120° indenter is higher than the 37° indenter.

This increase in loading rate can be explained by looking at Figure 4.12 which shows the micrographs for the static indentation tests. The 37° indenter penetrates twice as much as the 120° indenter for the same force. The reason for this is that the 37° indenter is capable of pushing the plies laterally as it penetrates. The fibre buckling which results, is clearly visible in the micrograph. The 120° indenter, however, is not as efficient at pushing the plies laterally and, as a result, debris builds up ahead of the indenter. The 120° indenter therefore has to crush the plies thereby generating much higher forces over a small indenter displacement when compared to the 37° indenter.

4.5 Ballistic Tests

The displacement-time, velocity-time, force-time, energy-displacement and force-displacement curves for each of the ballistic tests are shown in Figure 4.13 through Figure 4.18. All the force-displacement curves show the comparison between the ballistic and static tests with the projectile striking velocity, v_s, and the projectile residual velocity, v_r, labelled. Where possible two ballistic tests were included to compare a projectile which came to a complete stop in the specimen and one which perforated the specimen.

The curves for the ballistic tests show very good agreement with the static deflection curves. The initial portion of the impact follows the static indentation of the material. During this part of the impact there is no plate bending. The flexural waves are travelling to the boundary of the plate and back. When a significant number of these flexural waves pass backward and forth across the

plate, plate bending is possible and at this point the impact deviates from the static indentation response.

The static and ballistic curves for a 37° projectile agree well in matching the peak load and general shape of the curve. For the 120° projectile, however, the static curves tend to under predict the ballistic response in force and energy.

The effects of the test parameters will be discussed next. These parameters are impact velocity, specimen thickness and cone angle.

4.5.1 Effect of Impact Velocity

Figure 4.19 shows the effect of the impact velocity on the response of the specimen. The event duration, t_{event}, is marked on the curve and is defined as the time taken to reach the maximum projectile displacement. For projectiles which stop in the specimen, there is enough time for the plate to bend and hence there are oscillations after the load has peaked. These oscillations are most likely due to the flexural waves travelling through the plate. As the velocity is increased, the penetration becomes more localised and the time available for bending is reduced. This means that the flexural waves have less time to travel through the plate. As the penetration becomes more localised, there is also less global bending with the result that the oscillations seen at the lower velocity die out.

This can be seen by looking at Figure 4.20. This figure shows the event duration plotted as a function of the impact velocity. The dashed line in Figure 4.20 represents the time taken to travel the width of the laser sheet. This is essentially the 'event duration' with no target. The dashed line thus provides a lower bound for the event duration. Figure 4.20 does show that as the impact

velocity increases, the event duration decreases, which means that there is less time available for the specimen to respond to the impact. It is also clear from this plot that as the impact velocity is increased the event duration approaches the lower bound indicating that during the initial portion of the impact the projectile does not slow down appreciably.

4.5.2 Effect of Thickness

Figure 4.21 shows the effect of increasing the specimen thickness for specimens impacted by projectiles with a cone angle of 37°. This figure actually contains both changes in impact velocity and thickness. It has just been shown, however, that the impact velocity does not affect the general character of the response curve. Therefore Figure 4.21 reflects purely the effect of changing the specimen thickness. The increase in thickness causes the peak projectile force to increase. This is also evident when the specimen is impacted by a projectile with a cone angle of 120°, as shown in Figure 4.22.

The relationship between specimen thickness and peak projectile force is shown in Figure 4.23. The dotted lines are the results of the static deflection tests. There is a definite increasing relationship between thickness and peak projectile force. The agreement between the ballistic and static tests is good for the 37° cone angle and not as good for the 120° cone angle.

4.5.3 Effect of Cone Angle

Figure 4.24 shows the comparison between a 37° projectile and a 120° projectile impacting a 12.70 mm (0.50″) thick specimen. The first observation is that the peak force is higher for a 120° projectile and occurs at a lower projectile displacement than the 37° projectile. The second observation is that the shape of the load-displacement curve is different for the two projectile

angles. The load-displacement curve for the 120° projectile rises to the peak load and then decreases. The load-displacement curve for the 37° projectile, however, has a *dip* at about 4 mm before it reaches the peak load at 11 mm.

Figure 4.25 shows the relationship between the cone angle and peak projectile force for both the static deflection tests (dotted lines) and ballistic tests (solid lines). This shows that as the cone angle is increased the peak projectile force increases. The agreement between the static and ballistic tests is good except for the 19.05 mm (0.75") thick specimens. As mentioned in section 4.5.1 increasing the thickness also has the effect of increasing the peak projectile force. Therefore it could be stated that changing the cone angle has the effect of stiffening the specimen. In other words the apparent stiffness of the specimen increases as the cone angle is changed from 37° to 120°.

A further indication that the change of cone angle changes the apparent stiffness of the specimen comes from looking at the initial slope of the load-displacement curve in Figure 4.24. Clearly as the projectile cone angle increases from 37° to 120° so too does the slope of the initial portion of the load-displacement curve indicating that the apparent stiffness of the specimen has increased.

4.5.4 Plate Vibration

Some of the curves show what appears to be plate vibrations during the test. These vibrations occur while the projectile is still impacting the specimen and hence are not free vibrations of the specimen. Figure 4.26, however, shows an impact test where the projectile has come to a complete stop and the plate is in free vibration. The frequency of the oscillation from A to B in Figure 4.26 is 8.5 kHz.

The calculation of the free vibration of a rectangular plate is presented in Appendix C. From these calculations the frequency of free vibration is 7.2 kHz which corresponds to the second mode of vibration along the length of the specimen, and the first mode of vibration along the width of the specimen.

4.6 Ballistic Damage Mechanisms

Figure 4.27a shows the micro-graph for a 19.05 mm (0.75″) thick specimen impacted by a projectile with a 37° cone angle. The impact energy for this test was 154 J. The figure on the right is the result of a dye penetrant test performed on the same specimen. The dye penetrant test shows that there are *micro-delaminations* present as a result of the impact. These micro-delaminations are the separation of the plies but are not visible to the naked eye. The micro-delaminations form in a cone shape with the base of the cone at the impact side of the specimen. These micro-delaminations are possibly a result of the top few plies lifting up.

Figure 4.27b shows the micro-graph for an impact energy of 284 J. The micro-delaminations that started have grown and new micro-delaminations are also starting. These micro-delaminations are due to bending stresses in the specimen and also form a cone. The base of this cone, however, is at the back face of the specimen.

Figure 4.27c shows the micro-graph for a specimen tested at the ballistic limit of the material (365 J). The micro-delaminations continue to grow as the energy is increased.

Figure 4.27d and Figure 4.27e show the micro-graphs for impact energies above the ballistic limit. On both these micro-graphs the double cone is quite visible. The micro-delaminations have also grown further towards the boundary.

The damage mechanisms for the ballistic tests appear to be similar to the static tests. The only visible difference is the fibres around the penetration cavity. Figure 4.6 and Figure 4.27c represent the static and ballistic micro-graphs for perforation respectively. The energies are 407 J (static) and 365 J (ballistic) respectively. There is fibre buckling in Figure 4.27c that is not seen in Figure 4.6. The fibre buckling is most likely an effect of the loading rate. In the static test the fibres have time to deform and bend in the direction of the indenter. In the ballistic test, however, there is no time for the fibres to deform and the projectile pushes the fibres laterally. Thus the fibres have no option but to buckle laterally.

Fibre buckling has been identified by some authors as one of the failure modes in S-2 glass reinforced laminates. Kandasamy *et al.* [1994] and Bless *et al.* [1990] performed ballistic experiments on 12.70 mm thick S̄-2 Glass reinforced phenolic with blunt, hemispherical and conical projectiles. They found that failure modes depend on the shape of the projectile as well as the impact velocity. For conical and hemispherical projectiles they showed that the projectiles shear the fibres at the nose tip. These sheared fibres are then pushed laterally and buckle around the projectile. The failed fibres were then displaced above the target impact surface causing the top few plies to lift up.

The double cone of micro-delamination was also identified by Bless *et al.* [1990]. They studied the impact of S-2 Glass reinforced phenolic by hemispherical, conical and blunt projectiles. For impacts near the ballistic limit they found that there is a small delaminated region near the impact

site and a much larger delaminated region in the rear of the specimen. The conical and hemispherical projectiles cause upward delamination of the first few plies. This upward delamination is what causes the smaller cone mentioned previously.

Changing the projectile cone angle from 37° to 120° once again has an effect on the damage mechanisms. The micro-graphs for a 12.70 mm (0.50″) specimen impacted by a 120° projectile are shown in Figure 4.28. The figure on the right is the result of a digitised image showing the micro-delaminations.

The first observation is that there is a delamination present which is not seen in the 37° projectile. Figure 4.28a shows the micro-graph for an impact energy of 267 J. There is no delamination present in this specimen. The only damage is in the form of micro-delaminations around the penetration cavity. The micro-delaminations do not form in the double cone but result from bending stresses. This is due to the fact that the top plies do not lift up causing micro-delamination. The sub-laminate thickness at this impact energy is 6.10 mm.

The second observation is that the penetration cavity for 120° projectiles is different than that caused by 37° projectiles. Figure 4.27c and Figure 4.28a show the comparison between the penetration cavities for specimens impacted by 37° and 120° projectiles respectively. Quite clearly the 120° projectile causes a crater. This crater was also identified by Kandasamy *et al.* [1994] and Bless *et al.* [1990]. Figure 4.29 shows the difference in penetration cavities for hemispherical (or conical) and blunt nose projectiles.

Figure 4.28b shows the micrograph for an impact energy of 327 J. This is the first time the delamination is present. It occurs at a depth of 5.45 mm with a sub-laminate thickness of

5.75 mm. (The sub-laminate thickness is measured from the penetration depth). Once again there is a critical thickness which determines whether or not there will be delamination. This critical thickness appears to be between 6.10 mm and 5.75 mm.

As the impact energy is increased the delamination depth increases and the sub-laminate thickness decreases. Figure 4.28c shows the micro-graph for an impact energy of 486 J. The sub-laminate thickness has been reduced from 5.75 mm to 4.35 mm. Comparing Figure 4.9 and Figure 4.28c we see a very good agreement in the delamination depth and sub-laminate thickness. The energy absorbed in the static test was assumed to be the energy up to the point at which the tearing stopped (G in Figure 4.2). This gives a value of 473 J which compares well with the ballistic test of 486 J. The sub-laminate thickness for the static and ballistic tests are 4.45 mm and 4.35 mm respectively. So for the same amount of absorbed energy the damage mechanism is identical. What this shows is that the static deflection tests using a 120° indenter represent one case in the ballistic tests.

Further increasing the impact energy (Figure 4.28d and Figure 4.28e) results in the sub-laminate thickness getting even smaller. It is also interesting to note that the delamination occurs at the point where the projectile stops. Chou *et al.* [1995] studied the impact of S-2 Glass reinforced polyester by fragment simulating projectiles (FSP's) and also found that there was a large delamination at the location where the projectile stopped.

This suggests that the delamination is dependent on impact energy. There is a threshold impact energy which determines whether or not the specimen will delaminate. Figure 4.28a shows the specimen with no delamination. As the impact energy is increased the projectile is able to penetrate further until the critical thickness is passed and the first delamination occurs (Figure

4.28b). Increasing the impact energy further (Figure 4.28c) results in the delamination depth increasing. At higher impact energies the projectile has more energy to penetrate further. At some stage, however, the force needed to penetrate the next ply will be insufficient. At this point the remaining energy of the projectile will go into growing the delamination and the projectile comes to a stop at the point the delamination is initiated. Thus as the energy is further increased it would be expected that the delamination would vanish altogether. Figure 4.30 shows the relationship between delamination depth, sub-laminate thickness and energy. Clearly as the energy increases the delamination depth increases and the sub-laminate thickness decreases.

The ballistic tests on 6.35 mm (0.25″) thick specimens either perforate or rebound. As with the static deflection tests, this suggests that there is a critical thickness below which penetration does not occur.

4.7 Ballistic Limit

The ballistic limit of a material (v_{50}) is defined as the velocity at which there is a 50 % chance of perforation. A more meaningful way to look at this parameter is by considering an E_{50}, rather then a v_{50}. The reason for this is that different mass projectiles will give a different v_{50}, for the same amount of energy. Therefore it becomes difficult to compare tests where the mass of the projectile changes. To compare with static tests, it is also more meaningful to look at perforation energies. So for comparison, it is more meaningful to use E_{50} instead of v_{50}.

During the course of this thesis, static deflection and ballistic tests were performed to establish the perforation energies. The ballistic tests made use of projectiles with masses of 4.25 g and 13.2 g. Thus, there are 3 independent methods for calculating the perforation energies. It is

generally agreed that v_{50} varies linearly with areal density. Bless *et al.* [1989] investigated the effect the matrix, fibre content and fibre-resin compatibility had on S-2 glass composites. He used fragment simulating projectiles (FSP's) to impact the specimens and found that the ballistic limit varied linearly with areal density, as shown in Figure 4.31. Bless *et al.* [1985] also looked at the ballistic impact of thick S-2 glass composites and once again found that the ballistic limit varied linearly with areal density. Szymczak [1994] compared the ballistic properties of a variety of materials and reached the same conclusion.

The literature clearly uses v_{50} instead of E_{50}. This is most likely because of convenience and the fact that during impact projectiles may deform. In deforming, the projectiles would absorb energy and thus the E_{50} measured might be higher than it actually is.

Figure 4.32 shows the results of the ballistic limits for both the 37° and 120° projectiles. As expected, the lighter 37° projectiles have higher ballistic limits. The 120° projectiles also have a higher ballistic limit than the 37° projectiles. Figure 4.33 shows the plot of E_{50} (see Table 4.3) against areal density for 37° projectiles and indenters. It would be expected that the energies are the same regardless of the mass of the projectile, assuming there are no strain rate effects. This plot, however, shows small discrepancies between the two projectile masses and the static deflection tests. It should be noted that these curves include energy absorbed due to friction between the material and indenter/projectile. Thus, removing this energy should give better agreement between the tests.

Figure 4.34 shows the same results but with the energy absorbed due to friction removed. Using the friction force from section 4.3, and knowing how much further the 13.2 g projectiles

penetrated than the 4.25 g projectiles, it is possible to calculate the energy absorbed due to friction from

$$E_{absorbed} = F_{friction} * d \tag{4.1}$$

where $E_{friction}$ is the friction force and d is the extra distance the 13.2 g projectile penetrated.

Figure 4.34 shows quite clearly that there is excellent agreement between static and ballistic tests on both 4.25 g and 13.2 g projectiles, once the energy due to friction has been removed. Thus it is possible to predict v_{50} based on static deflection tests. This conclusion is obviously in disagreement with the results reported by Jenq *et al.* [1994], at least for this material.

Figure 4.34 suggests that S-2 glass reinforced phenolic is strain rate insensitive. It should be noted that the tests performed showing the strain rate sensitivity of GFRP were all done using the Hopkinson-bar technique. The materials tested were also not the same as the one tested in this thesis. Thus the only conclusion which can be drawn is that the through-thickness penetration behaviour of S-2 glass reinforced phenolic is insensitive to the rate of loading be it static or ballistic.

4.8 Summary

An experimental investigation has been undertaken on S-2 glass reinforced phenolic composites. Both the static and ballistic penetration were investigated and comparisons made. It was found that the agreement in both damage mechanisms and force-displacement curves was good.

The effect of cone angle, specimen thickness and impact velocity were all investigated and it was found that increasing the cone angle from 37° to 120° had an effect similar to that of increasing

the thickness (i.e. increasing the apparent stiffness of the panel) on both the force-displacement curve and the damage mechanisms. The projectiles with a 120° cone angle triggered a delamination not seen with the 37° projectiles. The depth of this delamination was also found to increase as the impact velocity increased.

Finally a comparison between the ballistic and static perforation energies was made and it was found that when the energy absorbed due to friction was removed the perforation energies were very close.

Table 4.1. Summary of static and ballistic tests performed on GFRP laminates.

Test #	Date	Thickness inches	Cone Angle degrees	Test	Projectile Mass g	Velocity m/s
96-b-2012-1	20-Dec-96	0.50	37	ballistic	4.20	379
97-b-2012-2	20-Dec-96	0.75	37	ballistic	4.20	364
96-b-2012-3	20-Dec-96	0.25	37	ballistic	4.20	236
97-b-2401-1	24-Jan-97	0.25	37	ballistic	13.2	284
97-b-2401-2	24-Jan-97	0.25	37	ballistic	13.2	162
97-b-2702-1	27-Feb-97	0.25	37	ballistic	13.2	175
97-b-2702-2	27-Feb-97	0.25	37	ballistic	13.2	108
97-b-2702-3	27-Feb-97	0.25	37	ballistic	13.2	159
97-b-0303-1	3-Mar-97	0.25	37	ballistic	13.2	151
97-b-1203-1	12-Mar-97	0.75	37	ballistic	13.2	235
97-b-2103-1	21-Mar-97	0.75	37	ballistic	13.2	340
97-b-2403-1	24-Mar-97	0.75	37	ballistic	13.2	207
97-b-2403-2	24-Mar-97	0.75	37	ballistic	13.2	267
97-b-2403-3	24-Mar-97	0.75	37	ballistic	13.2	398
97-b-1804-1	18-Apr-97	0.50	37	ballistic	4.26	320
97-b-1804-2	18-Apr-97	0.50	120	ballistic	4.19	357
97-b-1804-3	18-Apr-97	0.50	120	ballistic	4.24	393
97-b-1804-4	18-Apr-97	0.75	37	ballistic	4.29	422
97-s-2404-3	24-Apr-97	0.75	37	static deflection	/	/
97-s-2404-4	24-Apr-97	0.50	37	static deflection	/	/
97-s-2504-1	25-Apr-97	0.50	120	static deflection	/	/
97-s-2504-3	25-Apr-97	0.75	120	static deflection	/	/
97-b-2804-1	28-Apr-97	0.50	120	ballistic	4.25	478
97-b-2804-2	28-Apr-97	0.50	120	ballistic	4.23	525
97-b-2804-3	28-Apr-97	0.50	120	ballistic	4.25	554
97-b-2804-4	28-Apr-97	0.75	120	ballistic	4.26	554
97-b-2804-5	28-Apr-97	0.75	120	ballistic	4.26	617
97-b-1205-1	12-May-97	0.50	37	ballistic	13.2	142
97-b-1205-2	12-May-97	0.50	37	ballistic	13.2	171
97-b-1505-1	15-May-97	0.75	120	ballistic	13.2	384
97-b-1605-1	16-May-97	0.50	37	ballistic	13.2	171
97-b-1605-2	16-May-97	0.50	37	ballistic	13.2	203
97-b-1605-3	16-May-97	0.50	37	ballistic	13.2	266
97-b-1605-4	16-May-97	0.50	37	ballistic	13.2	304
97-b-1605-5	16-May-97	0.50	120	ballistic	13.2	278
97-b-2005-1	20-May-97	0.50	120	ballistic	13.2	221
97-b-2005-2	20-May-97	0.25	37	ballistic	13.2	71
97-b-2005-3	20-May-97	0.25	37	ballistic	13.2	104
97-b-2005-4	20-May-97	0.25	37	ballistic	13.2	122
97-b-2005-5	20-May-97	0.75	37	ballistic	13.2	153
97-b-2005-6	20-May-97	0.75	120	ballistic	13.2	330
97-s-2305-1	23-May-97	0.25	37	static deflection	/	/
97-s-2305-2	23-May-97	0.25	120	static deflection	/	/
97-si-2305-1	23-May-97	0.75	37	static indentation	/	/
97-si-2305-2	23-May-97	0.75	120	static indentation	/	/
97-b-3005-1	30-May-97	0.75	120	ballistic	4.25	628
97-b-3005-2	30-May-97	0.75	120	ballistic	4.25	626
97-b-3005-3	30-May-97	0.75	120	ballistic	4.25	726
97-b-3005-4	30-May-97	0.75	120	ballistic	4.25	861
97-b-0306-1	3-Jun-97	0.25	120	ballistic	13.2	244
97-b-0306-2	3-Jun-97	0.25	120	ballistic	13.2	211
97-b-0306-3	3-Jun-97	0.25	120	ballistic	13.2	178

Table 4.2. Frictional force between indenter and 6.35 mm (0.25″), 12.70 mm (0.50″) and 19.05 mm (0.75″) specimens.

Thickness (inches)	Thickness (mm)	Frictional Force (N)
0.25	6.35	2360 (calc.)
0.50	12.70	4720 (exp.)
0.75	19.05	7080 (calc.)

Table 4.3. Comparison between perforation energies obtained from static deflection and ballistic tests with projectile mass of 4.25 g and 13.2 g.

Thickness (inches)	Thickness (mm)	Areal Density (kg/m^2)	37° Cone Angle Static (J)	Ballistic m=4.25 g (J)	Ballistic m=13.2 g (J)	120° Cone Angle Static (J)	Ballistic m=13.2 g (J)
0.25	6.35	12.1	121	118	150	/	264
0.50	12.70	24.1	228	218	271	/	615
0.75	19.05	36.2	407	378	365	/	920
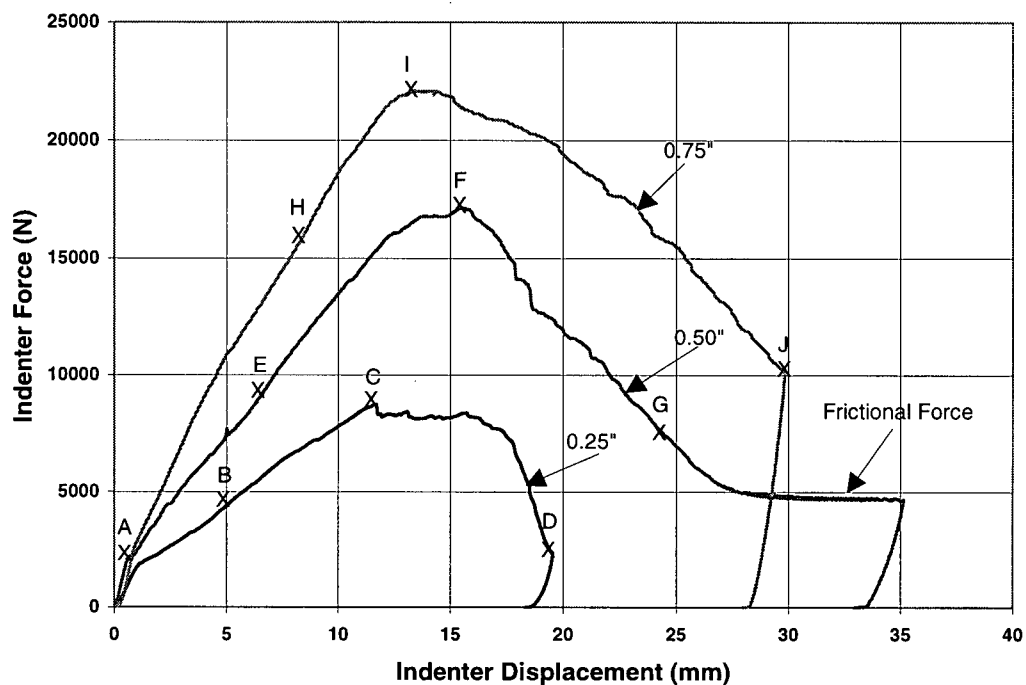
Figure 4.1. Load-displacement curves for GFRP static deflection tests (37° indenter).
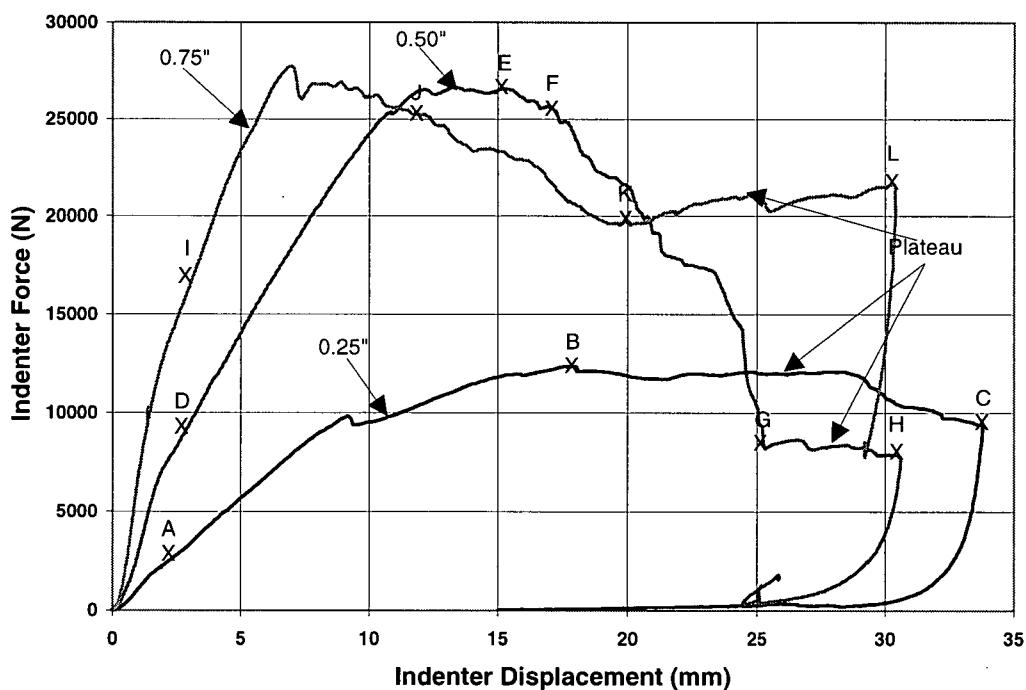
Figure 4.2. Load-displacement curves for GFRP static deflection tests (120° indenter).
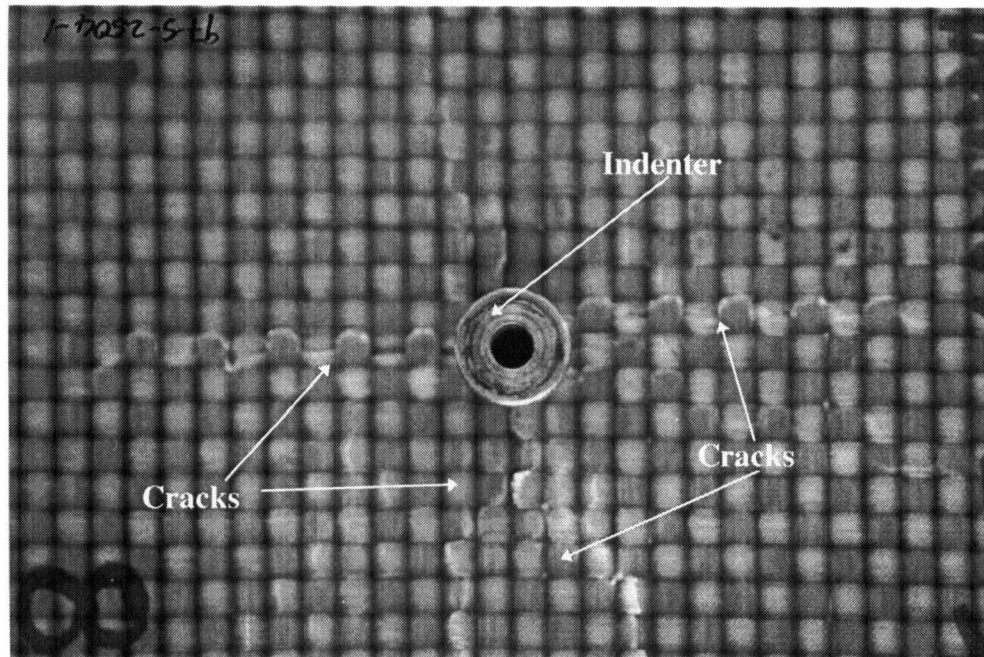
Figure 4.3. Picture showing front face matrix cracks on GFRP specimens.
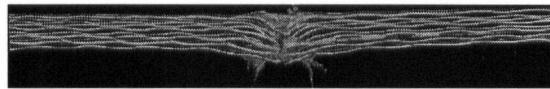
Test Type	Test #	Thickness(in)
Static 37°	97-s-2305-1	0.25

Figure 4.4. Micro-graph corresponding to point D.
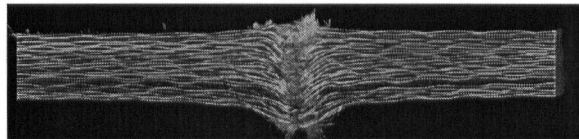
Test Type	Test #	Thickness(in)
Static 37°	97-s-2404-4	0.50

Figure 4.5. Micro-graph corresponding to point G.
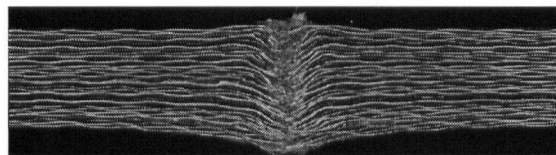
Test Type	Test #	Thickness(in)
Static 37°	97-s-2404-3	0.75

Figure 4.6. Micro-graph corresponding to point J.
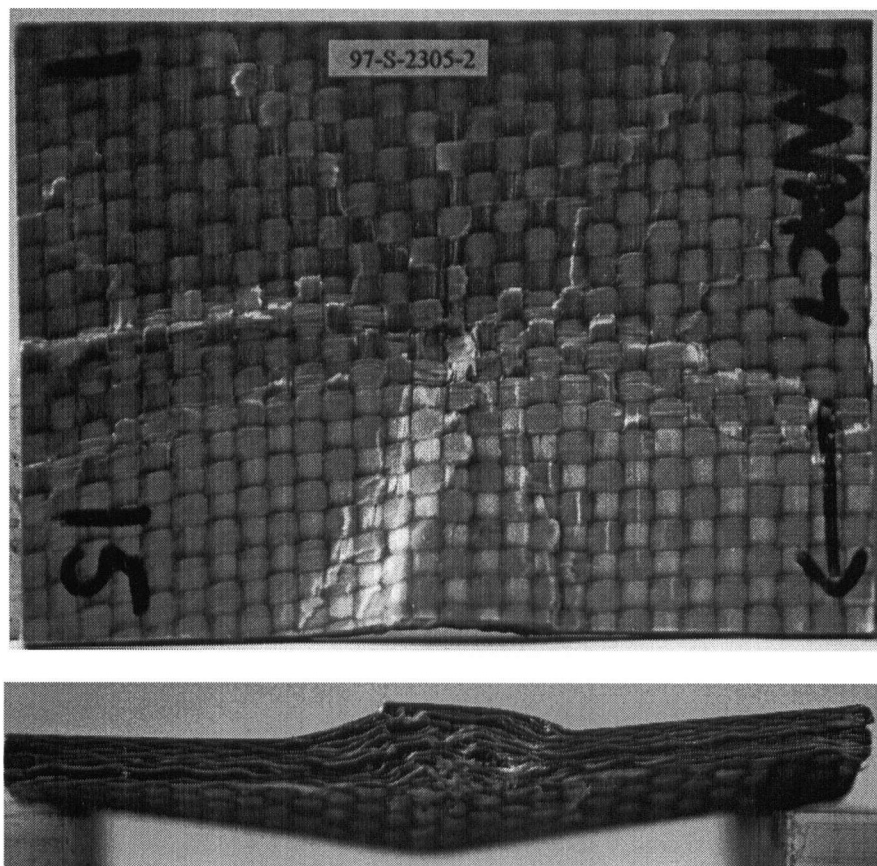
Figure 4.7. Top and side view showing a damaged 6.35 mm (0.25″) specimen with no penetration.
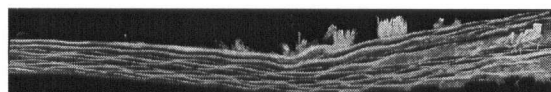
Test Type	Test #	Thickness(in)
Static 120°	97-s-2305-2	0.25

Figure 4.8. Micro-graph corresponding to point C (this is a cross-section of Figure 4.7).
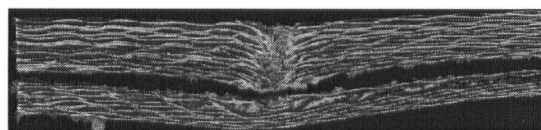
Test Type	Test #	Thickness(in)
Static 120°	97-s-2504-1	0.50

Figure 4.9. Micro-graph corresponding to point H.
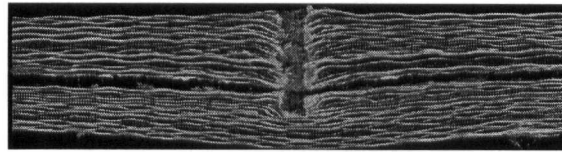
Test Type	Test #	Thickness(in)
Static 120°	97-s-2504-3	0.75

Figure 4.10. Micro-graph corresponding to point L.
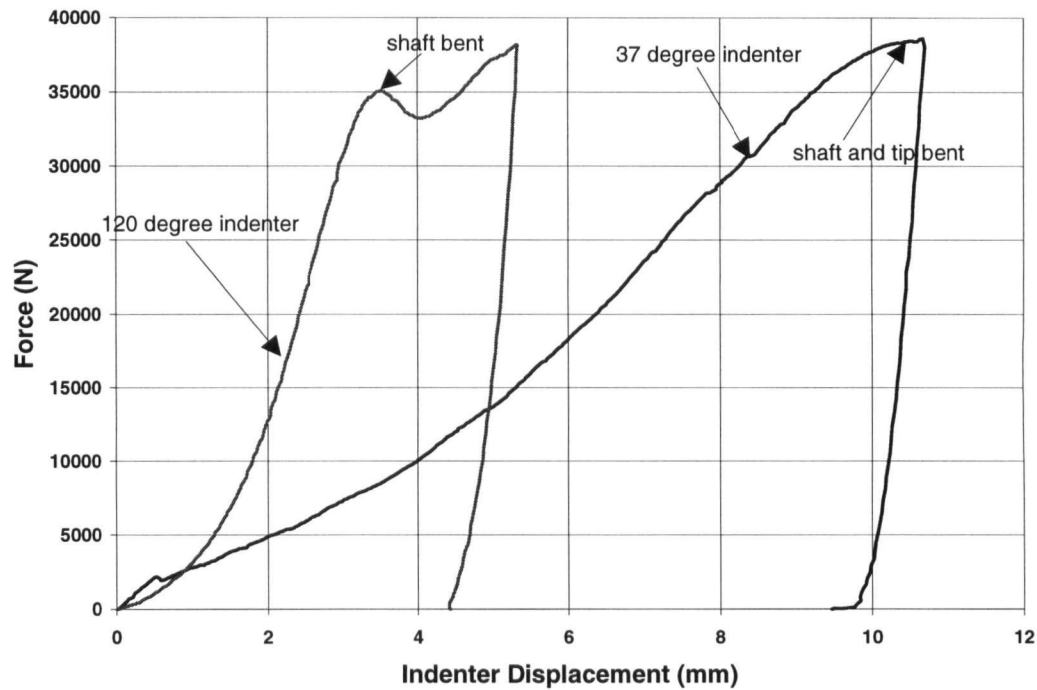
Figure 4.11. Static indentation of GFRP laminates by 37° and 120° indenters.
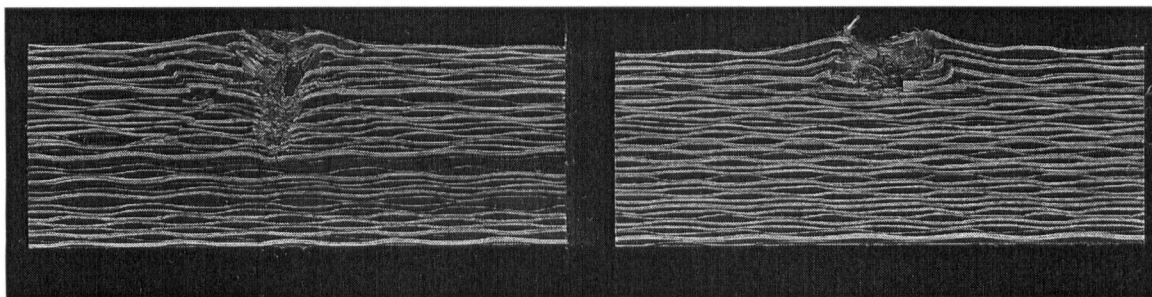
Figure 4.12. Micro-graphs showing damage from static indentation on a 19.05 mm (0.75″) thick GFRP by a 37° indenter (left) and a 120° indenter (right) .
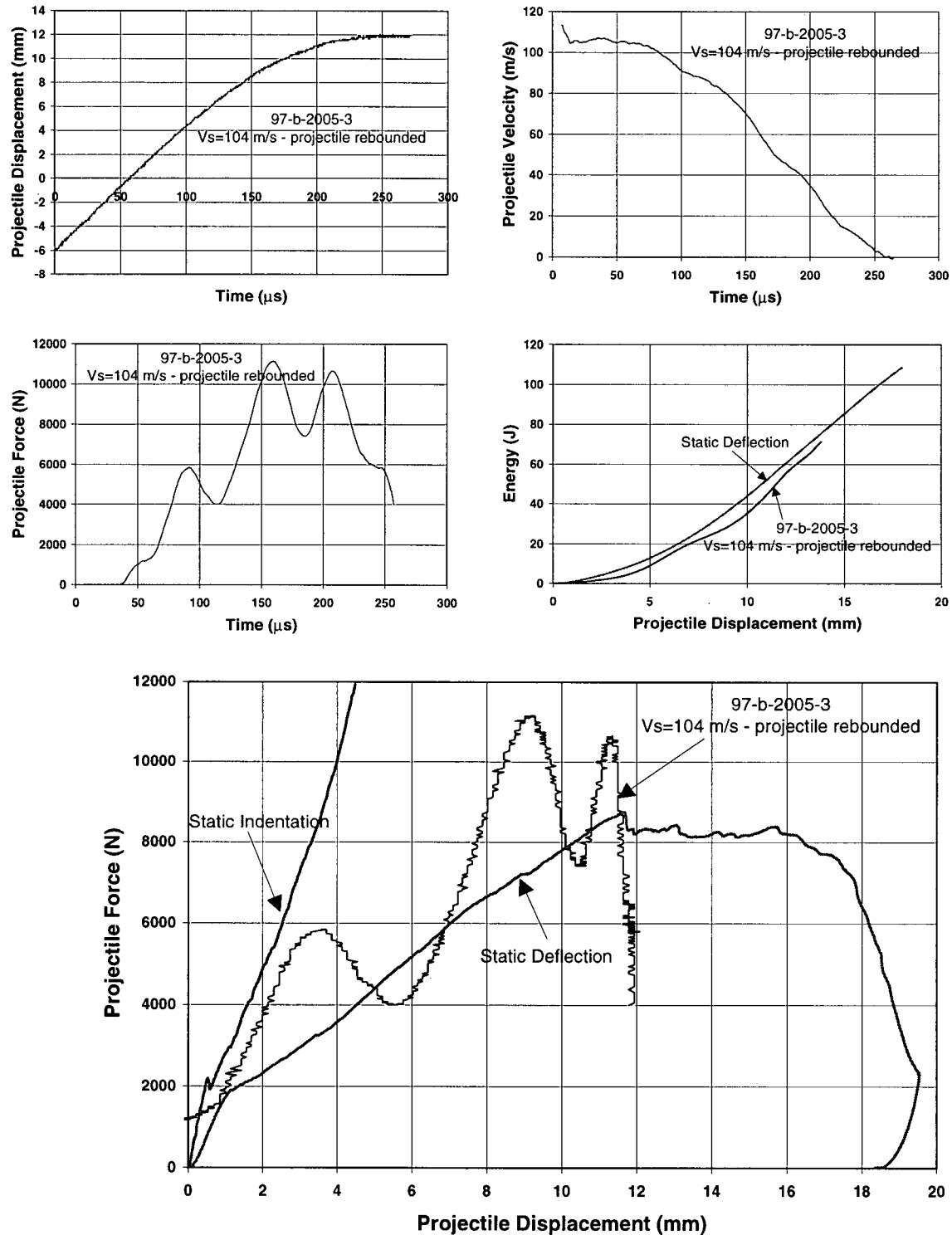
Figure 4.13. Displacement-time, velocity-time, force-time, energy-displacement and force-displacement for 6.35 mm (0.25″) thick GFRP specimens impacted by 13.2 g 37° projectiles.
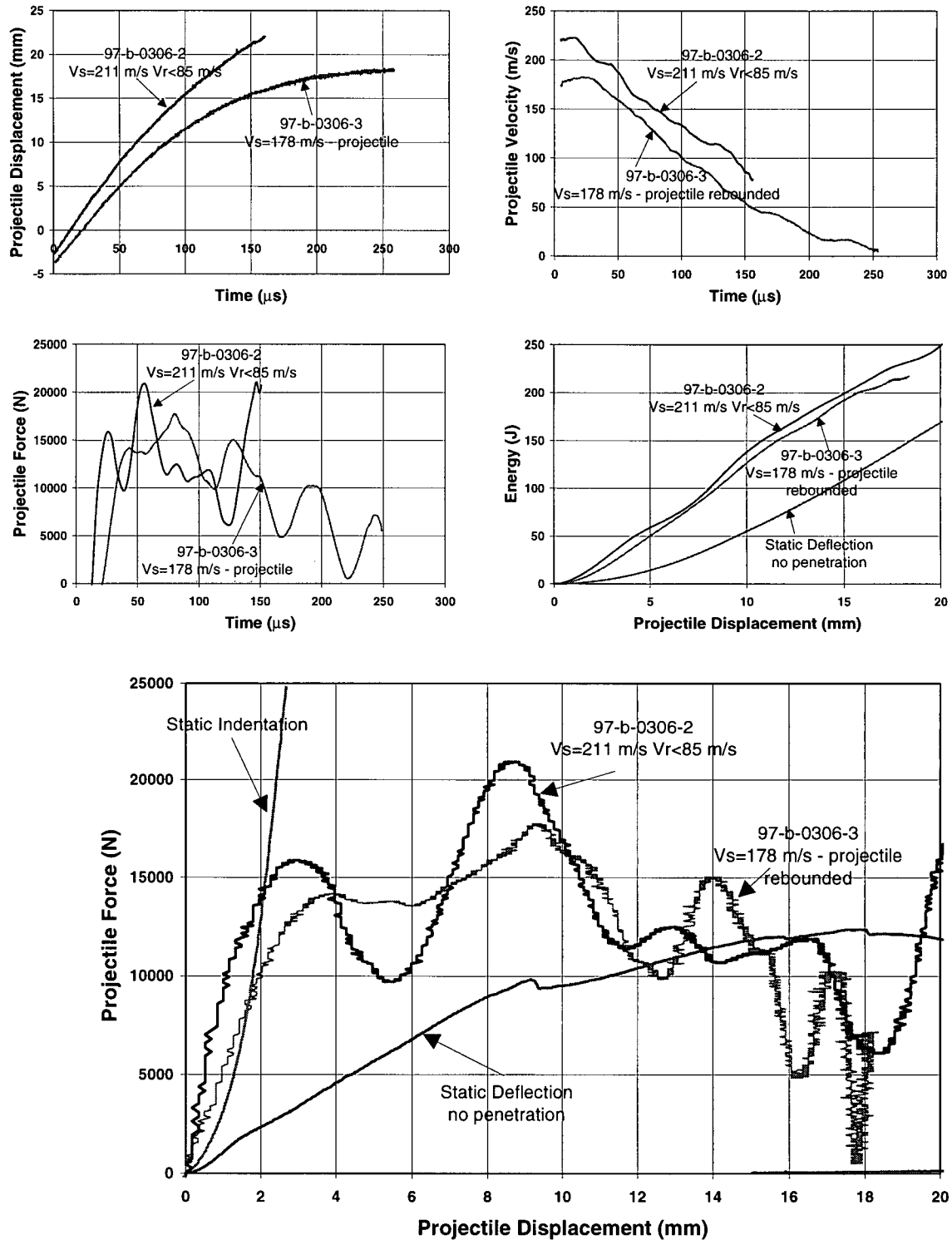
Figure 4.14. Displacement-time, velocity-time, force-time, energy-displacement and force-displacement for 6.35 mm (0.25″) thick GFRP specimens impacted by 13.2 g 120° projectiles.
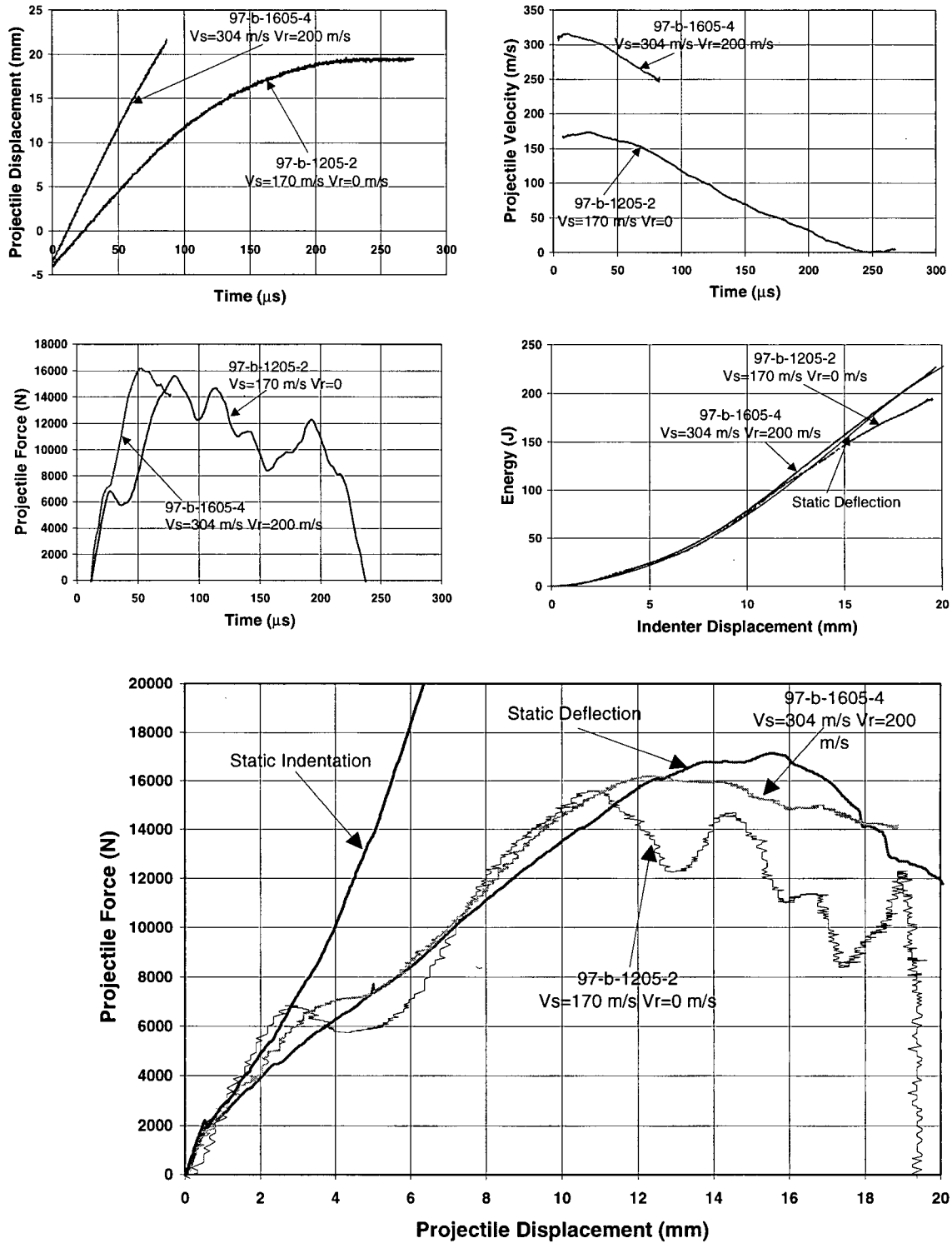
Figure 4.15. Displacement-time, velocity-time, force-time, energy-displacement and force-displacement for 12.70 mm (0.50″) thick GFRP specimens impacted by 13.2 g 37° projectiles.
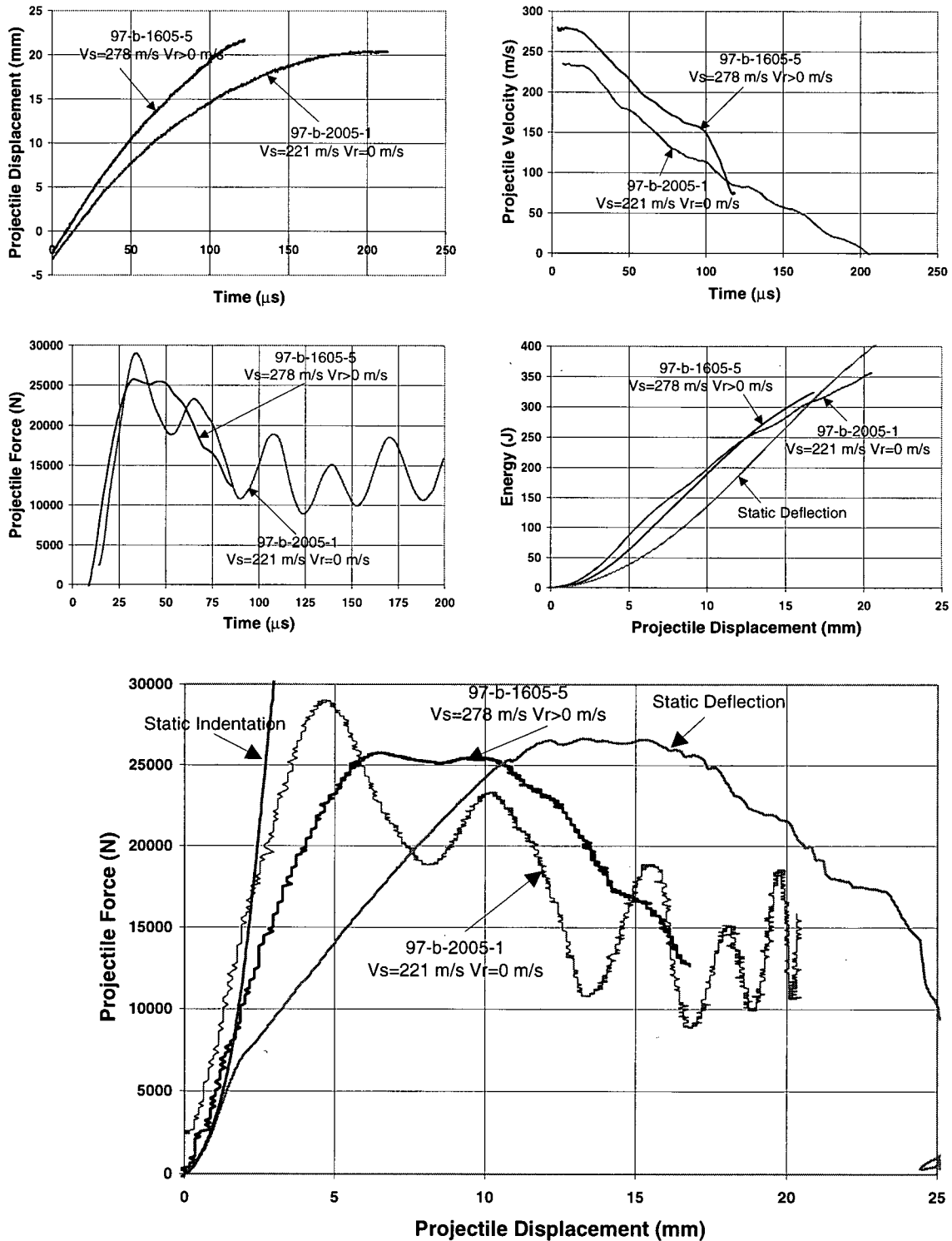
Figure 4.16. Displacement-time, velocity-time, force-time, energy-displacement and force-displacement for 12.70 mm (0.50″) thick GFRP specimens impacted by 13.2 g 120° projectiles.
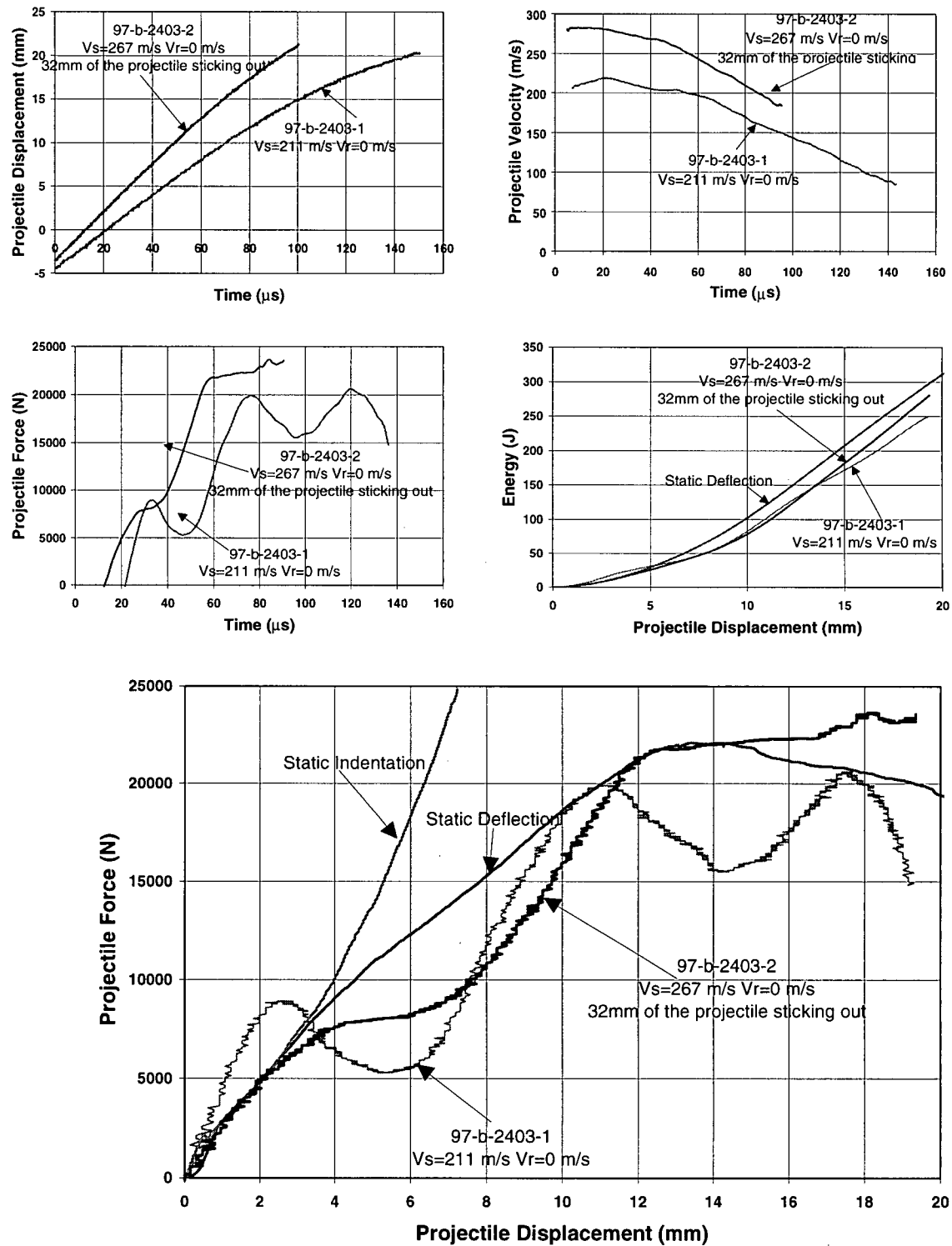
Figure 4.17. Displacement-time, velocity-time, force-time, energy-displacement and force-displacement for 19.05 mm (0.75″) thick GFRP specimens impacted by 13.2 g 37° projectiles.
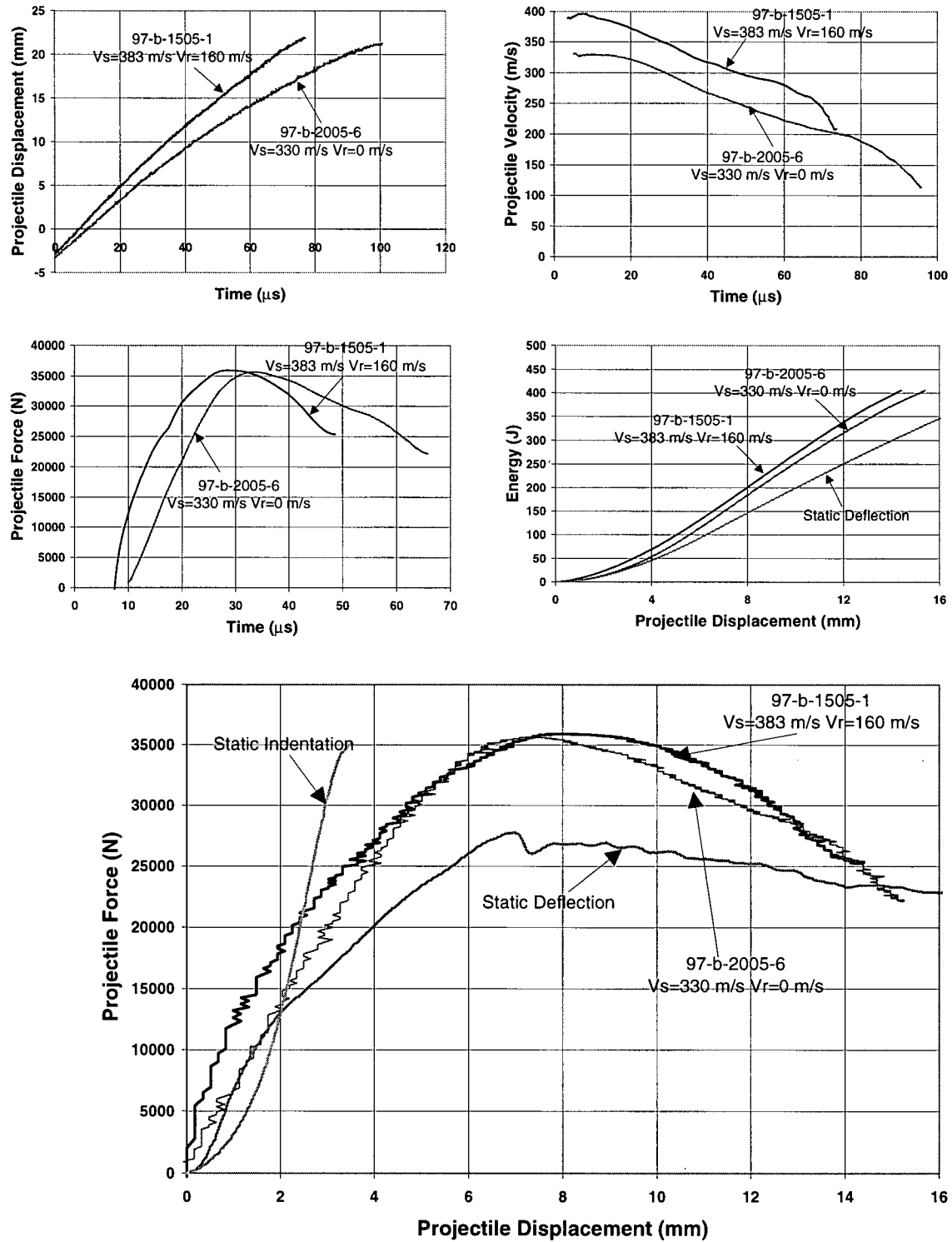
Figure 4.18. Displacement-time, velocity-time, force-time, energy-displacement and force-displacement for 19.05 mm (0.75″) thick GFRP specimens impacted by 13.2 g 120° projectiles.
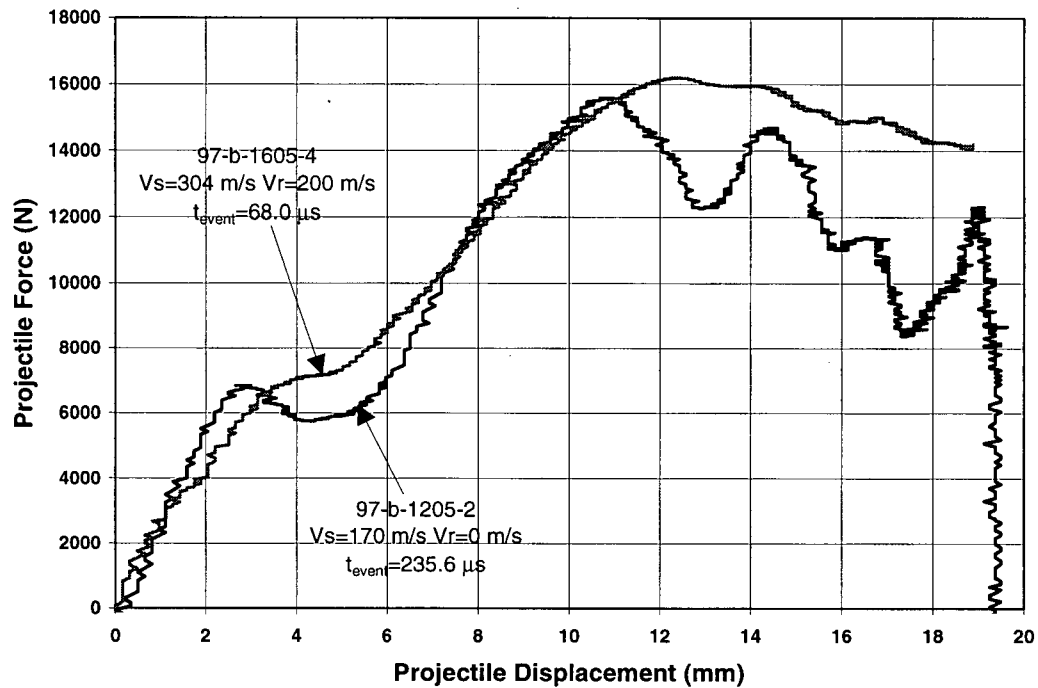
Figure 4.19. Load-displacement curve showing effect of impact velocity on 12.70 mm (0.50″) thick GFRP specimens impacted by 37° projectiles.
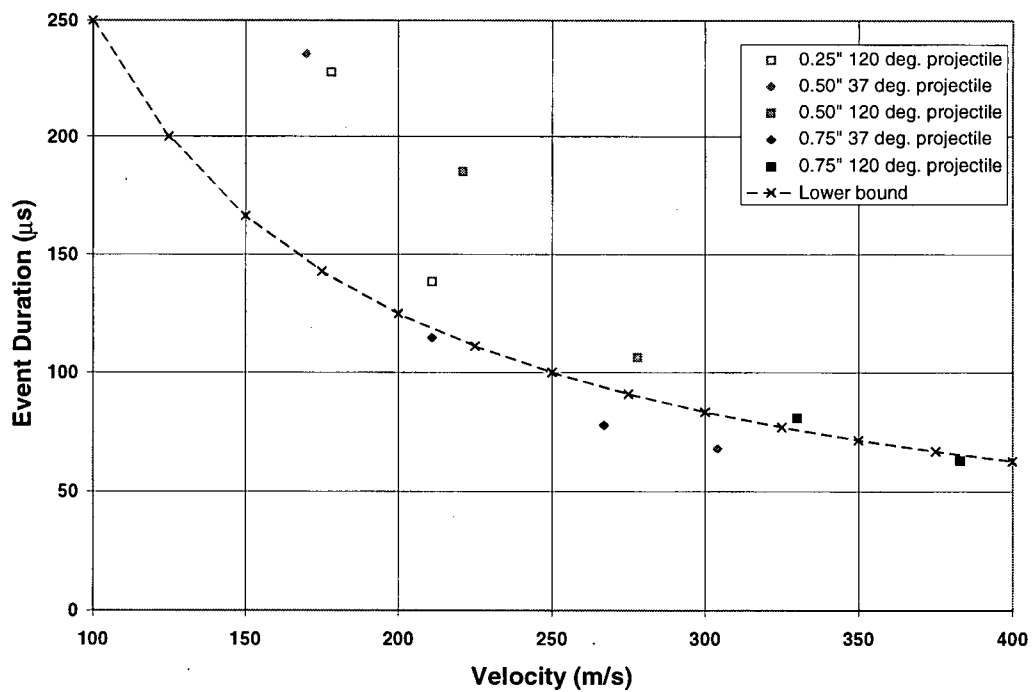
Figure 4.20. Curve showing effect of increasing the impact velocity for 6.35 mm (0.25″), 12.70 mm (0.50″) and 19.05 mm (0.75″) thick GFRP specimens.
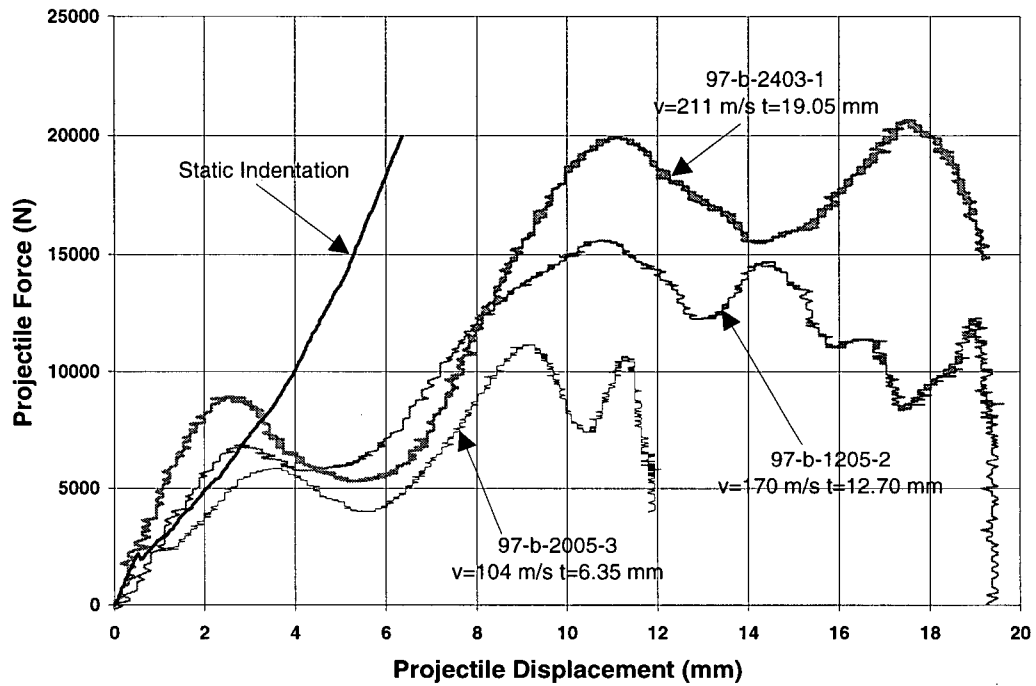
Figure 4.21. Load-displacement curves showing effect of changing the thickness of GFRP specimens impacted by 37° projectiles.
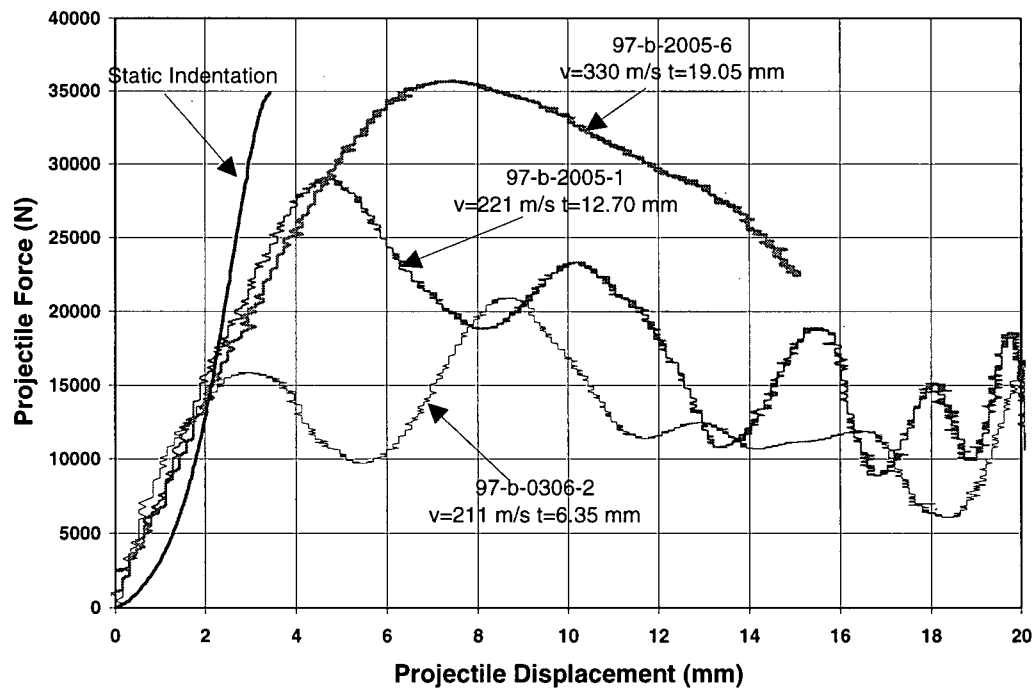
Figure 4.22. Load-displacement curves showing effect of changing the thickness of GFRP specimens impacted by 120° projectiles.
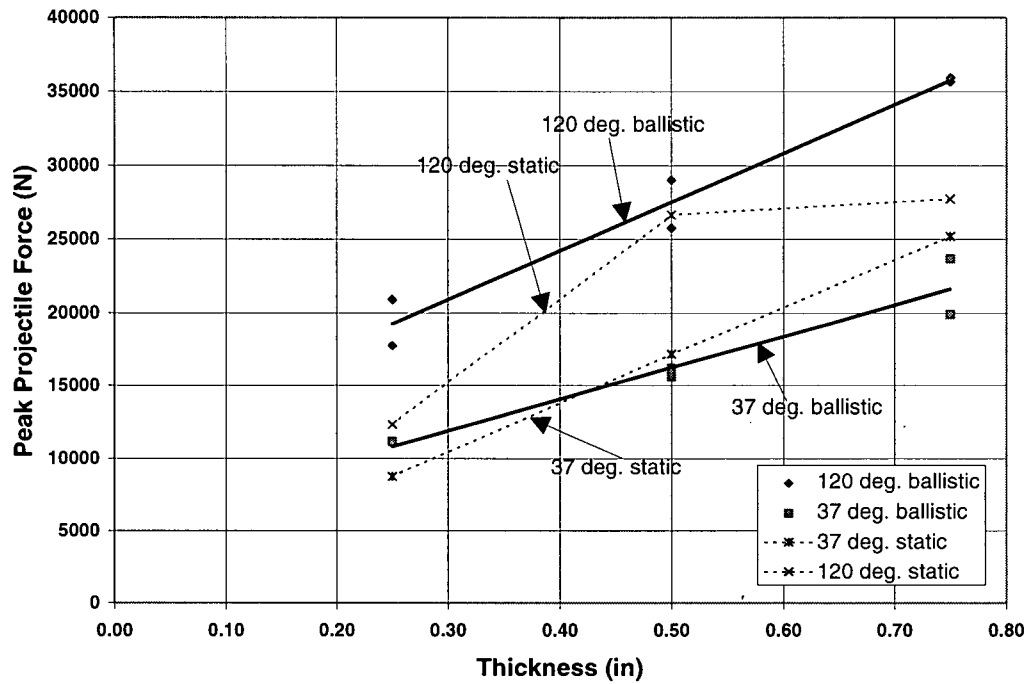
Figure 4.23. Curve showing the effect of increasing the specimen thickness for projectile and indenter cone angles of 37° and 120°.
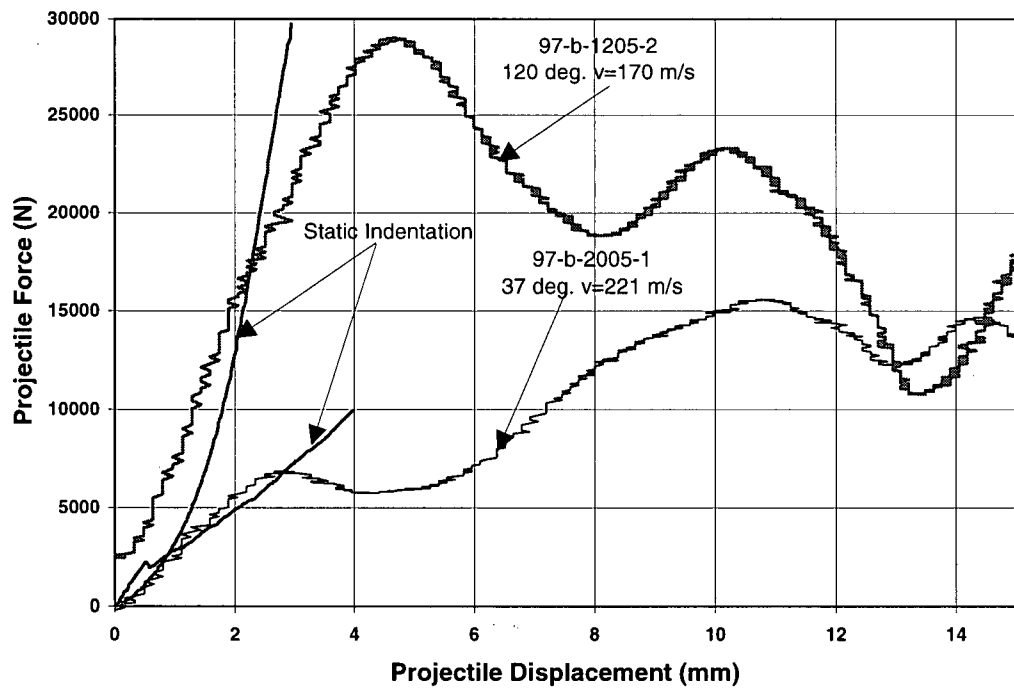
Figure 4.24. Load-displacement curves showing effect of changing the projectile cone angle from 37° to 120° on a 12.70 mm (0.50″) thick GFRP specimen.
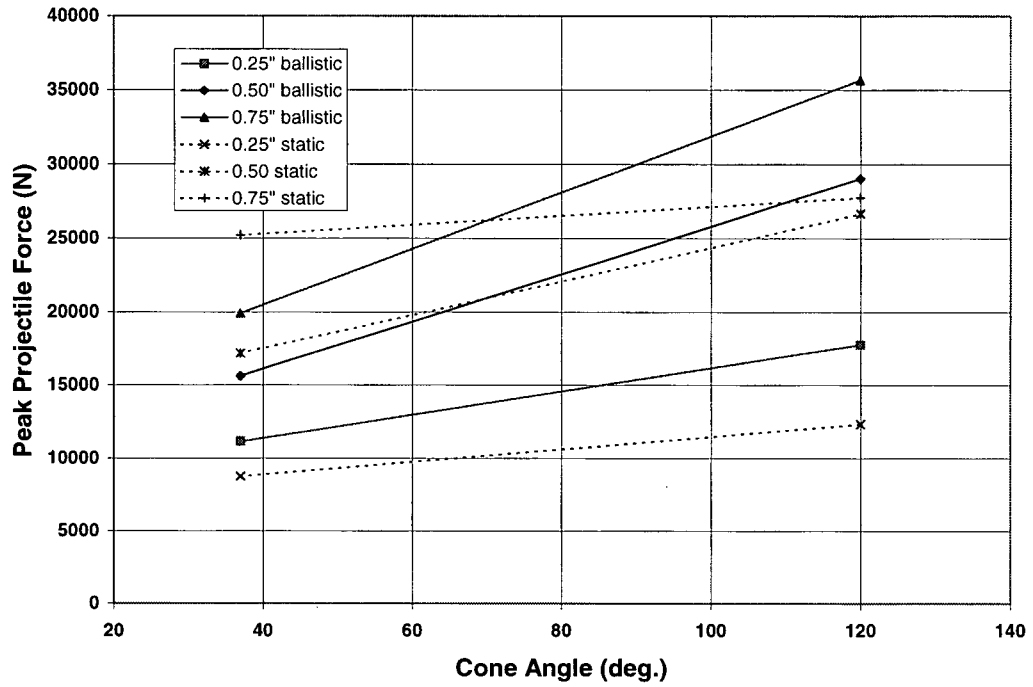
Figure 4.25. Curve showing the effect of changing the projectile cone angle from 37° to 120°.
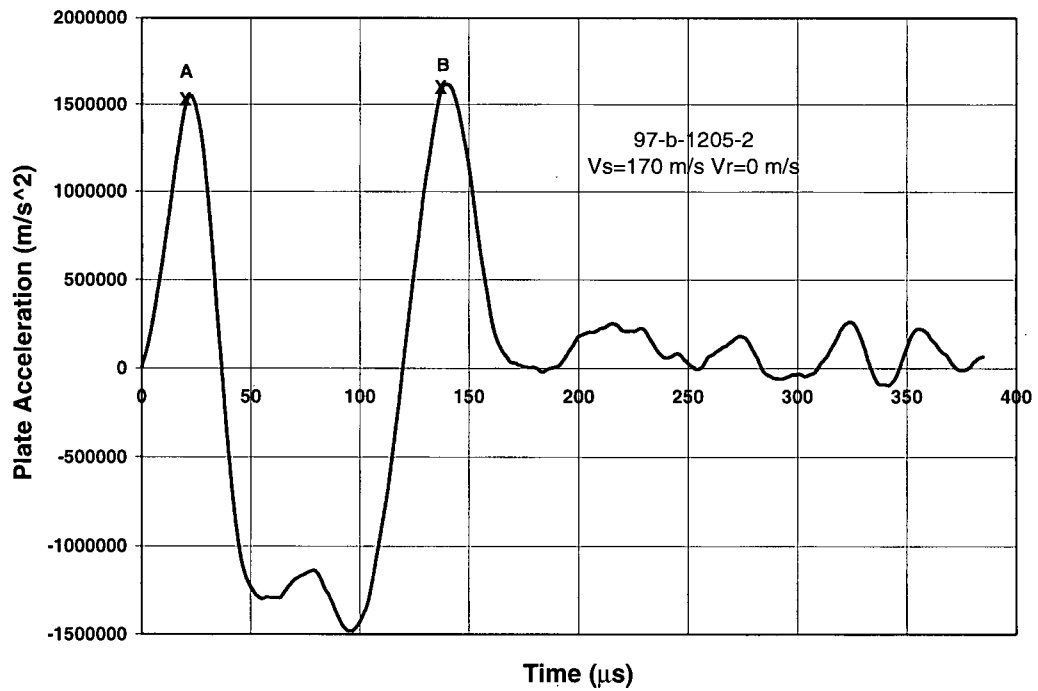
Figure 4.26. Acceleration-time curve showing free vibration of a 12.70 mm (0.50″) thick GFRP specimen.
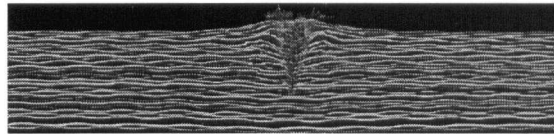
Striking Energy (J)	Test Number	Thickness (in)	Delam. Depth (mm)
154	97-b-2005-5	0.75	none

(a)
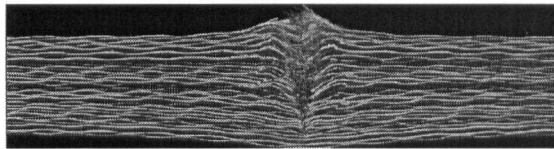
Striking Energy (J)	Test Number	Thickness (in)	Delam. Depth (mm)
284	97-b-2403-1	0.75	none

(b)
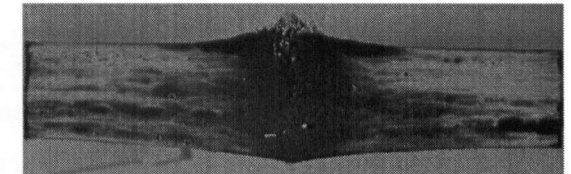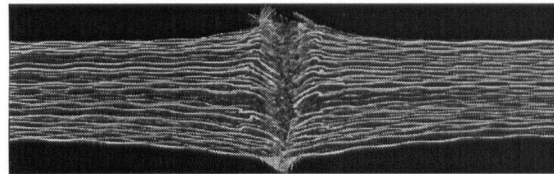
Striking Energy (J)	Test Number	Thickness (in)	Delam. Depth (mm)
365	97-b-1203-1	0.75	none

(c)
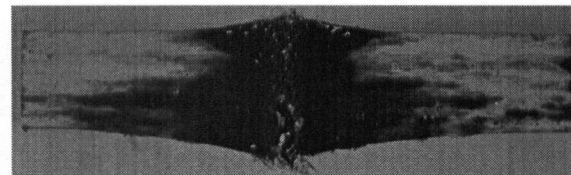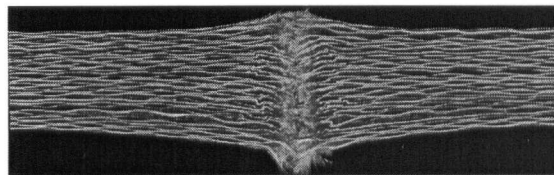
Striking Energy (J)	Test Number	Thickness (in)	Delam. Depth (mm)
469	97-b-2403-2	0.75	none

(d)
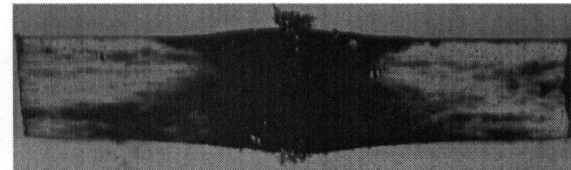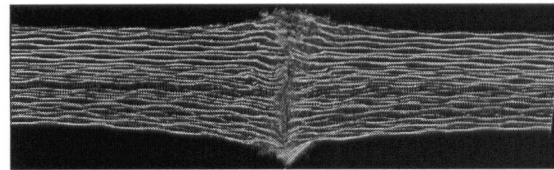
Striking Energy (J)	Test Number	Thickness (in)	Delam. Depth (mm)
763	97-b-2103-1	0.75	none

(e)

Figure 4.27. Micro-graphs showing (a) 154 J (b) 284 J (c) 365 J (d) 469 J and (e) 763 J impact on 19.05 mm (0.75″) GFRP laminates by projectiles with a 37° cone angle. The photograph of the specimen is shown on the left, while the result of the dye penetrant test is shown on the right.

Striking Energy (J)	Test Number	Sub-Laminate (mm)	Delam. Depth (mm)
267	97-b-1804-2	6.10	N/A

(a)

Striking Energy (J)	Test Number	Sub-Laminate (mm)	Delam. Depth (mm)
327	97-b-1804-3	5.75	5.45

(b)

Striking Energy (J)	Test Number	Sub-Laminate (mm)	Delam. Depth (mm)
486	97-b-2804-1	3.95	8.75

(c)

Striking Energy (J)	Test Number	Sub-Laminate (mm)	Delam. Depth (mm)
583	97-b-2804-2	2.03	11.20

(d)

Striking Energy (J)	Test Number	Sub-Laminate (mm)	Delam. Depth (mm)
652	97-b-2804-3	1.21	11.60

(e)

Figure 4.28. Micro-graphs showing (a) 267 J (b) 327 J (c) 486 J (d) 583 J and (e) 652 J impact on 12.70 mm (0.50″) GFRP laminates by projectiles with a 120° cone angle. The photograph of the specimen is shown on the left, while the digitised image is shown on the right.
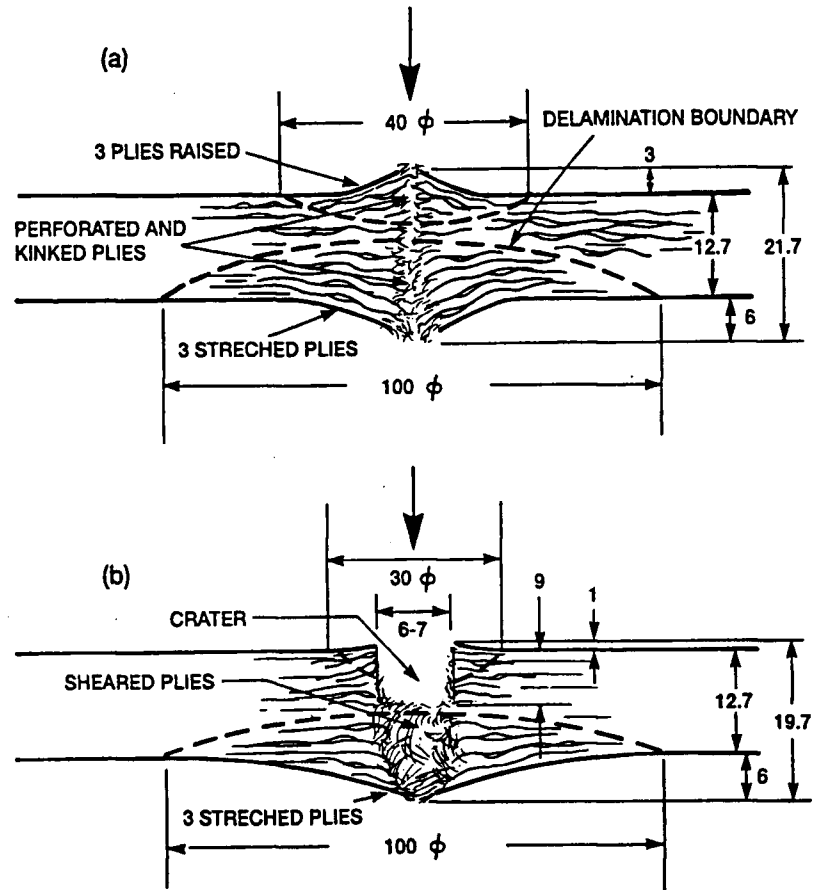
Figure 4.29. Schematic showing difference in penetration cavities caused by hemispherical (or conical) and blunt nose projectiles (from Bless *et al.* [1990]).
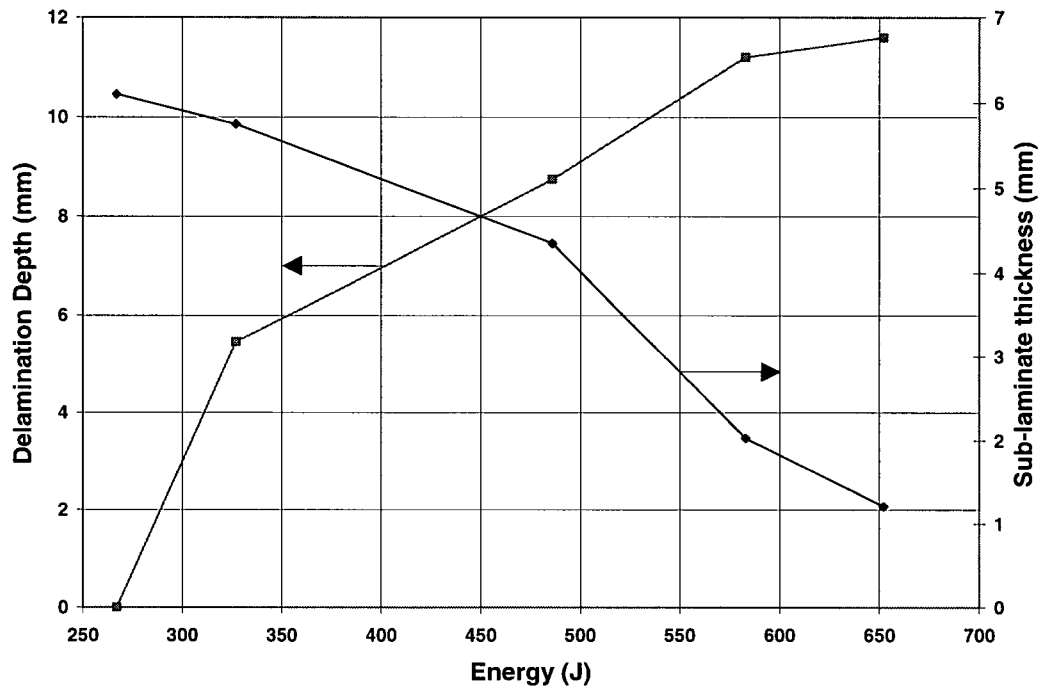
Figure 4.30. Relationship between delamination depth, sub-laminate thickness and impact energy for a 12.70 mm (0.50″) thick GFRP specimen.
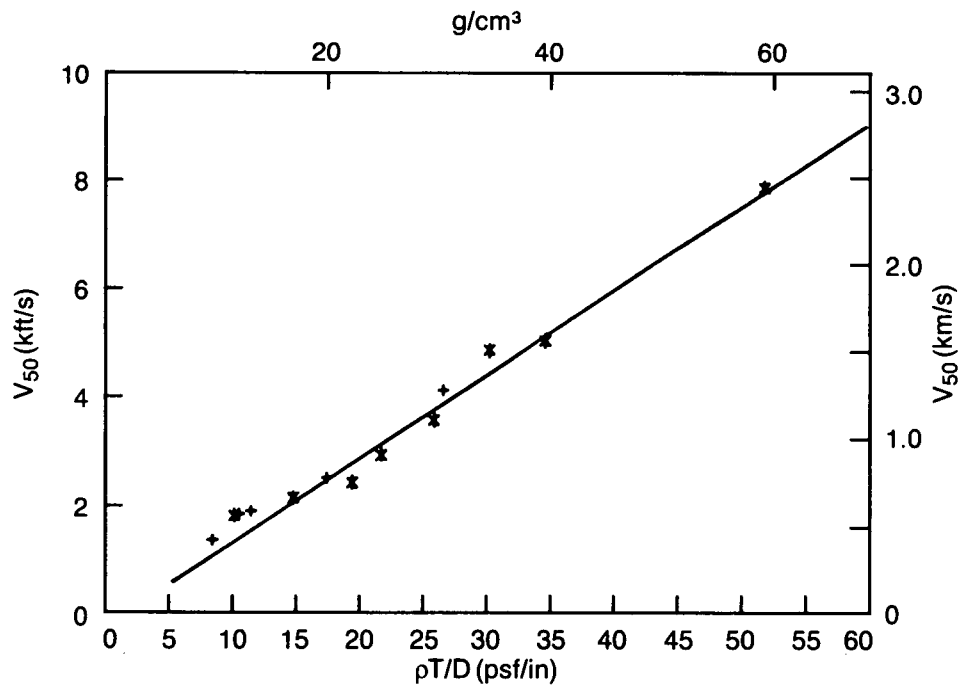
Figure 4.31. Plot showing relationship between v_{50} and areal density (from Bless *et al.* [1989]).
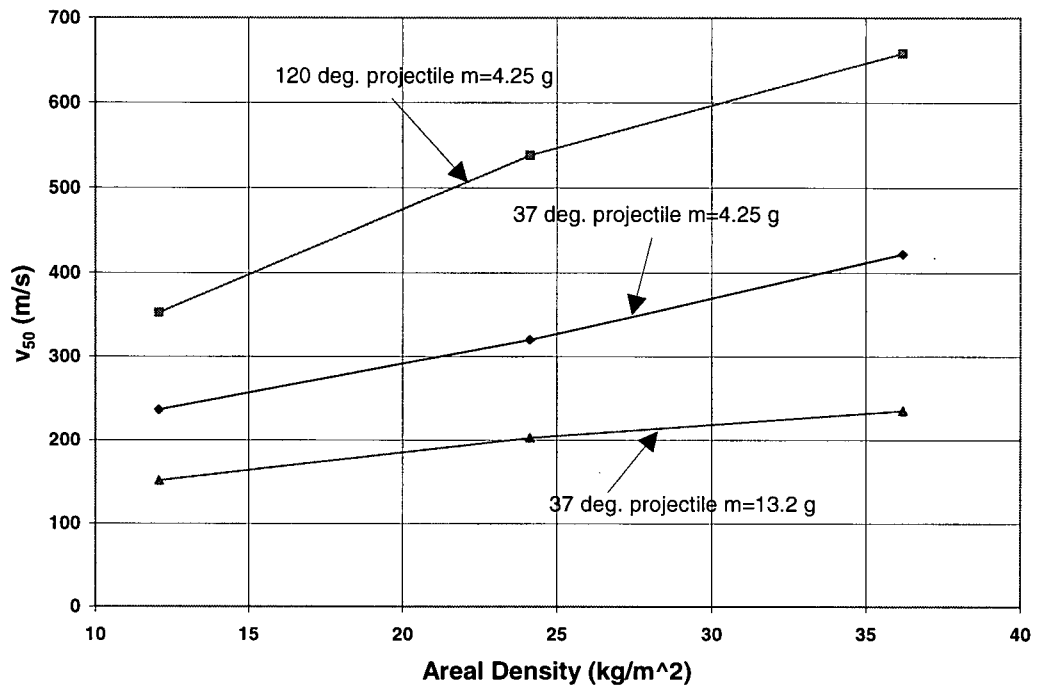
Figure 4.32. Relationship between v_{50} and areal density for projectile cone angles of 37° and 120°.
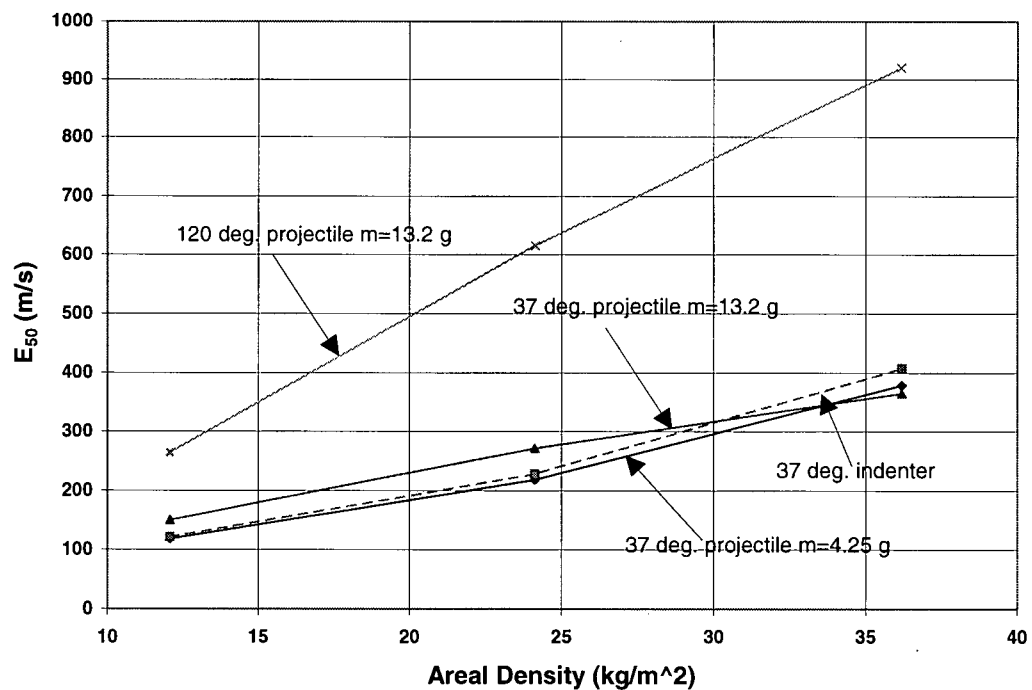
Figure 4.33. Relationship between E_{50} and areal density for projectile cone angles of 37° and 120°.
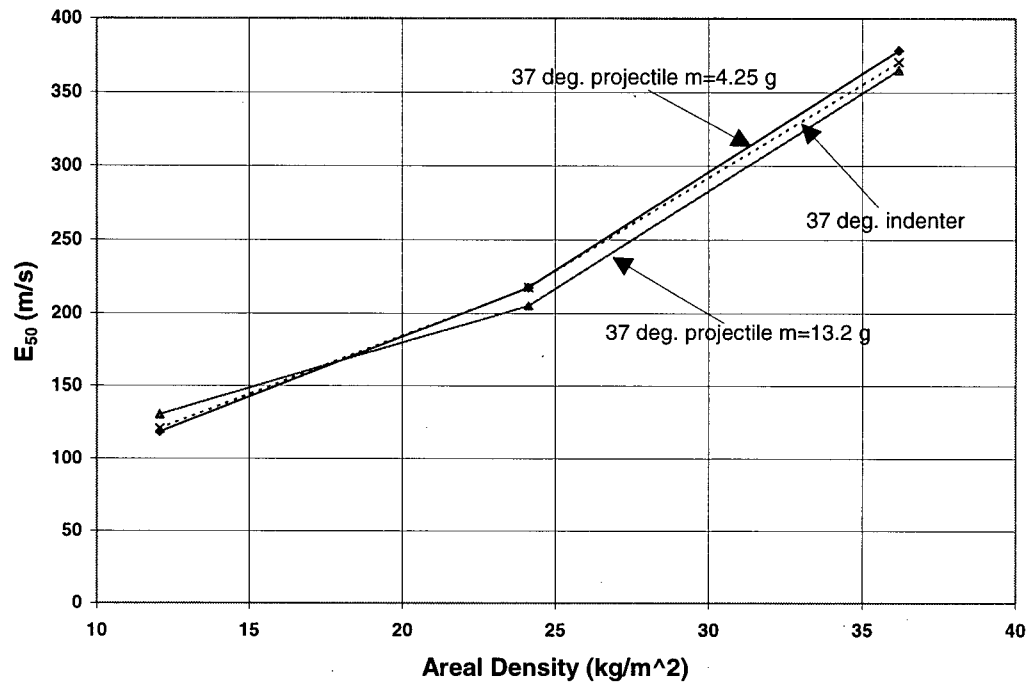
Figure 4.34. Relationship between E_{50} (with energy absorbed due to friction removed) and areal density for a projectile cone angle of 37°.

Chapter Five

Summary and Future Work

5.1 Summary

Penetration behaviour of two fairly distinct material systems, glass fibre reinforced polymer (GFRP) and carbon fibre reinforced polymer (CFRP) laminates has been studied. A measurement system that can continuously measure the force during a ballistic test has been developed and successfully used to obtain force-displacement curves for cylindro-conical projectiles (with 37° and 120° cone angles) penetrating GFRP laminates.

The damage progression in CFRP has been investigated and the main damage mechanisms identified. The CFRP panels were penetrated by an indenter with a 37° cone angle. Initially the specimen experiences pure bending but no penetration by the indenter. This is characterised as the elastic bending in the plate. Penetration is the first damage mechanism, followed closely by back face bulging. Matrix cracks initiate after bulging and are caused by high interlaminar stresses. The matrix cracks grow, and when they reach a critical size delamination starts. The delaminations grow and the next major damage mechanism is back face splitting. As the back face fails the damage spreads very quickly and the specimen is considered to have failed at this point.

The damage progression for GFRP was quite different than that of CFRP. Once again a 37° indenter was used to study the damage progression. The main difference between CFRP and GFRP was that there was no well defined transition between the damage mechanisms in the GFRP laminates. Delamination also occurred in a different form to CFRP. Delamination in a traditional sense is the separation of two plies and in most cases is visible to the naked eye. For GFRP, however, the delaminations were not visible and dye penetrant tests had to be performed to show the delamination. The GFRP essentially softened as opposed to separating. The GFRP tested had a high fibre volume fraction compared to CFRP (70 % compared to 45 %). This made it easier for the fibres to separate from the resin rather than plies separating from each other. The load-displacement curve for GFRP exhibited an increase to the peak force, and then the force decreased due to the extensive damage in the specimen. There was no back face splitting, no major load drops and no change of slope in the load-displacement curves.

Changing the indenter cone angle from 37° to 120° had a significant effect on the damage mechanisms in GFRP. For the first time a delamination was seen. As the 120° indenter penetrated a point was reached in the penetration process where the indenter literally tore off a sub-laminate. The reason the indenter does this is that there is a critical thickness which determines whether or not the indenter will penetrate. This critical thickness was found to be approximately 6 mm. This meant that for the thinnest specimen (6.35 mm) the indenter never penetrated under static loading and under ballistic impact either the projectile rebounded at low velocities, or perforated at high velocities (i.e. was never captured by the specimen). It was further found that the delaminated sub-laminate thicknesses of the 12.70 mm (0.50″) and 19.05 mm (0.75″) thick specimens were close to the critical thickness.

The ballistic tests for GFRP showed very good agreement with to the static tests in both force-displacement and damage modes. The force-displacement curves were analysed and the effect of changing impact velocity, specimen thickness and projectile cone angle were investigated. Increasing the impact velocity had the effect of reducing the impact duration and reducing the time the specimen had to respond to the impact. As expected increasing the thickness increased the bending stiffness of the specimens. It was also found that changing the cone angle had the effect of changing the apparent stiffness of the specimen. In other words, a specimen impacted by a 37° projectile *appeared* to be stiffer when impacted by a 120° projectile.

Ballistic limits were obtained from the ballistic tests for 37° projectiles (m=4.25 and 13.2 g) and 120° projectiles (m=4.25 g). The ballistic limit was found to vary linearly with areal density. It was further found that the lighter projectiles have higher ballistic limits (for the same cone angle) and the 120° projectiles have a higher ballistic limit than the 37° projectiles (for the same mass). Therefore it would be expected that a blunt projectile has an even higher ballistic limit. In other words the perforation energy for a blunt projectile is higher than the perforation energy for a 37°. Thus a sharp tipped conical projectile is more threatening to GFRP laminates than a blunt projectile.

It should be noted that CFRP laminates show an opposite trend. From the literature (Delfosse and Poursartip [1995]) it was shown that blunt projectiles had a *lower* perforation energy than 37° projectiles. Thus, for CFRP, blunt projectiles are more of a threat than 37° projectiles.

Finally the perforation energies for the 37° projectiles were obtained from ballistic tests using 4.25 g and 13.2 g projectiles and from the static tests. One would expect that the perforation energies would all be the same. A direct measurement of the perforation energies showed that

this was not the case. However, by subtracting the energy absorbed by friction, excellent agreement was found. This indicates that it is possible to predict ballistic limits using static tests on a material that shows strain rate sensitivity when tested using other techniques.

5.2 Future Work

One area of research which needs further attention is the laser line velocity sensor (LLVS) system. The width of the sheet in the LLVS is currently 25.4 mm and sometimes the last 4 or 5 mm of penetration during an impact event are missed. It may be worth while to investigate widening the sheet to allow the measurement of large deflections.

The projectiles and gun powder that are used have limitations and a new projectile design needs to be considered. The problem with the projectiles is that at low velocities, they become very unstable and as a result can sometimes cause erroneous readings. The same instability is seen in the projectiles at high velocities. This, however, is due to the gun powder that is currently used. The gun powder is very volatile and at the energies needed for high velocities the powder explodes rather than burns at a constant rate. This leads to the instability in the projectile at high velocities. Thus a less volatile gun powder needs to be used.

With the LLVS system working efficiently it is now possible to obtain force-displacement curves for virtually any material. Another possible application of the LLVS is in measuring the back face motion of specimens during impact. The problem with the current set-up is that the current test fixture blocks the view of the back face of the specimens. So a new test fixture would have to be designed taking into account a second LLVS system.

The micro-delamination present in GFRP is difficult to observe under a microscope and limited success was obtained with the dye penetrant. A more robust technique to show the micro-delamination should be investigated. Detailed static penetration tests could then be performed highlighting the onset of micro-delamination and other damage mechanisms which are missing from the current study.

The combination of specimen thickness, cone angle and hole opening geometry determine the response of the specimen to an impact. This thesis used only one hole opening geometry and two cone angles. In reality there are an infinite number of possible combinations of test parameters. These test parameters interact with one another to give the response of the specimen. Thus it becomes important to understand how changing the test parameters affects the response of the specimen. With this understanding, a successful model can be developed.

Finally the numerical and analytical model currently under development at UBC should incorporate the damage mechanisms, progression of damage and force-displacement curves obtained from this work. With these models, parametric studies can be carried out to enable a more complete understanding of the impact and penetration of GFRP laminates.

References

Abrate S., 'Impact on laminated composite materials', *Appl. Mech. Rev.*, Vol. 44 (4), *1991*, pp. 155-190

Abrate S., 'Impact on laminated composite materials: Recent advances', *Appl. Mech. Rev.*, Vol. 47 (11), *1994*, pp. 517-544

Bless S.J., Hartman D.R. and Hanchak S.J., 'Ballistic Performance of Thick S-2 Glass Composites', Symposium on Composite Materials in Armament Applications, 20-22 August, *1985*

Bless S.J. and Hartman D.R., 'Ballistic Penetration of S-2 Glass Laminates', 21st International SAMPE Technical Conference, September 25-28, *1989*, pp. 852-866

Bless S.J., Benyami M. and Hartman D.R., 'Penetration Through Glass-reinforced Phenolic', 22nd International SAMPE Technical Conference, Boston, November, *1990*

Cantwell W.J. and Morton J., 'Detection of Impact Damage in CFRP Laminates', *Composite Structures*, Vol. 3, *1985*, pp. 241-257

Cantwell W.J. and Morton J., 'Comparison of the Low and High Velocity Impact Response of CFRP', *Composites*, Vol. 29 (6), *1989*, pp. 545-551

Cantwell W.J. and Morton J., 'Impact Perforation of Carbon Fibre Reinforced Plastic', *Composite Science and Technology*, Vol. 38, *1990*, pp. 119-141

Choi H.Y. and Chang F-K., 'Impact Damage Resistance of Graphite/Epoxy Laminated Composites', *Polymer Engineering and Science*, Vol. 31 (18), *1991a*, pp. 1294-1300

Choi H.Y., Downs R.J. and Chang F-K., 'A New Approach toward Understanding Damage Mechanisms and Mechanics of Laminated Composites Due to Low-Velocity Impact : Part I - Experiments', *Journal of Composite Materials*, Vol. 25, *1991b*, pp. 992-1011

Choi H.Y., Wu H-Y.T. and Chang F-K., 'A New Approach toward Understanding Damage Mechanisms and Mechanics of Laminated Composites Due to Low-Velocity Impact : Part II - Analysis', *Journal of Composite Materials*, Vol. 25, *1991c*, pp. 1012-1038

Chou S. and Kokido D., 'A Note on the Energy Absorption Mechanisms of GRP Composite Under Impact Loading', *Dynamic Response and Behaviour of Composites, ASME,* AD-Vol. 46, *1995*, pp. 43-63

Davies G.A.O. and Zhang X., 'Impact Damage Prediction in Carbon Composite Structures', *Int. J. Impact Engng.,* Vol. 16 (1), *1995*, pp. 149-170

Delfosse D., Pageau G., Bennett R. and Poursartip A., 'Instrumented Impact Testing at High Velocities', *Journal of Composites Technology & Research,* JCTRER, Vol. 15 (1), *1993*, pp. 38-45

Delfosse D., 'Experimental Results from Static and Dynamic Out-of-Plane Loading of Laminated Composite Materials', *Joint Report to Defence Research Establishment Valcartier and Directorate Research and Development Land, Department of National Defence,* The University of British Columbia, Metals and Materials Engineering Department, Vancouver, British Columbia, *1994*

Delfosse D. and Poursartip A., 'Experimental Parameter Study of Static and Dynamic Out-of-Plane Loading of CFRP Laminates', Proceedings of the Tenth International Conference on Composite Materials (ICCM X), Whistler, B.C., Canada, August, Vol. 5, *1995*, pp. 583-590

Espinosa H.D., Lu H-C. and Xu Y., 'A Novel Technique for Penetrator Velocity Measurement in Ballistic Penetration Studies', *ASME, 1996,* pp. 23-47

Goldsmith W., Dharan C.K.H. and Chang H., 'Quasi-Static and Ballistic Perforation of Carbon Fiber Laminates', *Int. J. Solids Structures,* Vol. 32 (1), *1995*, pp. 89-103

Gupta P.K. and Chiang F.P., 'Laser Speckle Interferometry Applied to Studying Transient Vibrations of a Cantilever Beam', *J. Sound Vib.,* Vol. 133 (2), *1989*, pp. 251-259

Harding J. and Welsh L.M., 'A Tensile Testing Technique for Fibre-reinforced Composites at Impact Rates of Strain', *J. Mater. Sci.,* Vol. 18, *1983*, pp. 1810-1826

Hodgkinson J., Vlachos N., Whitelaw J. and Williams J., 'Drop-Weight Impact Tests With the use of Laser-Doppler Velocimetry', *Proc Roy Soc London Series A Math Phys Sci,* Vol. 379 (1779), *1982*, pp. 133-144

Jenq S.T., Jing H-S. and Chung C., 'Predicting the Ballistic Limit for Plain Woven Glass/Epoxy Composite Laminate', *Int. J. Impact Engng.,* Vol. 15 (4), *1994*, pp. 451-464

Jih C.J. and Sun C.T., 'Prediction of Delamination in Composite Laminates Subjected to Low Velocity Impact', *Journal of Composite Materials,* Vol. 27 (7), *1993*, pp. 684-701

Kandasamy R. and Brar N.S., 'Failure Modes in S-2 Glass Laminates Under Ballistic Impact', 26th International SAMPE Conference, October 17-20, *1994*, pp. 657-668

Khetan R.P. and Chang D.C., 'Surface Damage of Sheet Molding Compound panels Subjected to Point Impact Loading', *Journal of Composite Materials,* Vol. 17, *1983,* pp. 182-194

Lee S-W.R. and Sun C.T., 'A Quasi-Static Penetration Model for Composite Laminates', *Journal of Composite Materials,* Vol. 27 (3), *1993a,* pp. 251-271

Lee S-W.R. and Sun C.T., 'Dynamic Penetration of Graphite/Epoxy Laminates by a Blunt Ended Projectile', *Composites Science and Technology,* Vol. 49, *1993b,* pp. 369-380

Newill J.F. and Vinson J.R., 'Some High Strain Rate Effects on Composite Materials', Proceedings of the Ninth International Conference on Composite Materials (ICCM IX), Madrid, Spain, Vol. 5, *1993,* pp. 269-277

Pierson M.O., 'Modelling the Impact Behaviour of Fiber Reinforced Composite Materials', *Master's Thesis, 1994,* The University of British Columbia

Press W.H., Flannery B.P., Teukolsky S.A. and Vetterling W.T., 'Numerical Recipes The Art of Scientific Computing (FORTRAN Version)', *1989,* Cambridge University Press

Ramesh K.T. and Kelkar N., 'Technique for the continuous measurement of projectile velocities in plate impact experiments', *Rev. Sci. Instrum.,* Vol. 66 (4), *1995,* pp. 3034-3036

Staab G.H. and Gilat A., 'High Strain Rate Characterization of Angle-Ply Glass/Epoxy Laminates', Proceedings of the Ninth International Conference on Composite Materials (ICCM IX), Madrid, Spain, Vol. 5, *1993,* pp. 278-285

Sun C.T. and Potti S.V., 'High Velocity Impact and Penetration of Composite Laminates', Proceedings of the Ninth International Conference on Composite Materials (ICCM IX), Madrid, Spain, Vol. 5, *1993,* pp. 261-268

Szymczak M., 'Evaluation of Polymeric Composites - A Preliminary Report', *Letter Report,* 3723E-P31WE (DREV 1641), *1994*

Timoshenko S.P., 'Vibration Problems in Engineering', Third Edition, *1955,* McGraw-Hill

Timoshenko S.P. and Woinowsky-Krieger S., 'Theory of Plates and Shells', Second Edition, *1959,* McGraw-Hill

Ursenbach D.O., 'Penetration of CFRP Laminates by Cylindrical Indenters', *Master's Thesis, 1995,* The University of British Columbia

Wu E., Sheen H-J., Chen Y-C., and Chang L-C., 'Penetration Force Measurements of Thin Plates by Laser Doppler Anemometry', *Experimental Mechanics,* Vol. 34 (2), *1994,* pp. 93-99

Zee R.H., Jang B.Z., Mount A. and Wang C.J., 'Microvelocity Sensor for Instantaneous Velocity Determination', *Rev. Sci. Instrum.,* Vol. 60 (12), *1989,* pp. 3692-3697

Appendix A

Laser Line Velocity Sensor (LLVS)

Laser Line Velocity Sensor (LLVS) is the name given to a group of components which enable the determination of a force-displacement curve for a ballistic event. The LLVS was developed by Ramesh and Kelkar [1995] at The Johns Hopkins University to continuously measure the impact velocity of flyer plates. The same system was implemented at UBC but was modified to enable the continuous measurement of the velocity during an impact event. The LLVS is made up of 4 components which will be dealt with individually. The components are hardware, calibration, software and LLVS data checks.

A.1 Hardware

Hardware refers to the physical components of the system and is made up of a diode laser, optics, detector and mounting equipment. The LLVS components are shown schematically in Figure A.1. The numbers on the components are described below and the dotted line represents the side view of the sheet.

A.1.1 Diode Laser

The diode laser (1 in Figure A.1) has a power output of 1 mW with a wavelength of 670 nm and is supplied by **Lasiris Inc.** (part number **SNF-501L-670-1-10**). With the use of special line generating optics patented by Lasiris Inc., a sheet of light which diverges in both the horizontal and vertical planes is obtained. The intensity of the light is not quite uniform across the width of the sheet and the edges have a slightly higher intensity than the middle of the sheet.

A.1.2 Optics

The first of two cylindrical lenses (2 in Figure A.1) is used to collimate the diverging sheet in the horizontal plane, resulting in a sheet of uniform width but diverging height. Due to the non-uniformity of the edges of the sheet a one inch aperture (3 in Figure A.1) is used to block the outside edges of the sheet. The sheet then passes through a neutral density filter (4 in Figure A.1) to reduce the intensity. Next the sheet passes through the second cylindrical lens (5 in Figure A.1) which collimates it in the vertical plane. There is now a sheet of laser light which is collimated in both the horizontal and vertical planes and has uniform intensity across the width.

The sheet is of fixed height and width. Lastly the sheet passes through a bi-convex lens (6 in Figure A.1) which focuses it to a point.

All the optics are supplied by **Melles Griot Canada Inc.**. The first cylindrical lens has part number **01LCP017** with corresponding lens holder **07LHC003**. The second cylindrical lens has part number **01LCP001** with corresponding lens holder **07LHC003**. The bi-convex lens has part number **01LDX171** with corresponding lens holder **07LHA002** and post **07RMS002**. The neutral density filter has part number **03FNG007** with the corresponding filter holder **07HFP002**.

A.1.3 Detection

The sheet is focused onto the active area of a photo-detector (7 in Figure A.1). The photo-detector has a saturation level of 1.5 V and hence the neutral density filter which is mentioned previously is used to reduce the intensity of the light. Without the neutral density filter the maximum voltage is 2.5 V. The photo-detector has a fast (7 ns) rise and fall time making lead and lag effects minimal. The photo-detector is supplied by **ThorLabs Inc.** and has part number **PDA150**.

A.1.4 Mounting Equipment

The LLVS requires a high degree of alignment in both the vertical and horizontal directions. The components of the system are aligned using an optical rail (8 in Figure A.1), rail carriers (9 in Figure A.1), post holders (10 in Figure A.1) and posts (11 in Figure A.1). The optical rail and rail carriers ensure alignment in the horizontal direction and the post holders and posts allow alignment in the vertical direction. To ensure that the sheet is perpendicular to the projectile direction the optical rail is attached to a clamp. This clamp attaches to the powder gun, as shown in Figure A.2, and allows movement in the projectile direction only. The LLVS can be mounted directly onto the powder gun since it is insensitive to rigid body motions.

The mounting equipment is once again supplied by **Melles Griot Canada Inc.**. The optical rail has part number **07ORN007**. The rail carrier has part number **07OCN501**. The post holder has part number **07PHS003**.

A.1.5 Oscilloscope

The oscilloscope is used to capture the output signal from the photo-detector. The oscilloscope used is a Tektronix 420 series and is an 8 bit 4 channel digital scope. The settings for a typical test are shown in

Table A.1.

A.1.6 Miscellaneous components

There are three other components that cannot be bought 'off the shelf' and have to be manufactured by a machine shop. These are the aperture, laser holder and post for the photo-detector. The drawing for the aperture is shown in Figure A.3, the laser holder in Figure A.4 and the post for the photo-detector in Figure A.5.

A.2 Calibration

The calibration is divided into two sections. The first section deals with the alignment of the components discussed in the previous section and the second section deals with the actual calibration relating voltages to displacements.

A.2.1 Alignment

The first component that is aligned is the diode laser (1 in Figure A.1). The diode laser controls the height of the sheet relative to the projectile. For conical projectiles this is important since the tip is pointed and needs to be aligned . Once the diode laser is aligned the bi-convex lens is put in to position (6 in Figure A.1). The centre of the lens is lined up with the laser. The first cylindrical lens (2 in Figure A.1) is then aligned. The height of this lens relative to the sheet is not critical but the distance between the diode laser and the lens must be set at the focal length of the lens to ensure that the light is collimated properly. If the distance is set incorrectly the sheet twists and is not horizontal. The aperture (3 in Figure A.1) and neutral density filter (4 in Figure A.1) are aligned next and since they block out and filter the light, respectively, the distance from the first lens is not critical. The second cylindrical lens (5 in Figure A.1) is aligned next. The centre of this lens must be aligned with the sheet or the sheet will not be horizontal. The photo-detector (7 in Figure A.1) is the last component to be aligned. This is done by moving the photo-detector forward until the sheet is visible on the surface of the photo-detector. The height of the photo-detector is then adjusted so that the sheet is centred on the active area of the photo-detector. The photo-detector is then moved back again until the sheet is focused to a point on the active area of the photo-detector. A schematic of the distances between the components are shown in Figure A.6.

A.2.2 Calibration

Due to the slight non-uniformity of the sheet intensity across the width it is necessary to have two calibrations. The first calibration, going into the sheet, represents the front of the projectile entering the sheet. The second calibration, going out of the sheet, represents the back of the projectile entering the sheet. The calibration is done using a digital micrometer with a piece of aluminium attached to block out the sheet. The set-up used during the calibration is shown in Figure A.7. When the micrometer is in position A in Figure A.7 the calibration into the sheet is performed, and when in position B in Figure A.7 the calibration out of the sheet is performed. The calibration is performed by blocking the sheet in increments of 0.5 mm and recording the

corresponding voltage. Once the calibration is completed the relationship between voltage and displacement is known.

One of the problems encountered from doing tests is that the maximum voltage is not always the same. The lexan sheets protecting the lenses may get dirty or even the laser itself may get dirty and thus the intensity of the sheet drops and the maximum voltage drops. It is therefore useful to have a normalised calibration so that if the maximum voltage does change, the calibration changes accordingly. Using the calibrations done to date (7 out of the sheet and 6 into the sheet) on the current set-up, a normalised calibration is obtained. The normalised calibration is done by subtracting the minimum value and then dividing by the new maximum value. This then gives a range from 0 to 1. The biggest error associated with the normalised calibration is 5% which translates to an error of 5% in displacement. It should be noted that if the set-up were to change, i.e. lens heights were adjusted or the aperture were changed, the calibration would have to be done again. The reason for this is that the current calibration is based on the slight non-uniformity across the width of the laser sheet as it is set-up now. If the set-up changes so too does the uniformity of the sheet which means the system would need re-calibrating.

A.3 Software

The software refers to the Data Acquisition Program (DAQ) and the Data Reduction Program (DRE). As their names suggest the DAQ acquires the data from the oscilloscope and the DRE reduces the data from voltages to displacements and eventually forces.

A.3.1 DAQ program

The DAQ program is a modification of one already in use that downloads waveforms from the oscilloscope and stores the values as digits. The digits range in value from -128 to 128. When the value reaches -128 it *'saturates'* and anything below a value of -128 has 256 digits added to it. The program was written in-house and the modifications are mainly to tailor the program to the LLVS settings. The modifications include entering more data about the test and a step converting digits to positive digits. The DAQ program stores digits as binary values and cannot return an integer, only whole numbers. Therefore the DAQ cannot return voltages but can return positive digits which are defined by

$$\text{Positive Digits} = \text{digit} + 128 + \text{position} * (\text{vertical digits / division}) \qquad \text{(A.1)}$$

for negative values of digits and

$$\text{Positive Digits} = (\text{digit} - 256) + 128 + \text{position} * (\text{vertical digits / division}) \qquad \text{(A.2)}$$

for positive values of digits. In equation (A.1) and (A.2) the position refers to the position of the zero point, in divisions, and the vertical digits per division is 25. Usually the position is subtracted but since it is a negative number (for the LLVS) the result is that it is added. Once the positive digits are calculated the DAQ program writes them with the other test variables to a data file.

A.3.2 DRE program

The DRE program is written in two parts using Visual Basic for EXCEL. The program uses subroutines and functions which will be explained below. A listing of the code is given in section A.4. Before the program is discussed it should be noted that the input file containing the raw data must have the test variables in the right cells. Table A.4 shows the layout from a typical raw data file.

The 1st row contains the user name, filename, time of the test, date of the test, material tested and thickness of the material tested (this is changed to number of layers in the case of fabrics). The 2nd row contains the width of the laser sheet (mm), distance between the sheet and the target (mm), voltage at full intensity, voltage at zero intensity and expected velocity. The 3rd row contains the volts per divisions, time scale (s/division), zero offset, trigger position (%) and trigger level (V). The 4th row contains the projectile hardness, projectile nose shape, projectile calibre (in.), projectile length (mm), projectile mass (g) and amount of powder (grains). The 5th to 5004th rows contain the test data.

A.3.2.1 Part 1 Sub *OpenFiles*

The program starts by prompting the user for the location of the raw data filename. The file is then opened and a second file *"voltage time.xls"* is also opened. This file is used for storing the voltages and times.

A.3.2.2 Part 1 Sub *ReadInValues*

The time scale, voltage per division and positive digits are read in from the data file. The positive digits are converted to voltages (*V*) using

$$V = Positive\ Digits * (V\ /\ digit) \tag{A.3}$$

where the volts per digit is given by

$$V\ /\ digit = \frac{V\ /\ division}{vertical\ digits\ /\ division} \tag{A.4}$$

and the vertical digits per division is once again 25.

A.3.2.3 Part 1 Sub *SetUpTime*

The time scale is converted into a time step between positive digits by dividing the time scale by the horizontal digits per division (50). The time array is then set up by adding the time step to the value before.

A.3.2.4 Part 1 Sub *WriteValues*

The times and voltages are then written to the "voltage time" spreadsheet and Part 1 of the module ends.

Before the second part of the program can be run the user needs to enter 6 numbers on the "voltage time" spreadsheet. Four of these are points in Figure A.8 and the other 2 are voltages. Points A, B, C and D in Figure A.8 correspond to the point at which the front of the projectile enters the laser sheet, the switch over point for the calibration, the point at which the back of the projectile enters the sheet and the point at which the back of the projectile leaves the sheet respectively. They are all in units of time. The voltages correspond to 100 % intensity (V_{full}) and 0 % intensity ($V_{blocked}$).

Once the values are entered Part 2 of the module is run.

A.3.2.5   Part 2 *CheckValues*

The module checks to make sure that the times and voltages have been entered correctly. If they haven't the module ends and instructs the user to check the data. When the values are correctly entered the sub-routine continue is run.

A.3.2.6   Part 2 Sub *PrintTimes*

The user is asked if a hardcopy of the times and voltages entered for the first part is needed.

A.3.2.7   Part 2 Sub *OpenFiles*

The *"current calibration.xls"* and *"data file.xls"* files are opened. *"data file.xls"* is the file which all the final data is written to and *"current calibration.xls"* contains the calibration values for the look-up table.

A.3.2.8   Part 2 Sub *ReadInVariables*

This sub-routine reads in all the test variables from the raw data file.

A.3.2.9   Part 2 Sub *ReadInValues*

The voltages, times and 6 values entered by the user are read in from *"voltage time.xls"*. The calibration values are read in from *"current calibration.xls"*.

A.3.2.10   Part 2 Sub *LLVSChecks*

This sub-routine calculates the checks which can be performed on the LLVS to make sure it is working properly. These checks are described in more detail on page 122.

A.3.2.11   Part 2 Sub *FindPoints*

Points A, B, C and D which are entered by the user are in units of time. These are converted into points on the curve (i.e. a time of 20 μs might correspond to point 500) and stored for later use.

A.3.2.12   Part 2 Sub *PreventOverflow*

If there is a point in the data set which is above the maximum calibration voltage or below the minimum calibration voltage the program crashes due to an overflow. Therefore it is necessary to prevent this by making values above the maximum equal to the maximum, and values below

the minimum equal to the minimum. The values are normally 7mV above the maximum or below the minimum.

A.3.2.13 Part 2 Sub **CalculateDisplacements**

The first calculation that is performed on the voltage is one converting it into a displacement. A function has been written that has a voltage and a point for the input, and outputs a displacement. The point is used to determine which side of point B in Figure A.8 the voltage is. If the point is before point B the calibration into the sheet is used and if the point is at or after point B the calibration out of the sheet is used. The voltage is converted to a displacement using a look up table and a typical displacement time curve is shown in Figure A.9.

A.3.2.14 Part 2 Sub **InitialV**

The striking velocity is calculated between points X and Y in Figure A.9. The velocity, v , is calculated from

$$v = \frac{\Delta s}{\Delta t} \tag{A.5}$$

which is simply the slope of the displacement time curve.

A.3.2.15 Part 2 Sub **ReduceData**

The data set at this stage of the program has 5000 data points. The point of impact is defined as

$$P_{impact} = w_{ls} + d_{ts} - l_{projectile} \tag{A.6}$$

where w_{ls} is the width of the laser sheet ,d_{ts} is the distance of the target from the sheet and $l_{projectile}$ is the projectile length (see Figure A.10). Therefore the 'useful' data or 'impact data' occurs once the back of the projectile enters the sheet. So the data is reduced to include only the impact data which is only the data between points C and D in Figure A.9. If the projectile is shorter than the sheet the point of impact is assumed to be at point C in Figure A.9. The final displacement data set includes only data from point C to D in Figure A.9 that has been zeroed to point C, and then zeroed to the point of impact. A sample output is shown in Figure A.11. Zero on the final displacement time curves refers to the point of impact

Figure A.11 also provides a check for the width of the laser sheet. The width of the laser, w_{ls}, sheet can be computed from

$$w_{ls} = l_{remaining} + d_{max} - d_{min} \tag{A.7}$$

where $l_{remaining}$ is the length of the projectile left in the sheet and d_{min} and d_{max} refer to points A and B in Figure A.11 respectively. It should be noted that equation (A.7) calculates the width of the laser sheet if the projectile is longer than the sheet but calculates the length of the projectile if the projectile is shorter than the sheet.

A.3.2.16 Part 2 Sub **Velocities**

Once the data is reduced the velocities can be calculated. Once again these are computed using equation (A.5) which is the slope of the displacement time curve. A second function was written which has displacement and time as the input and returns the slope (velocity) of a straight line fitted to the data set. The number of data points in each velocity calculation is determined by the time range. The time range is the Δt in equation (A.5) and the program prompts the user for a value. If no value is entered, the time range defaults to 28 µs. The number of data points is always an odd number so that the slope can be calculated at the midpoint of the data points. If the number of data points is an even number the program rounds it up to the next highest odd number.

The beginning and end of the record do not contain enough data for a time range of 28 µs. The program recognises when it is at the beginning or end of the data set and adjusts the number of points in the velocity calculation based on an input from the user. Once again if no value is entered the program uses a default value.

A.3.2.17 Part 2 Sub **AccelerationsForces**

The final calculation in the program is to calculate acceleration and ultimately force. The slope function is used once again for this calculation since

$$a = \frac{\Delta v}{\Delta t} \qquad (A.8)$$

which is the slope of a velocity time curve. So the inputs for the slope function are velocity and time and the output is acceleration. The acceleration is multiplied by the projectile mass and a scaling factor to get compatible units and the end result is a force. The force is computed as a compressive force.

A.3.2.18 Part 2 Sub **Energies**

This sub-routine calculates the energies and zeroes the displacement to a zero force.

A.3.2.19 Part 2 Sub **WriteValues**

The test variables, times, displacements, velocities, accelerations, forces and energies are all written to *"data file.xls"*. If the material is a hard armour the 'Areal Density' column is removed and the '# layers' cell is changed to thickness with the units in mm.

A.3.2.20 Part 2 Sub **CloseFiles**

The program ends by closing the calibration file. It leaves all the other files open in case the user wants to run the second part again with slightly different values for point A, B ,C and D.

A.4 Data Reduction (DRE) Code

A.4.1 Part 1

```
'First part of a two part module
'This module reads in digits from the raw-data file and converts to voltages
'The user then inputs further information which is used in the second part of the module

Const WriteFileName = "voltage time.xls"

Const NoOfPoints = 5000

Dim Voltage(NoOfPoints), DataTime(NoOfPoints)
Dim DataFileName
Dim VoltDiv, TimeDiv

Sub Main()
    OpenFiles
    ReadInValues
    SetUpTime
    WriteValues
End Sub

Sub OpenFiles()                          'opens files
    ChDir "\\perseus\users\"
    Do
        DataFileName = Application.GetOpenFilename
    Loop Until DataFileName <> False
    Workbooks.OpenText Filename:=DataFileName, _
        Origin:=xlWindows, StartRow:=1, DataType:=xlDelimited, _
        TextQualifier:=xlDoubleQuote, ConsecutiveDelimiter:=False, Tab _
        :=True, Semicolon:=False, Comma:=False, Space:=False, Other _
        :=True, OtherChar:=",", FieldInfo:=Array(Array(1, 1), Array(2, 1), _
        Array(3, 1), Array(4, 1), Array(5, 1), Array(6, 1))      'opens data file as delimited using comma
    DataFileName = Application.ActiveSheet.Name & ".wav"
    Workbooks.Open Filename:="\\Frosty\d\Archive\Impact\LLVS\Data Reduction\" & WriteFileName
End Sub

Sub ReadInValues()                       'reads in values from data file
    Windows(DataFileName).Activate
    TimeDiv = Range("B3").Value                  'reads in time division
    VoltDiv = Range("A3").Value                  'reads in voltage division
    For i = 1 To NoOfPoints
        SelectedRange = "A" & i + 4
        Voltage(i) = Range(SelectedRange).Value * VoltDiv / 25      'converts digits into voltages
    Next i
End Sub

Sub SetUpTime()                          'sets up time array
    DataTime(1) = 0
    For i = 1 To NoOfPoints - 1
        DataTime(i + 1) = DataTime(i) + TimeDiv / 50 * 1000000
    Next i
End Sub

Sub WriteValues()                        'writes values to file
    Windows(WriteFileName).Activate
    Sheets("Data").Select
    For i = 1 To NoOfPoints
        SelectedRange2 = "A" & i + 3
        SelectedRange3 = "B" & i + 3
        Range(SelectedRange2).Value = DataTime(i)
        Range(SelectedRange3).Value = Voltage(i)
    Next i
    Range("C2").Value = DataFileName
End Sub
```

A.4.2 Part 2

```
'Second part of a two part module
'This module converts voltages to displacements, velocities and forces using a look-up table from the calibration

Const NoOfVoltages = 5000                'number of voltages
Const NoOfCaliPoints = 52                'no of calibration points

Const WriteFileName = "data file.xls"
Const CaliFileName = "current calibration.xls"
Const VoltageFileName = "voltage time.xls"

Dim ValueIn(NoOfCaliPoints, 3), ValueOut(NoOfCaliPoints, 3), ValueDisplacement(NoOfCaliPoints, 3)
Dim DataTime(NoOfVoltages), Voltage(NoOfVoltages)
Dim Displacement(NoOfVoltages), Velocity(NoOfVoltages), Acceleration(NoOfVoltages)
Dim Force(NoOfVoltages), Energy(NoOfVoltages)
Dim InitialVelocity
Dim CaliVoltageHi, CaliVoltageLow, CaliVoltageMax, CaliVoltageMin
Dim CaliVoltageIn(NoOfCaliPoints), CaliVoltageOut(NoOfCaliPoints), CaliDisplacement(NoOfCaliPoints)
Dim MinDisplacement
Dim TimeA, TimeB, TimeC, TimeD, PointA, PointB, PointC, PointD, PointOfImpact, NoOfImpactPoints
Dim BlockedVoltage, FullVoltage
Dim DataFileName
Dim UserName, File, TestTime, TestDate, Material, MatThick, ArealDensity
Dim Wid, Distance, MaxV, MinV, ExpVel, VoltDiv, TimeDiv, Offset, TrigPos
Dim TrigLev, ProjType, ProjNose, ProjCal, ProjLength, ProjMass, Powder
Dim StartPoint(NoOfVoltages), FinishPoint(NoOfVoltages), X(NoOfVoltages), Y(NoOfVoltages)
Dim DataRange, FirstVelRange, LastVelRange, NoOfVelocityPoints
Dim FirstVelPoint, LastVelPoint, FirstAccPoint, LastAccPoint, m
Dim IVelocity, NullVelocity, CalcLength
Dim Result

Sub Main()
    CheckValues
    If Result = 1 Then
        Continue
    Else temp = MsgBox("You have entered the data incorrectly." & _
    " Please check and run the second half of this module again.", vbExclamation)
    End If
End Sub

Sub CheckValues()                        'reads in values from first part
    Result = 0
    TimeA = 0
    TimeB = 0
    TimeC = 0
    TimeD = 0
    BlockedVoltage = 0
    FullVoltage = 0
    Windows(VoltageFileName).Activate
    Sheets("Data").Select
    TimeA = Range("E7").Value
    TimeB = Range("F7").Value
    TimeC = Range("G7").Value
    TimeD = Range("H7").Value
    BlockedVoltage = Range("E11").Value
    FullVoltage = Range("F11").Value
    If TimeA < TimeB And TimeB <= TimeC And TimeC < TimeD And _
    TimeA <> "" And TimeB <> "" And TimeC <> "" And TimeD <> "" And _
    BlockedVoltage < FullVoltage And BlockedVoltage <> "" And FullVoltage <> "" Then 'checks all values are entered
        Result = 1
    End If
End Sub

Sub Continue()
    PrintTimes
    OpenFiles
```

```
        ReadInVariables
        ReadInValues
        FindPoints
        LLVSChecks
        PreventOverflow
        CalculateDisplacements
        InitialV
        ReduceData
        Velocities
        AccelerationsForces
        Energies
        CalcOff
        WriteValues
        CloseFiles
        CalcOn
End Sub

Sub PrintTimes()                            'prints the times from the first part of the module
    Response = MsgBox("Do you want a print out of the times from part A?", vbYesNo)
    If Response = 6 Then
        Windows(VoltageFileName).Activate
        Sheets("Data").Select
        Columns("C:C").EntireColumn.AutoFit
        Range("C1:H11").Select
        Selection.PrintOut Copies:=1
        With Toolbars(8)
           .Left = 720
           .Top = 80
        End With
    End If
End Sub

Sub OpenFiles()                             'opens the necessary files
    Windows(VoltageFileName).Activate
    Sheets("Data").Select
    DataFileName = Range("C2").Value
    Workbooks.Open Filename:="\\Frosty\d\Archive\Impact\LLVS\Calibration\" & CaliFileName
    Workbooks.Open Filename:="\\Frosty\d\Archive\Impact\LLVS\Data Reduction\" & WriteFileName
End Sub

Sub ReadInVariables()                       'reads in test variables
    Windows(DataFileName).Activate
    UserName = Range("A1").Value
    File = Range("B1").Value
    TestTime = Range("C1").Value
    TestDate = Range("D1").Value
    Material = Range("E1").Value
    MatThick = Range("F1").Value
    ArealDensity = Range("G1").Value
    Wid = Range("A2").Value
    Distance = Range("B2").Value
    MaxV = Range("C2").Value
    MinV = Range("D2").Value
    ExpVel = Range("E2").Value
    VoltDiv = Range("A3").Value
    TimeDiv = Range("B3").Value
    Offset = Range("C3").Value
    TrigPos = Range("D3").Value
    TrigLev = Range("E3").Value
    ProjType = Range("A4").Value
    ProjNose = Range("B4").Value
    ProjCal = Range("C4").Value
    ProjLength = Range("D4").Value
    ProjMass = Range("E4").Value
    Powder = Range("F4").Value
End Sub

Sub ReadInValues()                          'reads in values from data file
```

```
    Windows(VoltageFileName).Activate
    Sheets("Data").Select
    For i = 1 To NoOfVoltages
        SelectedRange = "A" & i + 3
        SelectedRange2 = "B" & i + 3
        DataTime(i) = Range(SelectedRange).Value        'time
        Voltage(i) = Range(SelectedRange2).Value        'voltage
    Next i
    Windows(CaliFileName).Activate
    Sheets("Data").Select
    For j = 1 To NoOfCaliPoints
        For k = 1 To 3
            If k = 1 Then SelectedColumn = "A"        'selects calibration out voltage
            If k = 2 Then SelectedColumn = "B"        'selects calibration in voltage
            If k = 3 Then SelectedColumn = "C"        'selects calibration displacement
            SelectedRange2 = SelectedColumn & j + 7
            ValueDisplacement(j, k) = Range(SelectedRange2).Value
            ValueOut(j, k) = Range(SelectedRange2).Value
            ValueIn(j, k) = Range(SelectedRange2).Value
        Next k
        CaliDisplacement(j) = ValueDisplacement(j, 1)   'array containing calibration displacements
        CaliVoltageOut(j) = ValueOut(j, 2) * (FullVoltage - BlockedVoltage) + BlockedVoltage 'converts normalised value
        CaliVoltageIn(j) = ValueIn(j, 3) * (FullVoltage - BlockedVoltage) + BlockedVoltage   'to voltages
    Next j
    CaliVoltageMin = CaliVoltageIn(1)
    CaliVoltageMax = CaliVoltageIn(NoOfCaliPoints)
End Sub

Sub FindPoints()                          'finds the points corresponding to the input from the user
    i = 1
    Do Until DataTime(i) > TimeA
        i = i + 1
    Loop
    PointA = i
    Do Until DataTime(i) > TimeB
        i = i + 1
    Loop
    PointB = i
    Do Until DataTime(i) > TimeC
        i = i + 1
    Loop
    PointC = i
    Do Until DataTime(i) > TimeD - 0.1
        i = i + 1
    Loop
    PointD = i
End Sub

Sub LLVSChecks()                          'calculates LLVS checks
    NullTime = TimeC - TimeB
    NullDisplacement = ProjLength - Wid
    If NullDisplacement < 0 Then
        NullDisplacement = -NullDisplacement
    End If
    NullVelocity = NullDisplacement / NullTime * 1000
    InitialTime = TimeB - TimeA
    If ProjLength < 25.4 Then InitialDisplacement = ProjLength Else _
    InitialDisplacement = Wid
    IVelocity = InitialDisplacement / InitialTime * 1000
    If ProjLength < 25.4 Then
        CalcLength = Wid * (Voltage(PointA) - Voltage(PointB)) / (FullVoltage - BlockedVoltage)
    Else
        CalcLength = Wid * (Voltage(PointA) - Voltage(PointB)) / (FullVoltage - BlockedVoltage) + IVelocity * NullTime / 1000
    End If
End Sub

Sub PreventOverflow()                     'prevents overflow in the program
    For i = 1 To NoOfVoltages
```

```
        If Voltage(i) > CaliVoltageMax Then Voltage(i) = CaliVoltageMax Else Voltage(i) = Voltage(i)
        If Voltage(i) < CaliVoltageMin Then Voltage(i) = CaliVoltageMin Else Voltage(i) = Voltage(i)
    Next i
End Sub


Sub CalculateDisplacements()                    'calculates the displacements
    For i = 1 To NoOfVoltages
        Volt = Voltage(i)
        Displacement(i) = CalcDisplacement(Volt, i)    'function that uses the look up table to calculate displacements
    Next i
    MinDisplacement = Displacement(PointC)          'finds the minimum displacement
End Sub


Sub InitialV()                    'calculates the initial velocity                    'finds points of interest on curve
    i = 1
    Do Until Displacement(i) < 24                'first point for initial velocity
        i = i + 1
    Loop
    PointX = i
    Do Until Displacement(i) < Displacement(PointB) + 1 'second point for initial velocity
        i = i + 1
    Loop
    PointY = i
    For i = PointX To PointY                'assigns x and y values for slope function
        X(i) = DataTime(i)
        Y(i) = Displacement(i)
    Next i
    InitialVelocity = Slope(PointX, PointY) * 1000      'calculates initial velocity
    InitialVelocity = -InitialVelocity
End Sub


Sub ReduceData()                    'reduces data to only the displacements of interest
    NoOfImpactPoints = PointD - PointC + 1          'number of impact points
    If ProjLength < 25.4 Or Wid = 0 Or Distance = 0 _
    Then PointOfImpact = Displacement(PointC) Else _
    PointOfImpact = Wid - (ProjLength - Distance)       'if projectile is shorter than sheet point of impact becomes point B
    w = PointC - 1
    For i = 1 To NoOfImpactPoints
        Displacement(i) = Displacement(i + w) - PointOfImpact - MinDisplacement 'zeroes the displacement
    Next i                                  'to the point of impact
End Sub


Sub Velocities()                    'calclates the velocities
    MaxRange = DataTime(NoOfVoltages) - DataTime(1)
    ReadInDisplacements                 'assigns y values to displacement and x values to time
    If TimeDiv = 0.000001 Then              'sets default value based on time scale
        TimeRange = 3
    ElseIf TimeDiv = 0.000002 Then
        TimeRange = 6
    ElseIf TimeDiv = 0.000005 Then
        TimeRange = 30
    ElseIf TimeDiv = 0.00001 Then
        TimeRange = 30
    End If
    Response = MsgBox("The range of time for the velocity calculation has been set to " _
    & TimeRange & " us.  Do you want to change it?", vbYesNo)
    If Response = 6 Then
    TimeRange = MaxRange + 1
        Do Until TimeRange < MaxRange
            Do
                TimeRange = Application.InputBox("New time range for the velocity calculation?", "Time Range", Type:=1)
            Loop Until TimeRange <> False
            If TimeRange >= MaxRange Then
                t = MsgBox("The value you input is too high.  Enter a value below " & MaxRange, vbCritical)
            End If
        Loop
    End If
    i = 1
```

```
      Do Until DataTime(i) > TimeRange
         i = i + 1
      Loop
      DataRange = Odd(i)
      FirstVelRange = (DataRange + 1) / 2
      FirstPoint = (Odd(FirstVelRange) + 1) / 2
      Response = MsgBox("The first point for taking the slope has been set to the " _
      & FirstPoint & " point.  Do you want to change it?", vbYesNo)
      If Response = 6 Then
         FirstPoint = FirstVelRange + 1
         Do Until FirstPoint < FirstVelRange
            Do
               FirstPoint = Application.InputBox("New first point for the slope calculation?", "First Point", Type:=1)
            Loop Until FirstPoint <> False
            If FirstPoint >= FirstVelRange Then
               t = MsgBox("The value you input is too high.  Enter a value below " & FirstVelRange, vbCritical)
            End If
         Loop
      End If
      FirstVelPoint = (Odd(FirstPoint) + 1) / 2        'sets up first point for velocity reading
      LastVelPoint = NoOfImpactPoints - FirstVelPoint + 1 'sets up last point for velocity reading
      If FirstVelPoint > FirstVelRange Then
         FirstVelPoint = FirstVelRange
      End If
      LastVelRange = (NoOfImpactPoints + (NoOfImpactPoints - (DataRange - 1))) / 2 'sets up point for last range of values
      m = FirstVelRange - 1
      i = FirstVelPoint
      Do While i <= LastVelPoint                    'takes fewer readings at the beginning
         If i < FirstVelRange Then
            BeginPoint = 1                    'first value of range
            EndPoint = 2 * i - 1              'last value of range
         ElseIf i > LastVelRange Then               'takes fewer readings at the end
            BeginPoint = 2 * i - NoOfImpactPoints
            EndPoint = NoOfImpactPoints
         Else
            BeginPoint = i - m
            EndPoint = i - m + (DataRange - 1)
         End If
         Velocity(i) = Slope(BeginPoint, EndPoint) * 1000    'function slope calculates the slppe of set of points with
         i = i + 1                          'range EndPoint-BeginPoint
      Loop
      NoOfVelocityPoints = i
End Sub

Sub AccelerationsForces()                    'calclates forces and accelerations
      ReadInVelocities
      m = FirstVelRange - 1
      FirstAccRange = FirstVelPoint + m               'first point for full range of velocities
      LastAccRange = LastVelPoint - m
      FirstAccPoint = FirstVelPoint + (FirstVelPoint - 1) 'sets up first
      LastAccPoint = LastVelPoint - (FirstVelPoint - 1)   'and last acceleration points
      i = FirstAccPoint
      If i > FirstAccRange Then i = FirstAccRange Else i = i
      Do While i <= LastAccPoint
         If i < FirstAccRange Then
            BeginPoint = FirstVelPoint
            EndPoint = 2 * i - FirstVelPoint
         ElseIf i > LastAccRange Then
            BeginPoint = 2 * i - (NoOfVelocityPoints - 1)
            EndPoint = LastVelPoint
         Else
            BeginPoint = i - m                    'first value of range
            EndPoint = i - m + (DataRange - 1)         'last value of range
         End If
         Acceleration(i) = Slope(BeginPoint, EndPoint) * 1000000
         Force(i) = -ProjMass / 1000 * Acceleration(i)   'compressive force
         i = i + 1
      Loop
```

```
End Sub

Sub Energies()                        'calculates energies and zeroes the force to begin a zero
   i = FirstAccPoint                  'displacement
   Do Until Force(i) > 0
      i = i + 1
   Loop
   If i = FirstAccPoint Then FirstForcePoint = i Else FirstForcePoint = i - 1
   Offsett = Displacement(FirstForcePoint)
   Energy(FirstForcePoint) = 0
   For i = FirstForcePoint To LastAccPoint - 1
      Energy(i + 1) = Force(i + 1) * (Displacement(i + 1) - Displacement(i)) / 1000 + Energy(i)
   Next i
   For i = 1 To NoOfImpactPoints
      Displacement(i) = Displacement(i) - Offsett
   Next i
End Sub

Sub CalcOff()                         'switches calculation to manual
   Windows(WriteFileName).Activate
   Application.Calculation = xlManual
End Sub

Sub WriteValues()                     'writes values to file
   If Material = "S2 GLASS" Or Material = "s2 glass" Then
      Windows(WriteFileName).Activate
      Sheets("Data").Select
      Thickness
   End If
   Windows(WriteFileName).Activate
   Sheets("Data").Select
   Range("A3").Value = UserName
   Range("B3").Value = File
   Range("C3").Value = TestTime
   Range("D3").Value = TestDate
   Range("E3").Value = Material
   Range("F3").Value = MatThick
   Range("G3").Value = ArealDensity
   Range("A11").Value = Wid
   Range("B11").Value = Distance
   Range("C11").Value = MaxV
   Range("D11").Value = MinV
   Range("E11").Value = InitialVelocity
   Range("A15").Value = VoltDiv
   Range("B15").Value = TimeDiv
   Range("C15").Value = Offset
   Range("D15").Value = TrigPos
   Range("E15").Value = TrigLev
   Range("A7").Value = ProjType
   Range("B7").Value = ProjNose
   Range("C7").Value = ProjCal
   Range("D7").Value = ProjLength
   Range("E7").Value = ProjMass
   Range("F7").Value = Powder
   Range("C3").Select
   Selection.NumberFormat = "h:mm"
   For i = 1 To NoOfImpactPoints
      SelectedRange3 = "A" & i + 20
      SelectedRange4 = "B" & i + 20
      SelectedRange5 = "C" & i + 20
      SelectedRange6 = "D" & i + 20
      SelectedRange7 = "E" & i + 20
      SelectedRange8 = "F" & i + 20
      Range(SelectedRange3).Value = DataTime(i)
      Range(SelectedRange4).Value = Displacement(i)
      Range(SelectedRange5).Value = Velocity(i)
      Range(SelectedRange6).Value = Acceleration(i)
      Range(SelectedRange7).Value = Force(i)
```

```
        Range(SelectedRange8).Value = Energy(i)
    Next i
    Sheets("llvs data checks").Select
    Range("B3").Value = ExpVel
    Range("B6").Value = NullVelocity
    Range("B9").Value = IVelocity
    Range("B12").Value = CalcLength
End Sub


Sub CloseFiles()                        'closes calibration file
    Windows(CaliFileName).Activate
    ActiveWindow.Close
End Sub


Sub CalcOn()                            'switches calculation to automatic
    Windows("data file.xls").Activate
    Application.Calculation = xlAutomatic
End Sub


Sub ReadInDisplacements()               'assigns x and y values
    For i = 1 To NoOfVoltages
        X(i) = DataTime(i)
        Y(i) = Displacement(i)
    Next i
End Sub


Sub ReadInVelocities()                  'assigns x and y values
    For i = 1 To NoOfImpactPoints
        X(i) = DataTime(i)
        Y(i) = Velocity(i)
    Next i
End Sub


Sub Thickness()                         'deletes extra column if material is hard
    Columns("G:G").Select
    Selection.Delete Shift:=xlToLeft
    Range("F1:F16").Select
    With Selection.Borders(xlRight)
        .Weight = xlMedium
        .ColorIndex = xlAutomatic
    End With
    Selection.BorderAround LineStyle:=xlNone
    Range("F1").Select
    ActiveCell.FormulaR1C1 = "Thickness"
    Range("F2").Select
    ActiveCell.FormulaR1C1 = "mm"
End Sub


Function CalcDisplacement(Vactual, point)       'function that reads in a voltage and assigns a displacement to
    For m = 1 To NoOfCaliPoints - 1             'the voltage
        If point < PointA Then                  'if the voltage is going into the sheet use calibration in
            CaliVoltageLow = CaliVoltageIn(m)
            CaliVoltageHi = CaliVoltageIn(m + 1)
        Else
            CaliVoltageLow = CaliVoltageOut(m)          'else use calibration out
            CaliVoltageHi = CaliVoltageOut(m + 1)
        End If
        If Vactual < CaliVoltageHi And Vactual >= CaliVoltageLow Then
            Vhi = CaliVoltageHi
            Vlow = CaliVoltageLow
            Dhi = CaliDisplacement(m + 1)
            Dlow = CaliDisplacement(m)
        End If
        If Vactual = CaliVoltageHi Then
            Vhi = CaliVoltageHi
            Vlow = CaliVoltageLow
            Dhi = CaliDisplacement(NoOfCaliPoints)
            Dlow = CaliDisplacement(NoOfCaliPoints - 1)
```

```
    End If
  Next m
  CalcDisplacement = Dlow + (Dhi - Dlow) * (Vactual - Vlow) / (Vhi - Vlow)
End Function

Function Slope(Start, Finish)          'function to fit a least squares
  SumX = 0                             'curve to data
  SumY = 0
  Sum = 0
  Slope = 0
  Eror = 0
  SumErorSquared = 0
  For j = Start To Finish
    SumX = SumX + X(j)                 'sums the x values
    SumY = SumY + Y(j)                 'sums the y values
  Next j
  Sum = Finish - Start + 1             'assumes equal weighting on
  Sigma = SumX / Sum                   'each value
  For k = Start To Finish
    Eror = X(k) - Sigma
    SumErorSquared = SumErorSquared + Eror * Eror   'sums the square of the errors
    Slope = Slope + Eror * Y(k)
  Next k
  Slope = Slope / SumErorSquared          'gives the slope and
  Intercept = (SumY - SumX * Slope) / Sum       'intercept of the data
End Function

Function Odd(number)                    'rounds even numbers up to next highest odd number and odd numbers
  For i = 1 To number + 1 Step 2
    If i <= number Then Odd = number Else Odd = number + 1   'remain the same
  Next i
End Function
```

A.5 LLVS Data Checks

As mentioned before there are 4 checks that are performed to ensure the laser is working properly. The program calculates them automatically and writes them to the spreadsheet.

A.5.1 Null Period

The striking velocity, v_s, of the projectile can be calculated from

$$v_s = \left| \frac{w_{ls} - l_{projectile}}{t_{null}} \right| \tag{A.9}$$

where w_{ls} is the width of the laser sheet, $l_{projectile}$ is the length of the projectile and t_{null} is the duration of the null period (units in m and s respectively).

A.5.2 Initial Velocity

The striking velocity of the projectile can also be computed from

$$v_s = \frac{w_{ls}}{V_A - V_B} * l_{projectile} \tag{A.10}$$

where V_A and V_B are the voltages at point A and B in Figure A.8. For a projectile that is longer than the width of the laser sheet $l_{projectile}$ is simply equal to the width of the laser sheet.

A.5.3 v_s and v_r

The ratio between v_s and v_r will ideally be 1 when there is no target or the target fails to slow the projectile down, and will be less than 1 when the target is successful in slowing the projectile down.

A.5.4 Length of Projectile

The final check is that of the length of the projectile, $l_{projectile}$. This can be calculated from

$$l_{projectile} = \frac{w_{ls}}{V_{full} - V_{blocked}} * (V_A - V_B) + v_s * \frac{t_{null}}{1000} \qquad (A.11)$$

where V_{full} is the voltage at 100 % intensity, $V_{blocked}$ is the voltage at 0 % intensity and V_A and V_B are the voltages at points A and B in Figure A.8. For a projectile that is shorter than the sheet equation (A.11) reduces to

$$l_{projectile} = \frac{w_{ls}}{V_{full} - V_{blocked}} * (V_A - V_B) \qquad (A.12)$$

For the curve shown in Figure A.8 the checks were done and the results are shown in Table A.2. The curve satisfies all the checks for the test which shows the LLVS was working properly for the test.

In general the LLVS checks work well and show that the system is working. There are, however, occasions where the agreement between the checks and the test have not been very good. Upon closer inspection it was found that the times these checks failed corresponded to either low velocities or very high velocities. At both these extremes of velocity the projectiles become unstable and yawed quite a bit. The reason the projectiles yawed at low velocities is most probably due to their weight and size. At higher velocities the problem is due to the gun powder used. The current gun powder is very volatile and burns very fast creating a mini explosion rather than a controlled release of the energy. It should be noted that these problems are not a LLVS problem but rather a problem of the set-up, i.e. the projectiles need to be redesigned and a new gun powder used into that is less volatile.

A second time the check fails is with projectiles that are smaller than the sheet. The LLVS checks show good agreement for the slope calculation and the initial velocity but the velocity calculated from the null period is always higher than the other two calculations. This is most likely due to the fact that the LLVS has not been calibrated for the smaller projectiles and the null period uses the out calibration curve which could introduce error into the velocity.

Table A.1. Typical oscilloscope settings for an impact test.

Vertical menu		Horizontal menu		Trigger menu		Acquire menu
Coupling	*DC*	Time Base	*Main*	Type	*Edge*	*Single Acq. Seq.*
Bandwidth	*20 MHz*	Trigger Position	*10%*	Source	*CH1*	
Fine scale	*200 mV/div*	Record Length	*5000*	Coupling	*DC*	
Position	*-3.50 div*	Horizontal scale	*5 μ s/div*	Slope	⎺⎽	
Offset	*0 V*			Level	*1.2 V*	
				Mode & Holdoff	*Normal*	

Table A.2. Table of results from 4 checks performed on LLVS.

	Null Period	Initial Slope	Ratio	Projectile Length
	m/s	m/s	vs/vr	mm
Actual	*211.0*	*211.0*	*<1*	*46.1*
Check	209.1	211.7	<1	46.3

Table A.3. Part numbers for the LLVS.

Supplier	Item	Quantity	Part #	# in Figure A.1	Description
Melles Griot Canada Inc.	Optical Rail	1	07ORN007	8	1m long 50 mm wide
	Rail Carriers	6	07OCN501	9	25 mm long 50 mm wide
	Post Holders	6	07PHS003	10	12 mm bore 50 mm height
	Lens Holder	2	07LHC003		Cylindrical lens holder
	Adj. Lens Holder	1	07LHA002		Adjustable lens holder
	Post	1	07RMS002		12 mm diameter L=60 mm M6 thread
	Cylindrical lens	1	01LCO001	5	F=40 mm 60x15 mm
	Cylindrical lens	1	01LCP017	2	F=250 mm 60x50 mm
	Bi-convex lens	1	01LDX171	6	F=100 mm D=50 mm
	Filter Holder	1	07HFP002		
	Filter	1	03FNG007	4	Neutral density filter
Lasiris Inc.	Laser	1	SNF-501L-670-1-10	1	
Thorlabs Inc.	Photo-detector	1	PDA150	7	

Table A.4. Layout for a typical raw data file.

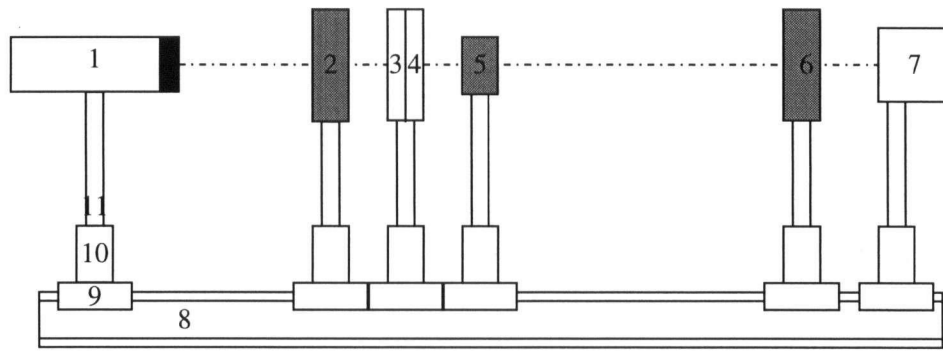|	A	B	C	D	E	F
1	tim	b03063	10:36:45	6/3/97	s2 glass	6.35
2	25.4	20	1.452	0.056	175	
3	0.2	0.000005	3.5	10	1.2	
4	rc30	120 deg.	0.3	40	13.2	3.5
5	183					
6	183					
7	183					
8	182					
9	183					
10	183					
11	183					
12	183					
13	182					
14	183					
15	183					
16	183					

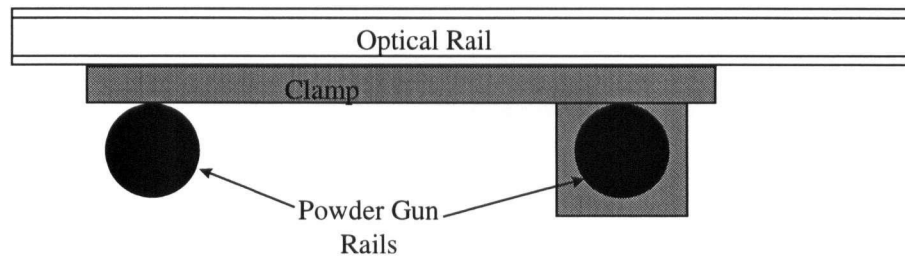Figure A.1. Schematic showing LLVS components (see also Table A.3).

Figure A.2. Schematic showing the clamp connecting the optical rail to the powder gun (side view).
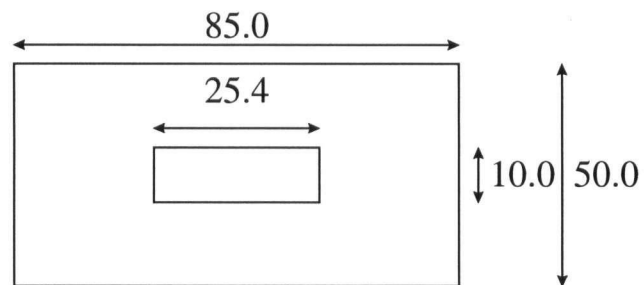

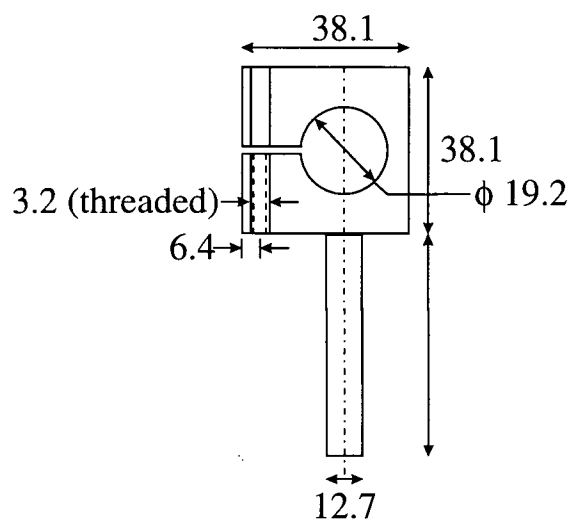Figure A.3. Drawing for the aperture (all dimensions in mm).

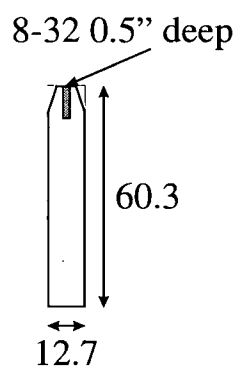Figure A.4. Drawing for the laser holder (all dimensions in mm).

Figure A.5. Drawing fo the photo-detector post (all dimensions in mm).

Figure A.6. Schematic showing distances (in mm) between the centres of the system components (top view).
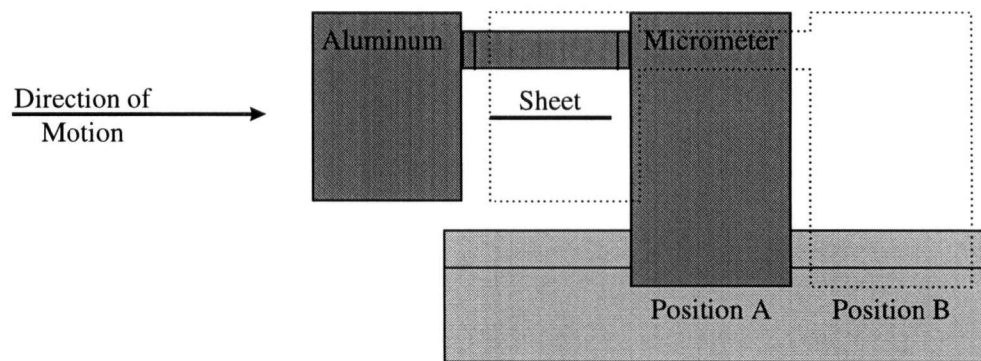
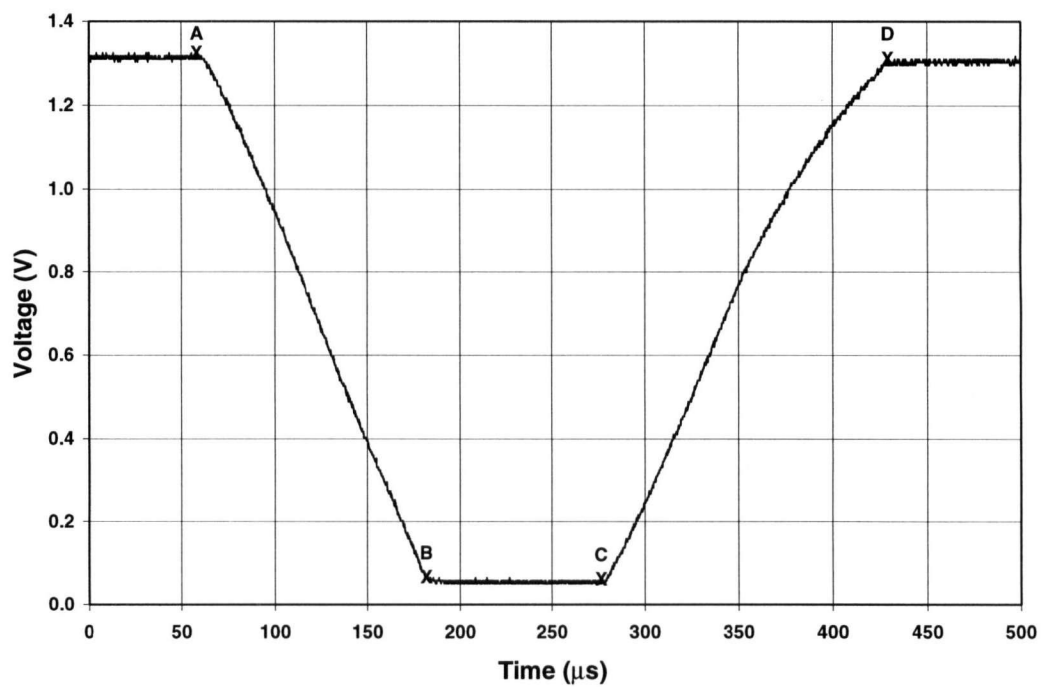Figure A.7. Schematic showing the position of the micrometer used in the calibration.

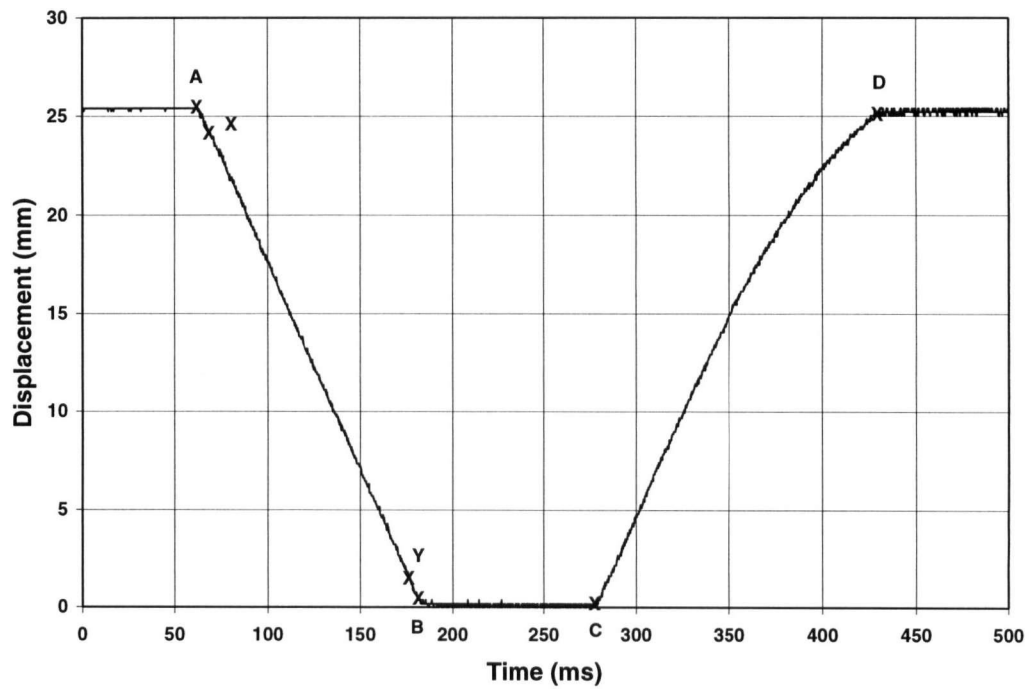Figure A.8. Sample output from the first part of the DRE.

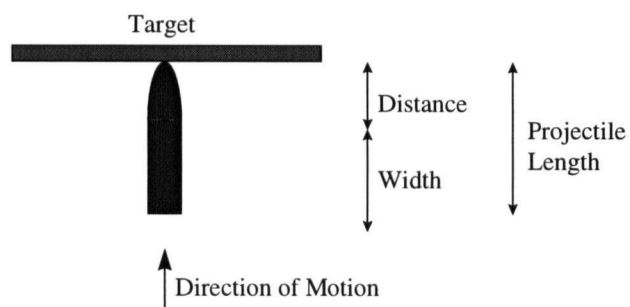Figure A.9. Curve showing a full displacement time curve.

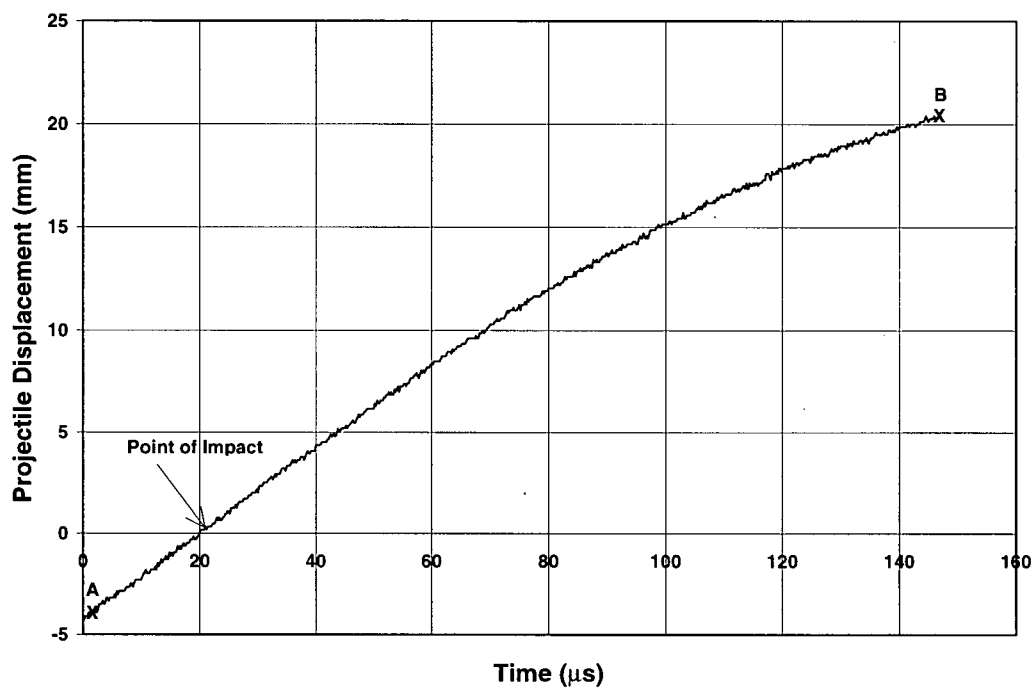Figure A.10. Schematic showing point of impact.

Figure A.11. Curve showing the reduced data set.

Appendix B

Panel Markings

This appendix describes the numbering conventions used on the tested panels.

B.1 Panel Markings

The markings on a typical tested panel are shown in Figure B.1. There are six markings on each panel and the first is labelled *top* which is the top of the specimen. The next marking is *impact* which indicates the front side of the panel. Next is an arrow which indicates the direction of the weave from the main panel. The next two markings are in the bottom left and bottom right of the specimen and they refer to the location of the specimen in relation to the original panel. The left number refers to the strip number and the right number refers to the location within the cut. A *strip* refers to a 9″ by 4′ cut from the main panel as shown in Figure B.2. The specimens are then cut from this strip. It is possible to get 14 6″ by 4″ specimens and 2 5.5″ by 4″ specimens from a single strip. A 9″ strip needs to be cut to allow for the trimming done using the diamond blade. Again from Figure B.2 the location is simply a number from 1 to 16 indicating where in the strip the specimen came from. Therefore in Figure B.1 the number 2 refers to the second strip and the number 10 refers to the location 10 in that strip. This particular specimen is highlighted in Figure B.2.

The final marking on the panels is located on the left hand side of the panel. This is the test number for the specimen. If the number is NOT on the panel then it means the panel has not been tested. The test number consists of the date, equipment used to test the panel and test number for that date. A sample code is 97-B-2403-1. The *97* refers to the year, the *B* is for Powder Gun, the *2403* is the date (ddmm) and the *1* shows that that was the first test performed that day. A *D* is used for the Drop Weight Impactor, *G* is used for the Gas Gun, an *H* for the Hopkinson Bar and an *S* for the Instron.

All the specimens were tested with the *impact* facing the projectile and the *top* at the top of the specimen.
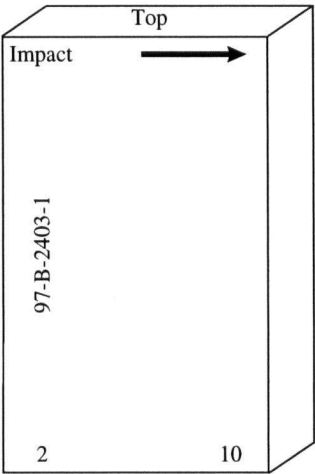
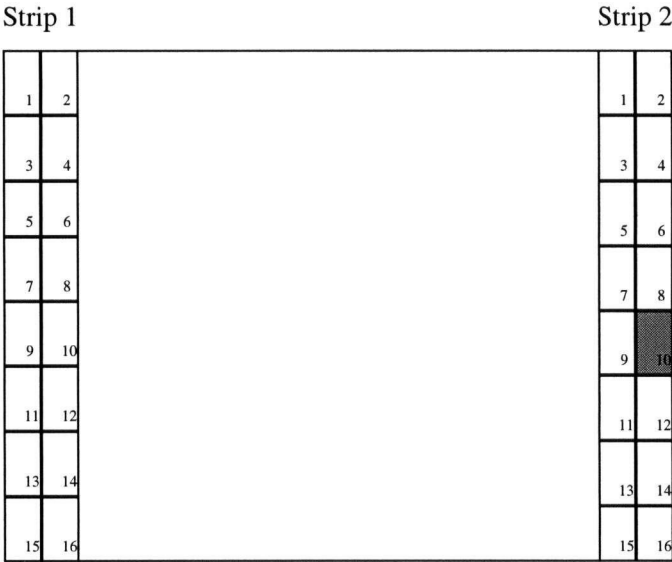Figure B.1. Figure showing panels markings of a tested panel.

Figure B.2. Figure showing position of strips and location of specimens within each strip.

Appendix C

Free Vibration

From Timoshenko [1959] the deflection along the x-axis in Figure C.1 is given by

$$w = \frac{Pa^2}{\pi^3 D} \sum_{m=1}^{\infty} \left(tanh\,\alpha_m - \frac{\alpha_m}{cosh^2\,\alpha_m} \right) \frac{sin\frac{m\pi\xi}{a}\,sin\frac{m\pi x}{a}}{m^3} \tag{C.1}$$

where D is the flexural rigidity, P is the load applied at $x = \xi$ and $\alpha_m = \frac{m\pi b}{2a}$.

The central deflection due to a force, P, applied at the centre of the plate (i.e. $x = \xi = \frac{a}{2}$), becomes

$$w = \frac{Pa^2}{2\pi^3 D} \sum_{m=1,3,5}^{\infty} \frac{1}{m^3} \left(tanh\,\alpha_m - \frac{\alpha_m}{cosh^2\,\alpha_m} \right) \tag{C.2}$$

The series converges quite quickly and equation (C.2) becomes

$$w = 0.01590 * \frac{Pa^2}{D} \tag{C.3}$$

Substituting for $a=76.2\ mm$ and α and rearranging gives

$$D = \frac{9.23*10^{-5}}{w/P} \tag{C.4}$$

where w/P is the flexibility of the plate calculated from experiments. The ratio of w/P is calculated by removing the static indentation from the static deflection curves. This leaves a curve which relates the load to plate bending. The static deflection curve with the indentation removed is shown in Figure C.2. This curve is for a 0.25″ specimen penetrated by a 37⁰ indenter.

The initial slope of this curve is then merely w/P. By substituting this value into equation (C.4) the value of D is obtained. D can then be related to the elastic modulus, E, by

$$D = \frac{Eh^3}{12(1-v^2)} \tag{C.5}$$

where h is the thickness and v the Poisson's ratio. The above equation is based on the assumption that the plate is isotropic. Using equation (C.5) a value of E=15.3 GPa is found for the 6.35 mm (0.25″) thick specimen. To validate this number the same procedure was done for the 12.7 mm (0.50″) thick specimen and a value of 15.2 GPa is found for the elastic modulus. Due to the data set for the 19.05 mm (0.75″) thick specimen the calculation was not possible.

Now that the elastic modulus is computed the natural frequency can be computed. From Timoshenko [1955] the natural period of a rectangular plate is given by

$$p = \pi^2 \sqrt{\frac{gD}{\gamma h}\left(\frac{m^2}{a^2} + \frac{n^2}{b^2}\right)} \tag{C.6}$$

where $\dfrac{\gamma h}{g}$ is defined as the mass per unit area, or areal density. Thus equation (C.6) can be written as

$$p = \pi^2 \sqrt{\frac{D}{\rho h}\left(\frac{m^2}{a^2} + \frac{n^2}{b^2}\right)} \tag{C.7}$$

where ρh is the areal density. The natural frequency is then given by

$$f = \frac{\pi}{2} \sqrt{\frac{D}{\rho h}\left(\frac{m^2}{a^2} + \frac{n^2}{b^2}\right)} \tag{C.8}$$

Using equation (C.8) the frequencies of free vibration can be calculated. The lowest mode of vibration for the 6.35 mm (0.25″), 12.7 mm (0.50″) and 19.05 mm (0.75″) thick specimens are 2.0 kHz, 4.0 kHz and 6.0 kHz respectively. Table C.1 shows the frequencies of the higher modes of vibration for the specimens.

Table C.1. Table showing frequencies of the modes of free vibration for GFRP laminates.

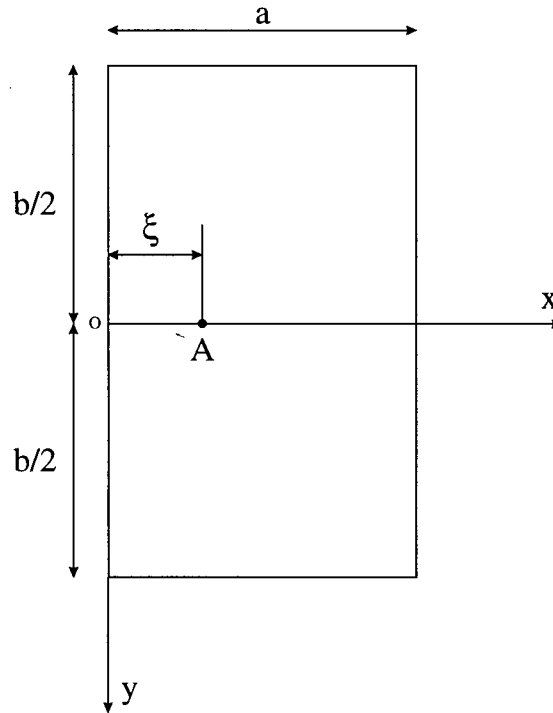| m	n	f kHz 0.25"	f kHz 0.50"	f kHz 0.75"
1	1	2.0	4.0	6.0
2	1	6.4	12.8	19.3
3	1	13.8	27.6	41.4
4	1	24.1	48.2	72.4
1	2	3.6	7.2	10.8
2	2	8.0	16.0	24.1
3	2	15.4	30.7	46.2
4	2	25.7	51.3	77.2
1	3	6.3	12.5	18.8
2	3	10.7	21.3	32.0
3	3	18.1	36.0	54.2
4	3	28.4	56.6	85.1
1	4	10.0	19.9	29.9
2	4	14.4	28.7	43.2
3	4	21.8	43.5	65.3
4	4	32.1	64.1	96.3

Figure C.1. Schematic showing nonmenclature for a rectangular plate with a force applied along the x-axis at point A.
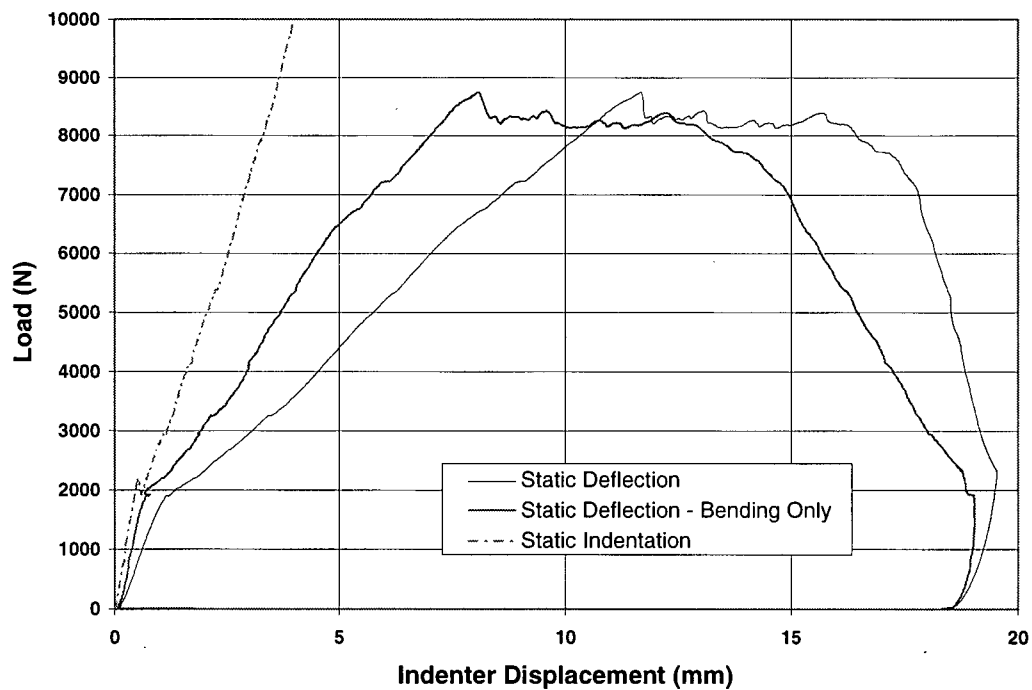

Figure C.2. Load-displacement curve for a 6.35 mm (0.25″) GFRP specimen with static indentation removed.